Non-invasive Measurements of Hepatic Glycogen Levels and Glycogen Synthesis Rates Using Chemical Exchange Saturation Transfer and Comparison to ^{13}C NMR Spectroscopy

By

Corin O'Dell Miller

Dissertation

Submitted to the Faculty of the

Graduate School of Vanderbilt University

In partial fulfillment of the requirements

for the degree of

DOCTOR OF PHILOSOPHY

in

Interdisciplinary Studies: Magnetic Resonance Imaging and Spectroscopic Methodology

August, 2015

Nashville, Tennessee

Approved: Date:

_____ _____

John C. Gore, Ph.D

_____ _____

Alan D. Cherrington, Ph.D

_____ _____

Bruce M. Damon, Ph.D

_____ _____

Eduard Y. Chekmenev, Ph.D

ACKNOWLEDGEMENTS

My gratitude to my wife and children for putting up with my absences during this process.

My gratitude to Jin Cao and Chunlian Zhang for their technical expertise and assistance with these studies.

My gratitude to both by advisors John Gore and Alan Cherrington who supported me throughout this lengthy and sometimes tortuous process, and who were continually willing to find creative ways to allow me to pursue this research, and to the other members of my PhD committee, Bruce Damon and Eduard Chekmenev, for their invaluable help and insight.

My gratitude to all my managers at Merck who supported me throughout this process, Richard Hargreaves, Donald Williams, Jeffrey Evelhoch, and Richard Kennan.

TABLE OF CONTENTS

LIST OF TABLES

Table

LIST OF FIGURES

Figure

LIST OF FREQUENTLY USED SYMBOLS AND ABBREVIATIONS

NMR – Nuclear magnetic resonance

MRS – Magnetic resonance spectroscopy

CEST – Chemical exchange saturation transfer

MTR_{asym} – Magnetization transfer ratio asymmetry

AUC – Area under the curve

PTR – Proton transfer ratio

SNR – signal to noise ratio

WSP – Weak saturation pulse

DWS – Direct water saturation

AMPK – AMP-activated protein kinase

GSase – Glycogen synthase

GPase – Glycogen phosphorylase

GK – Glucokinase

ACC – Acetyl CoA carboxylase

G6P – Glucose-6-phosphate

DNL – de novo lipognesis

RF – Radiofrequency

B_0 – Static magnetic field

B_1 – Applied magnetic field orthogonal to B_0

R_1 – Longitudinal relaxation rate

R_2 – Transverse relaxation rate

T_1 – Longitudinal relaxation time ($1/R_1$)

T_2 – Transverse relaxation time ($1/R_2$)

k – Chemical exchange rate

ω – Frequency

ANOVA – Analysis of variance

EC_{50} – Concentration of 50% excitation

CHAPTER I

GLYCOGEN AND ITS PHYSIOLOGICAL AND METABOLIC IMPORTANCE

Glycogen Structure and Tissue Distribution

Glycogen is a highly branched polymeric form of glucose that serves as the primary carbohydrate energy storage depot in mammalian cells. In the post-prandial state, ingested carbohydrates are stored as glycogen in the liver and muscle. During exercise, muscle glycogen is degraded to provide fuel for contraction. In periods of fasting or hypoglycemia, liver glycogen is broken down to glucose and released into the blood to provide energy for other tissues. As such, glycogen plays a key role in whole body glucose homeostasis and energy metabolism.

Polymerization in glycogen is achieved via α-1,4-glycosidic linkages between glucose units while branch points are introduced by α-1,6-glycosidic linkages (Figure 1A). Glycogen molecules are of varied sizes and branch points are not in precisely defined locations, and thus glycogen molecules of identical mass may have different chemical structures. A well-accepted model for glycogen structure (Gunja-Smith, 1970; Melendez-Hevia, 1993; Melendez, 1997; Goldsmith, 1982) categorizes the chains as inner B-chains, containing two branch points, and unbranched outer A-chains (Figure 1B). Analysis of mammalian glycogen suggests that the average chain length is approximately 13 glucose residues (Melendez-Hevia, 1993; Melendez, 1997) and that glycogen is made up as a series of tiers. An important structural feature is that the

outermost tier of any completely formed glycogen molecule contains approximately half of the total glucose residues of the molecule as unbranched A-chains.

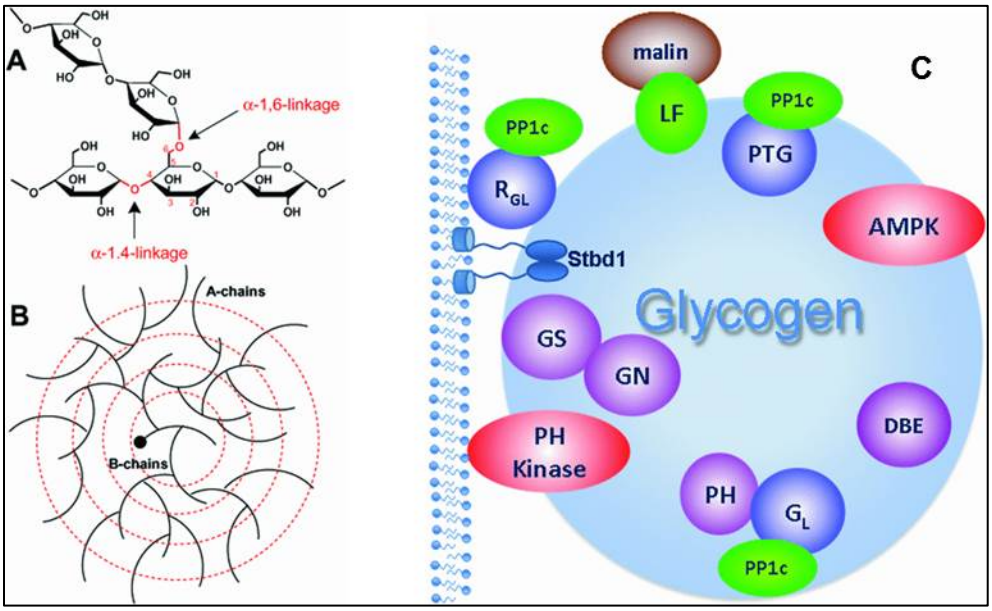

Figure 1. Schematic of glycogen structure. (A) Individual bonds between glucose molecules. (B) Model of a single glycogen molecule. (C) Model of a glycogen particle consisting of glycogen and representative associated proteins. Acronyms not defined in the text are as follows: PP1c – protein phosphatase type 1 catalytic subunit; G_L, R_{GL}, PTG – PP1 glycogen targeting subunits; LF – laforin;Stbd1 – starch-binding domain protein 1; (Reprinted from Roach, 2012)

Glycogen is known to form complexes with other small molecules, such as glucosamine (Kirkman, 1986; Kirkman, 1989) and phosphate (Fontana, 1980; Lomaka, 1984). Glycogen also forms complexes with associated proteins as shown schematically in Figure 1C (Roach, 2012). Fischer and colleagues were the first to partially purify 'glycogen particles' from muscle, which contained glycogen, proteins, and components of the sarcoplasmic reticulum (Meyer, 1970; Heilmeyer, 1970; Haschke, 1970). These particles result from the binding of certain proteins to glycogen, to each other, and also to membranes. Known proteins that associate with glycogen include the

glycogen synthesis initiator glycogenin (GN), enzymes involved in glycogen synthesis and degradation such as *glycogen synthase* (GSase), *glycogen phosphorylase* (GPase), and the *glycogen debranching enzyme* (DBE), and several regulatory proteins including *phosphorylase kinase* (PH kinase) and members of the *protein phosphatase-1G* (PP1c) family. In addition, the β-subunit of *AMP-activated protein kinase* (AMPK) has a glycogen-binding domain (Hudson, 2003; Polekhina, 2003) and is thought to play a role in the regulation of glycogen synthesis (McBride, 2009; Winnick 2011).

Glycogen is distributed throughout many tissue types in the body, but the sites in which highest concentrations of glycogen are observed are liver and muscle. As glycogen molecules are non-uniform in structure and thus do not have a consistent molecular weight, concentrations of tissue glycogen are typically reported in units of glucose equivalents per gram or per volume of tissue. Liver glycogen concentrations are normally in the 40-80 mg/g (200-400 mM) range (Wikipedia; Greutter 1994; Winnick, 2013), although under extreme glycogen loading conditions, reports of levels near 100 mg/g (500 mM) have been reported (Winnick, 2011). Liver glycogen is unique in that it functions as a storage depot under conditions of elevated circulating glucose (e.g. after a meal), and also as a supply of glucose to be released to the other tissues during periods of fasting or hypoglycemia. Muscle glycogen levels are lower than liver, typically in the 10-20 mg/g (50-100 mM) range, with a reported upper limit of 40 mg/g (Wikipedia; Hansen, 1999), although more glycogen is stored in muscle on a whole-body basis since muscle tissue is much more abundant than liver. Muscle glycogen also serves as a primary site of glucose disposal during post-meal conditions (Shulman 1990), however because muscle lacks the glucose-releasing enzyme *glucose-6-*

phosphatase (G6Pase), muscle glycogen can only supply local muscle cells with glucose. The amounts and roles of glycogen in other tissues are generally less clear and not as well studied. Approximate glycogen levels in other tissues are as follows: brain – 1 mg/g (Choi 2003; Oz, 2007), heart – 5 mg/g (Daw, 1968; Nakao, 1993), adipose – 1 mg/g (Jurczak, 2007).

Glycogen Metabolism and its Controls

In the liver, glycogen can be synthesized either from glucose, or from three-carbon precursors. These two pathways are termed the direct and indirect pathways, respectively. The contribution of the indirect pathway to glycogen synthesis is less well studied and varies depending on species and diabetic state (Huang, 1988; Moore, 1991; Hellerstein, 1993; Hwang, 1993). The direct pathway of glycogen synthesis and its controls, however, are well known. The biochemical pathways of hepatic glycogen metabolism, and their main controls, are shown in Figure 2. Several enzymes and regulatory proteins are involved in the regulation of hepatic glycogen synthesis. The bidirectional glucose transporter GLUT2 mediates transport of glucose into the liver cell. The first reaction of glycogen synthesis is the phosphorylation of glucose to glucose 6-phosphate (G6P), catalyzed by *glucokinase* (GK), the liver-specific isoform of *hexokinase*. G6P is then converted into glucose 1-phosphate (G1P) by *phosphoglucomutase*, and then to uridine diphosphate glucose (UDPG) by *UDPG pyrophosphorylase*. In the final step of glycogen synthesis, GSase catalyzes the transfer of glucose units from UDPG to glycogen by synthesis of α-1,4 bonds, while the

glycogen branching enzyme (GBE) transfers a chain of six to eight glucosyl units to a C6 to form an α-1,6 branch.

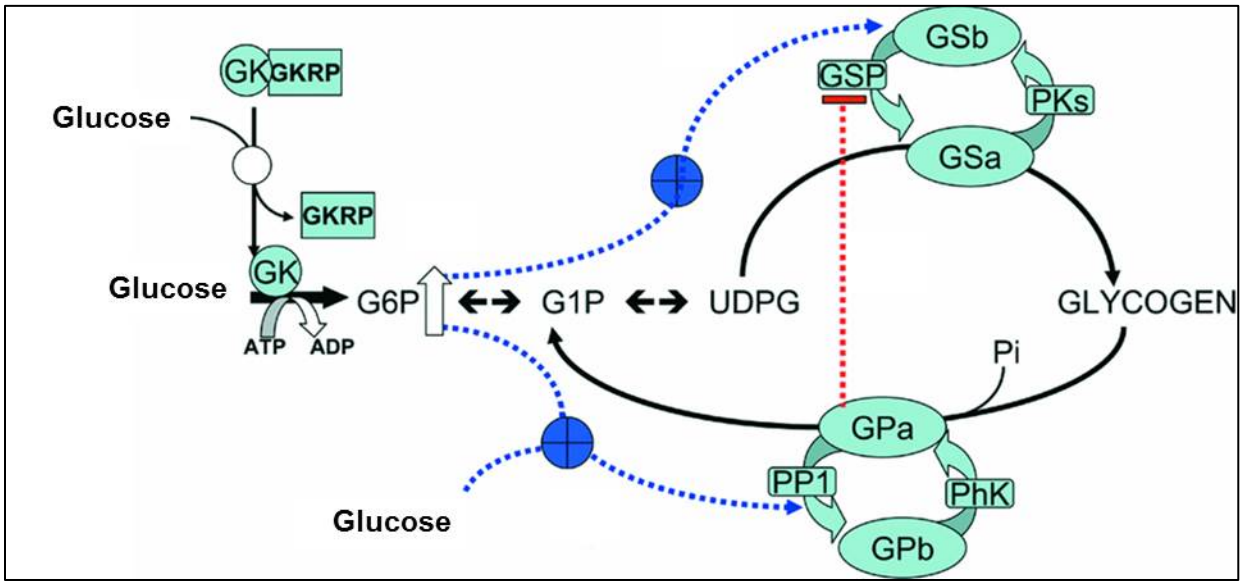

Figure 2. Pathway of hepatic glycogen metabolism (assuming direct synthesis from glucose) and its controls. Abbreviations not given in the text are as follows: GKRP – glucokinase regulatory protein; PKs – protein kinases; PP1 – protein phosphatase-1. (Reprinted from Agius, 2008).

Glycogen breakdown, for the most part, proceeds as the reverse of glycogen synthesis with the two key exceptions: (1) GSase is replaced by GPase and (2) the *glycogen branching enzyme* is replaced with the *glycogen debranching enzyme* (GDE). GPase catalyzes the degradation of glycogen by phosphorolysis of the α-1,4 bonds to form G1P. This process stops, however, when there are only four remaining glucose units from a branch point and cannot proceed further without GDE. GDE transfers three glucose units to a nearby branch and removes the final glucose unit, thereby completely removing the branch. In the case where the degraded glycogen is to be released from the liver into the circulation as free glucose, then GK is replaced by G6Pase.

Glycogen synthesis and degradation are subject to many layers of regulation, provided by small molecules, enzymes, and regulatory proteins. GK is acutely regulated by association/dissociation from a binding protein called *glucokinase* regulatory protein (GKRP), which acts as a nuclear-binding protein for GK (van Schaftingen, 1992; Choi, 2013). Cytoplasmic GK is stabilized via interactions with the bifunctional enzyme PFK2/FBPase which preserves GK's function as a 'glucose sensor' and also promotes a coordination of glucose phosphorylation and glycolysis (Massa, 2004). GK gene expression is upregulated by insulin while glucagon suppresses GK expression (Iynedijan, 1993). GSase is regulated by multi-site phosphorylation events, all of which cause varying degrees of inactivation (Roach, 2011). Conversely, activation of GSase via dephosphorylation is catalyzed by *glycogen synthase phosphatase* (GSP). G6P, the first intermediate in glucose metabolism, activates GSase in the following two ways: (1) by allosteric stimulation of the phosphorylated (inactive) form and (2) by inducing conformational changes that make it a better substrate for dephosphorylation (Villar-Palasi, 1997). It is generally accepted that the allosteric stimulation of GSase by G6P is stronger than any effects on phosphorylation or dephosphorylation. GPase is regulated by phosphorylation of a single residue at the N-terminus, catalyzed by PH kinase. The phosphorylated, activated form of GPase, (GPa) catalyzes the degradation of glycogen and is also an allosteric inhibitor of GSP. The phosphorylation state of GPase thus regulates both glycogen synthesis and degradation. The conversion of GPa into the dephosphorylated, inactive form of GPase (GPb) is catalyzed by *protein phosphatase-1* and has been shown to be regulated by both glucose and G6P, which make GPa a better substrate for dephosphorylation (Agius, 2008).

In an integrated whole body physiology sense, hepatic glycogen metabolism is regulated *in vivo* by three primary factors shown in Figure 3 (Moore, 2012), the portal vein glucose concentration, the difference between the portal vein and hepatic artery glucose levels, known as the 'portal signal' (Myers, 1991; Pagliassotti, 1996), and the prevailing hormonal concentrations. Insulin serves to augment hepatic glycogen synthesis (although mostly in the presence of a portal signal and an increased glucose load) (Cherrington, 1999) and to suppress glycogen breakdown via signaling through insulin receptor substrates (IRS) and the *protein kinase B* (aka AKT) pathway which results in inactivation of *glycogen synthase kinase* (GSK), leading to de-phosphorylation and activation of GSase (Saltiel, 2001). Glucagon increases hepatic glucose production through inhibition of glycogen synthesis and induction of glycogen breakdown by signaling through cyclic AMP and *protein kinase A*, which results in activation of PH kinase and subsequent activation of GPase (Jiang, 2003; Ramnanan 2011). Other hormones have an effect on glycogen metabolism as well. Epinephrine was shown to transiently increase glycogen breakdown while also increasing gluconeogenesis (Chu, 1997), and norepinephrine was shown to increase glycogen breakdown alone (Chu, 1998).

Although the biochemical pathways of glycogen metabolism are the same in liver and muscle, three primary differences exist in the control of muscle glycogen metabolism. First, the muscle glucose transporter (GLUT4) is not embedded in the cell membrane like GLUT2, rather it translocates to the cell membrane in response to insulin. So while the primary determinant of hepatic glucose uptake is the glucose load, the primary determinant of muscle glucose uptake is the ambient insulin level. Second,

muscle hexokinase has a much lower Km for glucose than GK (~0.1mM vs 10mM, respectively), and thus intracellular glucose is more rapidly phosphorylated in muscle resulting in potentially much higher levels of G6P in muscle than liver. Lastly, muscle does not express G6Pase and therefore cannot release glucose into the circulation like liver.

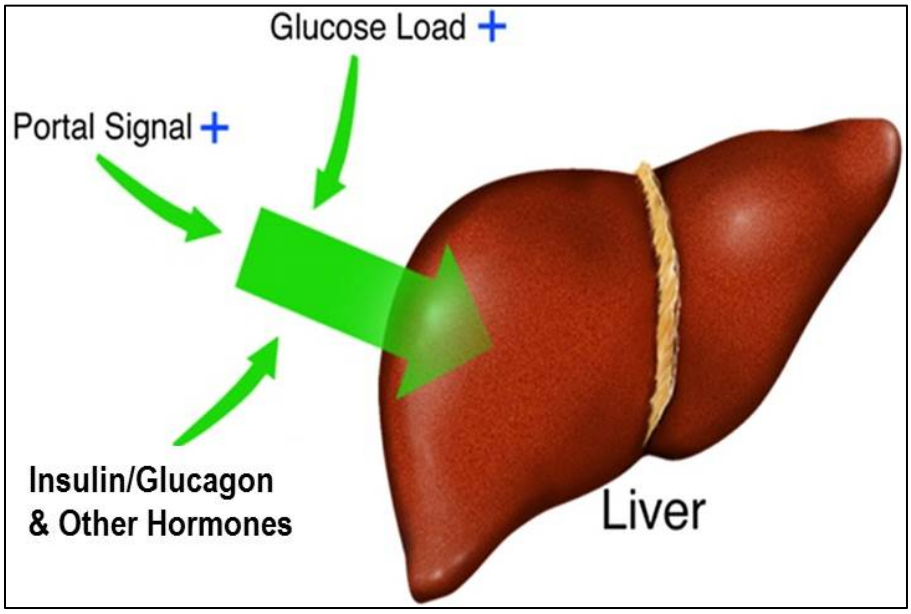

Figure 3. The physiological controls of hepatic glucose uptake and glycogen metabolism *in vivo*. (Reprinted from Moore, 2012).

While it is well established that glycogen levels represent the net result of the integration of many complex metabolic control processes, recent evidence has shown that glycogen levels themselves may be capable of exerting metabolic effects. For example, the well-known glucose secretory response of the liver to periods of hypoglycemia has recently been shown to be augmented in livers with increased glycogen content (Winnick, 2012). Additionally, in both liver (Winnick, 2013) and

muscle (Jensen, 2006), elevated glycogen levels have been shown to suppress further glycogen synthesis and it has been shown that this effect may be mediated at least in part via interaction of glycogen with the glycogen binding domain on AMPK (Hardie, 2008).

Pharmacological Effectors of Glycogen Metabolism

As glycogen is intimately linked to whole body glucose homeostasis, several of the key control points of glycogen metabolism have emerged as pharmacological targets for the treatment of diabetes.

GK activators have received much attention, although much of this is due to the additional role of GK in the pancreatic β cell's glucose-stimulated insulin secretion response (Henquin, 2000; Newgard, 2001). Nonetheless, liver-targeted GK activators may also provide a useful therapeutic effect. Hepatic GK expression is insulin dependent, and human and animal models of type 2 diabetes generally have reduced GK (Caro, 1995; Torres, 2009). Furthermore, inactivating mutations in GK result in diabetic phenotypes, particularly the so-called mature-onset diabetes of the young (MODY). Small molecule GK activators have been developed and have been shown to lower circulating glucose, stimulate insulin release, and reduce hepatic glucose production in humans and in preclinical models of diabetes (Matschinsky, 2011). Issues with this class of therapies largely have revolved around the risk of hypoglycemia due to the activation of pancreatic GK and the resultant large increase in insulin release. This

suggests that a liver-targeted GK activator may have a more optimal efficacy/safety profile.

As GPase is the rate controlling step in the breakdown of glycogen and subsequent release from the liver, it too represents a potential pharmacological target. Several different small molecule inhibitors, binding to different sites on the enzyme, have ameliorated hyperglycemia and other symptoms related to diabetes in animal models of type II diabetes (Baker, 2006). Key issues in the development of this class of therapies include isoform specificity (GPase is also expressed in the muscle and brain) and also a greater understanding of the effects of removing a part or all of such a vital fuel source, especially during periods of exercise and fasting.

Upon the discovery that muscle glycogen synthesis was markedly reduced in type II diabetic humans under hyperglycemic-hyperinsulinemic conditions (similar to those observed after a meal) (Shulman 1990), muscle GSase became a novel target for type II diabetes. In particular, inhibitors of *glycogen synthase kinase 3* (GSK3) were developed as a means of activating GSase. Several small molecule inhibitors of GSK3 showed insulin-like effects in preclinical diabetic models including increased GLUT4 (the muscle glucose transporter) translocation to the plasma membrane, activation of glucose uptake and glycogen synthesis in muscle cells, and suppression of gluconeogenic enzymes (Eldar-Finkelman, 2003). These effects generally led to improvements in oral glucose tolerance. The key issue in the development of GSK3 inhibitors is the enzyme's role in the regulation of cell mitosis and the potential for risks of carcinogenicity.

In other cases, pharmacological targets may have unexpected impacts on glycogen metabolism. For example, activation of AMPK was shown to directly phosphorylate and inhibit GSase in vitro (Carling, 1989), yet a recent study demonstrated that mice treated with an AMPK activator paradoxically had increased muscle glycogen levels (Hunter, 2011). Further analysis revealed that the effect of AMPK activation to directly increase muscle glucose uptake via increased GLUT4 translocation and subsequently increase intracellular levels of G6P, was able to override the direct inhibitory effects of AMPK on GSase alone. This finding was consistent with the idea that G6P is the strongest modulator of GSase activity and reinforces the idea that glycogen synthesis *in vivo* represents the sum of potentially many different processes, and cannot always be predicted from individual *in vitro* data alone.

CHAPTER II

MEASUREMENT METHODS FOR LIVER GLYCOGEN

Tissue Biopsy

As glycogen is confined to intracellular locations, robust and reliable measurements of liver glycogen content have been problematic. Biochemical assay of glycogen following a tissue biopsy is the oldest measurement method. This approach generally consists of homogenization and extraction of glycogen from a frozen tissue sample, followed by either enzymatic or chemical degradation of glycogen to glucose and subsequent assay of glucose concentrations via clinical chemistry analyzers or traditional glucose assay kits. The tissue biopsy method is limited by its invasive nature, along with the potential for regional variation within the liver (Moore, 1991) and these shortcomings have generally limited the clinical utility of this approach.

^{13}C Magnetic Resonance Spectroscopy

The ability to measure glycogen non-invasively in liver with ^{13}C magnetic resonance spectroscopy (MRS) was demonstrated approximately 25 years ago (Jue, 1987; Avison, 1988). The basic principles of MRS have been described in a number of reviews (Roden, 1999; Shulman 2001) and are discussed only briefly here. Certain nuclei possess a magnetic moment or “spin” which in the absence of any external magnetic influence will be randomly oriented. When placed inside a strong, static

magnetic field generated by a nuclear magnetic resonance (NMR) spectrometer or magnetic resonance imaging (MRI) scanner, the nuclei will precess around the direction of the external magnetic field (generally assigned as the +Z direction) with a characteristic frequency called the Larmor frequency. These nuclear spins can align either parallel or antiparallel to the magnetic field and at equilibrium, more will align parallel to the field due to the lower energy state, generating a net magnetization in the +Z direction. This is shown schematically in Figure 4.

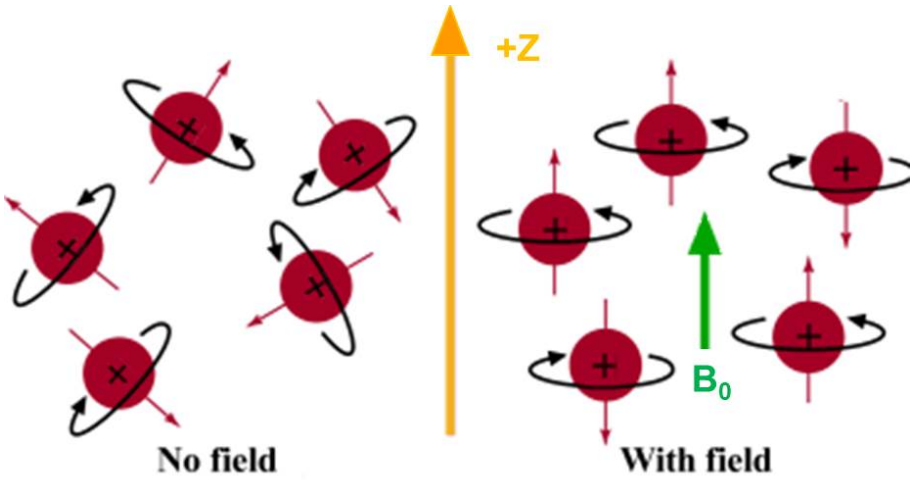

Figure 4. Schematic of nuclear spins in random orientations (left) and aligned parallel or antiparallel with an external magnetic field (right). (Image taken from 'Basics of NMR' online course, https://www.cis.rit.edu/htbooks/nmr/)

Excitation of these nuclei by an additional orthogonal oscillating magnetic field at the Larmor frequency (generally in the radiofrequency range) temporarily tips the spins of these nuclei out of alignment with the external field into the x-y plane. In the process of returning back to the low energy-state of alignment within the static magnetic field, energy in the form of radiofrequency (RF) waves is emitted and detected by a receiver coil oriented in the x-y plane. This signal generally has a decaying oscillating pattern

and is termed a free induction decay (FID). In most experimental settings, RF emissions from different nuclei in different chemical environments (either due to being in different molecules or in different tissue types) are superimposed, and the Fourier transformation is used to convert the time domain FID data recorded by the receiver into a spectrum (i.e. a display of signal intensities versus frequency) as shown in Figure 5. The frequency axis for an NMR spectrum is called the 'chemical shift' and is the difference (shift) in the frequency of the nuclei of interest and the base frequency of the spectrometer. This scale can be in units of Hz, or more commonly, parts per million (ppm) with respect to the spectrometer base frequency.

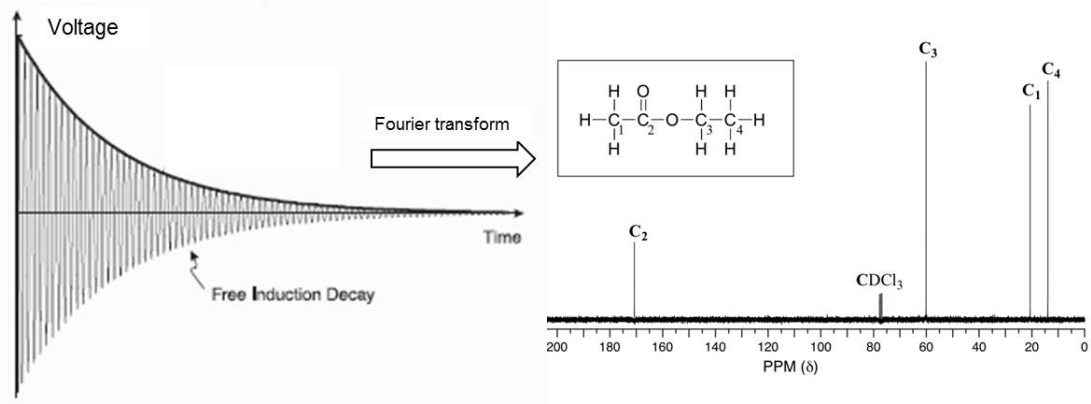

Figure 5. Sample ^{13}C MRS time domain free induction decay signal and Fourier transformed spectrum. (Images taken from Google Images)

For ^{13}C MRS, each resonant frequency is unique to a specific type of nuclei, thereby enabling one to distinguish compounds with characteristic peak frequencies in an NMR spectrum. The area under a particular peak is proportional to the molar amount of that chemical species and can be converted to standard concentration units by

comparison with spectra obtained from a standard solution (aka phantom) containing a known amount of that compound and acquired under identical conditions.

Despite the low natural abundance (1.1%) and inherently low NMR sensitivity of ^{13}C (with a gyromagnetic ratio ~1/4 that of ^{1}H), liver glycogen is present in sufficient quantities that it can still be detected at natural abundance with ^{13}C MRS. ^{13}C MRS can also be used in combination with infusions of ^{13}C glucose labeled at various positions to trace ^{13}C incorporation into glycogen and thereby measure glycogen synthesis rates. This incorporation of ^{13}C label into glycogen can increase the sensitivity of the ^{13}C MRS glycogen signal by 10-20 fold depending on the experimental protocol.

The initial reports of glycogen detection using natural abundance ^{13}C MRS (Jue, 1987; Avison, 1988) were soon followed by the demonstration that in vivo glycogen was 100% visible by MRS (Gruetter, 1991), and that MRS measurements of tissue glycogen yielded accurate estimates of glycogen levels when compared with tissue biopsies (Gruetter, 1994). Initial applications of ^{13}C MRS to glycogen metabolism included the measurement of glycogen synthesis rates in liver (Jue, 1989) and muscle (Jue, 1989) using both natural abundance ^{13}C MRS and [1-^{13}C] glucose infusions. Natural abundance ^{13}C MRS was also used to measure hepatic glycogen breakdown rates during a prolonged fast (Rothman, 1991). This protocol was then used as part of a novel method to estimate rates of gluconeogenesis by subtracting the ^{13}C MRS measured rate of glycogen breakdown from a separate isotope infusion based measure of whole body glucose production. These initial reports opened the door for many subsequent studies examining glycogen metabolism under various conditions and also exploring the role of glycogen metabolism in whole body glucose homeostasis.

Building on these initial studies, ^{13}C MRS measurements of glycogen were then applied to understanding defects of glycogen metabolism in type I and II diabetes mellitus. In one of the early landmark clinical studies, it was shown that under hyperglycemic-hyperinsulinemic conditions (similar to those observed after a meal), type II diabetic subjects exhibited a reduction in muscle glycogen synthesis (Shulman, 1990). When these rates were extrapolated to the whole body, it was concluded that muscle glycogen synthesis accounted for the majority of whole body glucose uptake and non-oxidative glucose metabolism and that this defect was likely to be a primary cause of the observed post-meal hyperglycemia in the type II diabetic subjects. Follow up studies used ^{13}C MRS to help dissect the potential causes of this impairment in muscle glycogen synthesis (Rothman, 1995; Cline, 1997). Previously, it was thought that flux through GSase was the key rate controlling step in glycogen synthesis, however data from these studies pointed to defects in muscle glucose transport and/or phosphorylation as being primarily responsible for the observed resistance to insulin-stimulated glycogen synthesis in muscle.

Investigations of hepatic glucose metabolism using ^{13}C MRS also yielded valuable insights into the diabetic state. Indirect measurements of gluconeogenesis as described previously above revealed that type II diabetic subjects exhibited increased rates of gluconeogenesis after an overnight fast (Magnusson, 1992). Additionally, type I diabetic subjects exhibited reduced hepatic glycogen synthesis after a mixed meal challenge (Hwang, 1995). These initial demonstrations of defects in tissue glycogen metabolism in diabetic subjects were followed by much more detailed work in liver and muscle which incorporated molecular biology measurements along with ^{13}C MRS in an

attempt to elucidate the mechanisms of insulin resistance in these tissues. Detailed reviews of these findings have been given elsewhere (Savage, 2007; Samuel, 2010) and are not appropriate here, however it should be stated that the results of these studies provided the basis for current theories of lipid induced insulin resistance and its role in diabetes.

Despite these advances, in vivo ^{13}C NMR spectroscopy still remains handicapped by its inherently low signal to noise ratio (SNR) due to the low natural abundance and the low gyromagnetic ratio of the ^{13}C nucleus, as well as the cost of the often required ^{13}C labeled isotopes. Furthermore, the vast majority of clinical MRI scanners lack ^{13}C detection capability, and clinical adaptation of this technology will likely remain within the research community only.

CEST Method for Glycogen Detection

Recently, a novel MRI method for detection of tissue glycogen was reported (van Zijl, 2007) based on sensing the chemical exchange of glycogen hydroxyl protons with tissue water. This method is generally referred to as chemical exchange saturation transfer (CEST). In general, this method is relatively straightforward to implement on current NMR spectrometers and MRI imaging systems, because only proton detection is required (e.g. Zhou, 2011; Longo, 2014). However, whether it can reliably measure physiological concentrations of glycogen, and what other factors affect its accuracy, have not been established. The basis of CEST detection of glycogen via exchange of hydroxyl protons is shown schematically in Figure 6 where the ^{1}H NMR signal from a

relatively small solute pool with exchangeable protons, glycogen in this case (Figure 6A), can be indirectly detected via saturation with NMR pulses, transfer of these saturated protons to the hydroxyl functional groups to water, and subsequent measurement of the attenuation of the water ^{1}H NMR signal (Figure 6B). This saturation transfer process is repeated for multiple frequency offsets from water and the resulting series of water peaks acquired at these frequency offsets (ω) is typically called a 'Z-spectrum' (Figure 6C), and is used to calculate the Magnetization Transfer Ratio Asymmetry (MTR_{asym}) (Figure 6D) as:

$$MTR_{asym}(\omega) = [S(-\omega) - S(\omega)]/S_0 \qquad (1)$$

Here, S represents the water signal observed at a saturation offset ω from the water resonance, and S_0 is the water signal observed at a saturation offset far (>20 ppm) from the water resonance where no CEST saturation effects are expected to be present. Note that Ihave adopted the standard convention in CEST studies of defining the water resonance to be 0 ppm. Most reported measures of CEST are based on this MTR_{asym} parameter, though for some choices of the saturation parameters there may be factors other than chemical exchange that influence measured values of MTR_{asym}.

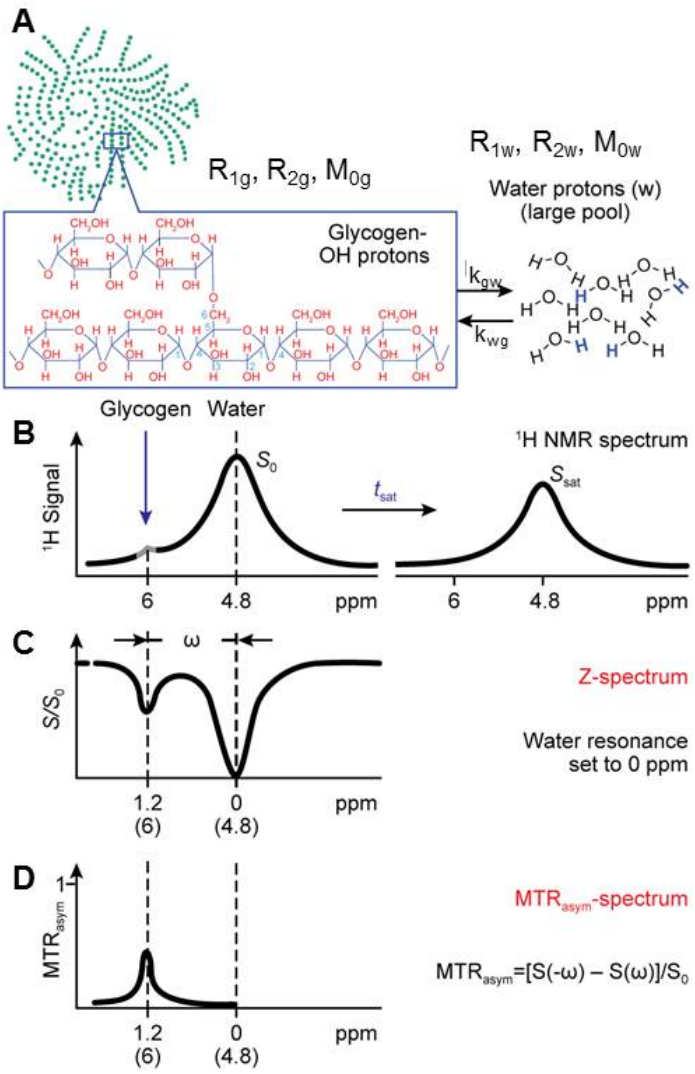

Figure 6. Illustration of the CEST phenomena (A) and (B), and traditional methods used to quantify CEST (C) and (D) (Adapted with permission from van Zijl, 2007).

Proton CEST approaches benefit from increased SNR compared to ^{13}C MRS and also from the wide availability of ^{1}H MR hardware. The use of CEST based approaches to detect other –OH and –NH containing metabolites has been recently reported for glycosaminoglycans (Ling, 2008), creatine (Kogan, 2014), glutamate (Cai, 2012), glucose (Chan, 2012), and 2-deoxy-glucose (Nasrallah, 23; Rivlin, 2013). Despite the

demonstration of proof of concept for detection of these metabolites, the optimization, calibration, and quantification in the tissue of interest using CEST has, for the most part, not yet been reported. Furthermore, in the initial report of CEST-based detection of glycogen (van Zijl, 2007), there appeared to be a non-linear and saturating relationship between the amount of glycogen and the CEST signal measured in phantoms over the expected physiological range, calling into question the utility of this approach for measurements of physiological levels of liver glycogen.

The overall the goals of this work were therefore as follows: (1) to develop optimal acquisition parameters for both ^{13}C MRS and CEST measurements of glycogen at 11.7T using phantoms with glycogen amounts over the expected physiological range, (2) to develop protocols using ^{13}C MRS and CEST methods to measure total liver glycogen in perfused livers at 11.7T, and (3) to develop physiological protocols to combine with the ^{13}C MRS and CEST methods to measure glycogen synthesis rates both in perfused livers at 11.7 T, and *in vivo* at 7T using CEST alone. Additionally, as an application of this methodology, I sought to utilize these methods to address a novel pharmacological question, specifically, the effects of acute activation of AMPK on hepatic glycogen synthesis in perfused livers.

CHAPTER III

CHEMICAL EXCHANGE SATURATION TRANSFER THEORY

Introduction

Here I will describe the theoretical aspects of CEST for a two pool system with glycogen being the solute of interest and water being the solvent. The analysis is similar to that described in Zhou, 2006. For such a system, chemical exchange processes are commonly described by the Bloch equations with exchange terms included. These are sometimes called the Bloch–McConnell equations (McConnell, 1958). In general, it is difficult to obtain analytical solutions of these equations, and so I will use some reasonable assumptions, where convenient, to gain insight into the factors affecting the CEST signal.

Two Pool Model of Chemical Exchange

Figure 6A shows a schematic for the two exchanging pools, a small pool of glycogen with exchangeable –OH protons (g) and a large pool of bulk water protons (w). These two pools have relaxation rates and initial magnetizations of R_{1g}, R_{2g}, and M_{0g}, and R_{1w}, R_{2w}, and M_{0w}, respectively. The analysis starts with the usual Bloch equations in the rotating reference frame for each of the two pools shown in Figure 6A. To account for the effects of relaxation, the terms $-R_2M_x$, $-R_2M_y$, $-R_1(M_0-M_z)$ are added to the x, y, and z components, respectively, of glycogen and water in the Bloch equations.

To account for the effects of chemical exchange, the terms ± kM_x, ± kM_y, and ± kM_z are also respectively added to the x, y, and z components of glycogen and water, with the sign being determined by the direction of the exchange. For the current two pool model, we make the following definitions: $\omega_0=\gamma B_0$, $\omega_1=\gamma B_1$ (where γ is the nuclear gyromagnetic ratio, B_0 is the main magnetic field, and B_1 is the applied radiofrequency field). Working in the rotating frame, WE define $\Delta\omega_g=\omega_g-\omega_0$ and $\Delta\omega_w=\omega_w-\omega_0$ which results in the components of the vector $\vec{\omega}$ being $(-\omega_1, 0, \Delta\omega_g)$ and $(-\omega_1, 0, \Delta\omega_w)$ for glycogen and water, respectively. When written for each pool, including both relaxation and chemical exchange terms, the Bloch equations become:

$$dM_{xg}/dt = -\Delta\omega_g M_{yg} - R_{2g}M_{xg} - k_{gw}M_{xg} + k_{wg}M_{xw} \quad (2)$$

$$dM_{yg}/dt = \Delta\omega_g M_{xg} + \omega_1 M_{zg} - R_{2g}M_{yg} - k_{gw}M_{yg} + k_{wg}M_{yw} \quad (3)$$

$$dM_{zg}/dt = -\omega_1 M_{yg} - R_{1g}(M_{zg} - M_{0g}) - k_{gw}M_{zg} + k_{wg}M_{zw} \quad (4)$$

$$dM_{xw}/dt = -\Delta\omega_w M_{yw} - R_{2w}M_{xw} + k_{gw}M_{xg} - k_{wg}M_{xw} \quad (5)$$

$$dM_{yw}/dt = \Delta\omega_w M_{xw} + \omega_1 M_{zw} - R_{2w}M_{yw} + k_{gw}M_{yg} - k_{wg}M_{yw} \quad (6)$$

$$dM_{zw}dt = -\omega_1 M_{yw} - R_{1w}(M_{zw} - M_{0w}) + k_{gw}M_{zg} - k_{wg}M_{zw} \quad (7)$$

The number of differential equations can be reduced and some terms omitted under certain assumptions, the most common of which is the weak saturation pulse (WSP) approximation (Forsen, 1963; Zhou, 2004), in which no direct water saturation occurs.

Weak Saturation Pulse Approximation

The simplest approximation is to assume that the RF field is applied only to the pool of glycogen protons (g) with the pool of water protons (w) left unperturbed. Under these conditions, we have $\Delta\omega_g=0$ and $\Delta\omega_w\rightarrow\infty$. Further assuming complete saturation (cs) of the irradiated protons, a simple solution can be obtained from Eq. (7):

$$M_{zw}^{cs} = M_{0w}[R_{1w}/(R_{1w}+k_{ws})] \quad (8)$$

The proton transfer ratio (PTR), in general, can be defined as:

$$PTR = (M_{0w} - M_{zw})/M_{0w} \quad (9)$$

Therefore, when pool s is completely saturated, the proton transfer ratio (PTR) for the water signal can be derived to be:

$$PTR^{cs} = k_{ws}/(R_{1w}+k_{ws}) \quad (10)$$

While this is an interesting result from the simplest case, complete saturation can be obtained only under a very strong RF field, which is not a true case.

Steady-State Solutions Under the WSP Approximation

We now use the case-sensitive definitions: $m_{zg}=M_{zg}-M_{0g}$, $m_{zw}=M_{zw}-M_{0w}$, $r_{1g}=R_{1g}+k_{gw}$, $r_{1w}=R_{1w}+k_{wg}$, $r_{2g}=R_{2g}+k_{gw}$, and $r_{2w}=R_{2w}+k_{wg}$. If the RF field is applied to glycogen protons only, equations (2) – (7) can be simplified to:

$$dM_{yg}/dt = \omega_1 m_{zg} - r_{2g} M_{ys} + k_{wg} M_{yw} + \omega_1 M_{0g} \quad (11)$$

$$dm_{zg}/dt = -\omega_1 M_{yg} - r_{1g} m_{zg} + k_{wg} m_{zw} \quad (12)$$

$$dM_{yw}/dt = -r_{2w} M_{yw} + k_{gw} M_{yg} \quad (13)$$

$$dm_{zw}/dt = -r_{1w} m_{zw} + k_{gw} m_{zg} \quad (14)$$

The steady-state (ss) solutions of these four equations can be obtained by setting the left hand sides of equations (11) – (14) equal to zero, and the results can be expressed as

$$m_{zg}^{ss} = -\frac{\omega_1^2 M_{0g}}{\omega_1^2 + pq} \quad (15)$$

$$M_{yg}^{ss} = -\frac{\omega_1 q M_{0g}}{\omega_1^2 + pq} \quad (16)$$

$$m_{zg}^{ss} = -\frac{k_{gw}}{r_{1w}} \frac{\omega_1^2 M_{0g}}{(\omega_1^2 + pq)} \quad (17)$$

$$M_{yg}^{ss} = -\frac{k_{gw}}{r_{2w}} \frac{\omega_1 q M_{0g}}{\omega_1^2 + pq} \quad (18)$$

where $p = r_{2g} - (k_{gw}k_{wg}/r_{2w})$ and $q = r_{1g} - (k_{gw}k_{wg}/r_{1w})$. From here, it is convenient to define the labeling fraction or saturation efficiency for pool g as

$$\alpha = -m_{zg}^{ss}/M_{0g} = \omega_1^2/(\omega_1^2 + pq) \quad (19)$$

Time-Dependent Solutions Under the WSP Approximation

The next assumption is to separate the process of saturation transfer into two consecutive steps, the first being the saturation of glycogen protons, and the second being the transfer of these saturated protons to water. If the glycogen pool is completely isolated, its saturation rate can be estimated to be $(R_{1s}+R_{2s})/2$, meaning that pool g has a saturation time constant of tens of ms (in the order of T_{2s}). Thus, this two-step approximation is very close to the actual situation.

Assuming that pool s (exchangeable solute protons) approaches a steady state $(m_{zg}^{ss} = M_{zg}^{ss} - M_{0g})$ instantly, the dynamics for pool w can be described by:

$$dm_{zw}/dt = -r_{1w}m_{zw}+k_{gw}m_{zg}^{ss} \quad (20)$$

If $M_{zw}(t_0) = M_{0w}$ (the weak pulse approximation), then $m_{zw}(t_0) = 0$. We have the solution

$$m_{zw}(t) = \frac{k_{gw}m_{zg}^{ss}}{r_{1w}}\left[1 - e^{-r_{1w}(t-t_0)}\right] \quad (21)$$

which demonstrates that the water protons approach a steady state with a rate r_{1w} (recall, $r_{1w}=R_{1w}+k_{wg}$), which can be thought of as the spin–lattice relaxation rate of the water protons in the presence of RF irradiation on the glycogen protons. Therefore, the PTR in the water signal can be derived to be

$$PTR = \frac{M_{0w} - M_{zw}(t_{sat})}{M_{0w}} \quad (22)$$

$$PTR = \frac{k_{gw}\alpha M_{0g}}{(R_{1w}+k_{wg})M_{0w}}\left[1 - e^{-(R_{1w}+k_{wg})(t_{sat})}\right] \quad (23)$$

where t_{sat} is the applied RF saturation time. This result suggests that the PTR depends on the exchangeable proton concentration of glycogen ($M_{0g} \propto$ [glycogen]), the chemical exchange rate of the glycogen protons, as well as on saturation efficiency for glycogen and T_1 of the water. It should be noted that at fast exchange rates, high exchangeable proton concentrations, and a high magnetic fields (which have lower R_{1w} values), k_{wg} may become comparable with R_{1w}, and back exchange (water protons to glycogen protons) may be of influence.

The Magnetization Transfer Asymmetry Ratio

A typical CEST acquisition consists of a series of saturation pulses at varied frequency offsets from zero. The resulting plot of water NMR signal versus saturation frequency offset is called a 'Z-spectrum' (Figure 6C) and is used to calculate the MTR_{asym} parameter as given in equation (1). This analysis, however, is based on the assumption that direct water saturation (DWS) and general magnetization transfer (MT) effects are symmetric about the water resonance frequency. Recently, an alternative method to calculate the CEST MTR_{asym} was proposed (Zaiss 2011), based on the theoretical result that under the WSP approximation the DWS portion is Lorentzian in shape. Thus, when applicable, some of the studies reported here use this approach of fitting the experimental Z-spectrum over the non-glycogen signal containing regions to a Lorentzian model and then calculating the MTR_{asym} as the difference between the modeled DWS and the experimental Z-spectrum. This approach is shown schematically in Figure 7 below and can be very useful in cases where the Z-spectrum

is not centered exactly on 0 ppm as this can be incorporated into the model and used to correct the Z-spectrum.

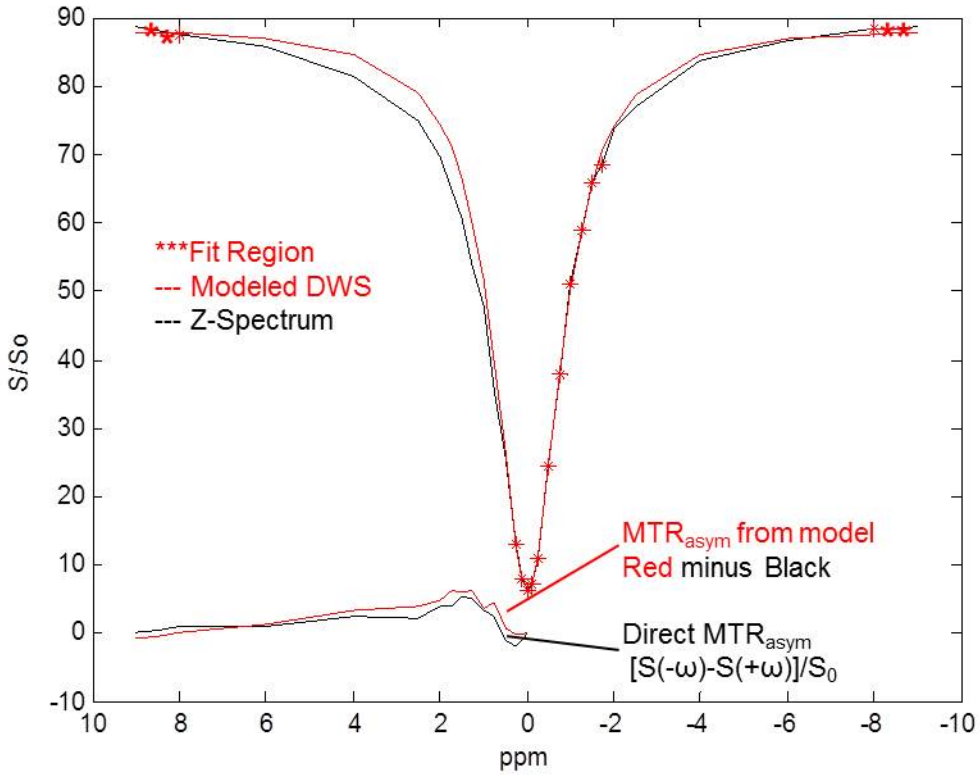

Figure 7. Illustration of the modelling procedure using an inverted Lorentzian fit of the DWS portion of the Z-spectrum to calculate the glycogen MTR_{asym}.

CHAPTER IV

PHANTOM STUDIES AND OPTIMIZATION OF CEST PARAMETERS

Introduction

In this Chapter I describe phantom studies aimed to derive optimal CEST acquisition parameters which yield a linear relationship with maximal measurement window between CEST glycogen signal and total phantom glycogen content over the expected physiological range.

Methods

Glycogen (oyster, Sigma-Aldrich P/N # G8751) was dissolved in a Krebs-Henseleit buffer supplemented with 0.25% bovine serum albumin, 0.1 mM palmitate, 0.5 mM glutamate, 0.5 mM glutamine, and 1 mM ATP (final pH = 7.4). As the maximum expected concentration of liver glycogen is approximately 400 μmoles/g, and the maximum expected mouse liver size for the perfused liver studies was 2 g, phantoms were constructed with up to 800 μmoles of glycogen (measured as glucose equivalents) in the sensitive volume of the NMR probe. CEST Z-spectra were acquired with varying saturation pulse powers and times in order to investigate which combination of parameters yielded a linear relationship between total phantom glycogen and the numerically integrated CEST MTR_{asym} area under the curve (AUC), with maximal dynamic range. It should be noted that these phantom studies were performed only to

determine the optimal saturation pulse parameters and were not used to calibrate the glycogen CEST signal. This is because tissue glycogen will likely have different structural (chain length, branching, protein binding) and relaxation characteristics compared to glycogen in solution.

NMR Acquisitions – All studies were performed on a Bruker 500 MHz (11.7 T) vertical bore NMR spectrometer using XWin-NMR 3.2 and a 20 mm TXO probe with $^{13}C/^{31}P$ on the inner coil and $^{1}H/^{2}H$ on the outer coil with a custom fabricated 20 mm NMR tube. Magnetic field lock was provided by a small (~0.5 mL) separate sealed tube of D_2O placed inside the 20 mm NMR tube. Natural abundance ^{13}C NMR acquisitions were performed using a 15° square pulse, ^{1}H broadband decoupling, an inter-pulse delay of 560 msec, and 1600 averages (22 min acquisition time). CEST NMR acquisitions were performed using 32 non-uniformly spaced frequency offsets as follows: [±9, ±8.5, ±8, ±6, ±4, ±2.5, ±2, ±1.75, ±1.5, ±1.25, ±1, ±0.75, ±0.5, 0, 40 ppm].

Data Analysis – ^{13}C NMR spectra of glycogen were analyzed with peak fitting programs written in Matlab. Briefly, the glycogen NMR resonances were each fit to a Lorentzian lineshape model, the parameters of which were optimized using a least-squares minimization routine. Each modeled resonance was then integrated analytically and the sum of the areas was calculated and used to calibrate future glycogen measurements in perfused livers.

For the CEST acquisitions, all data analysis was performed using Matlab functions. Z-Spectra were calculated by first numerically integrating each magnitude ^{1}H NMR spectrum between +2 and -2 ppm from the water resonance (to avoid the lipid

^{1}H NMR signal) from each saturation frequency offset. These integrals were then normalized to the corresponding integral of the ^{1}H NMR signal acquired with a 40 ppm frequency offset to form the Z-spectrum. For this particular application, the Z-spectrum can be considered the sum of the CEST contribution and the direct water saturation (DWS) contribution. As described in Chapter III, it can be shown that the DWS component of the Z-spectrum is theoretically inverted Lorentzian in shape. Accordingly, experimental Z-spectra were fit over the **non-glycogen signal containing regions** (Figure 7) with an inverted Lorentzian model given by

$$DWS(\omega) = L_0 - \frac{h}{4\left(\frac{\omega-\omega_0}{LW}\right)^2+1} \quad (24)$$

where L_0 is a small DC offset parameter, h is the height, ω_0 is the center frequency, and LW is the full width at 50% peak height. This fit was performed over the non-glycogen signal containing regions of the Z-spectrum using the following subset of saturation frequency offsets: [±9, ±8.5, ±8, ±0.1, 0, -0.25, -0.5, -0.75, -1, -1.25, -1.5, -1.75, 2 ppm from water] (23). The glycogen MTR_{asym} function was then calculated as the difference between the modeled DWS spectrum and the experimental Z-spectrum, i.e.

$$\text{Glycogen } MTR_{asym}(\omega) = DWS(\omega) - S(\omega) \quad (24)$$

and this glycogen MTR_{asym} curve was numerically integrated to yield the final measure of glycogen CEST signal. While this Lorentzian fitting procedure may be subject to small errors due to the potential inclusion of NOE effects in the region used to fit the DWS portion of the Z-spectrum, it should be noted that the direct calculation of the MTR_{asym} (eq. 1) would suffer from the same shortcoming. Furthermore, I observed that

this procedure proved superior to the direct calculation of the MTR_{asym} in our perfused liver studies as it allowed for any slight deviations of the 0 ppm offset to be incorporated into the model and corrected for.

Results and Discussion

Figure 8A shows sample Z-spectra (B_1 = 4 μT, 0.5 sec) and MTR_{asym} curves for total phantom glycogen amounts of 0, 200, 400, and 800 μmoles of glucose equivalents. Figure 8B shows a plot of total phantom glycogen versus CEST MTR_{asym} total AUC for a B_1 = 4 μT saturation pulse with saturation times of 0.25, 0.5, 1, and 2 seconds. The 0.5 sec pulse was defined as optimal based on the observation that it yielded the maximum dynamic range while maintaining a high degree of linearity (R^2 = 0.96). Studies with lower B_1 values and/or longer saturation times were also performed but, as expected from other reports, resulted in either a reduced dynamic range or a nonlinear relationship. As stated previously, these phantom studies were performed only to determine the optimal saturation pulse parameters for glycogen and were not used to calibrate the glycogen CEST signal due to expected differences in structural and relaxation characteristics compared to glycogen in tissue. Our RF pulse parameters and MTR_{asym} values were similar to those reported in many other biomolecule CEST studies. I also separately studied the CEST MR signal from glucose in similarly prepared phantoms (data not shown) and found that the CEST signal was approximately 2-fold greater, consistent with the fact that free glucose has 5 exchangeable hydroxyl groups,

while the glucosyl units in glycogen have 2-3 exchangeable hydroxyl groups depending on branching within the glycogen molecule.

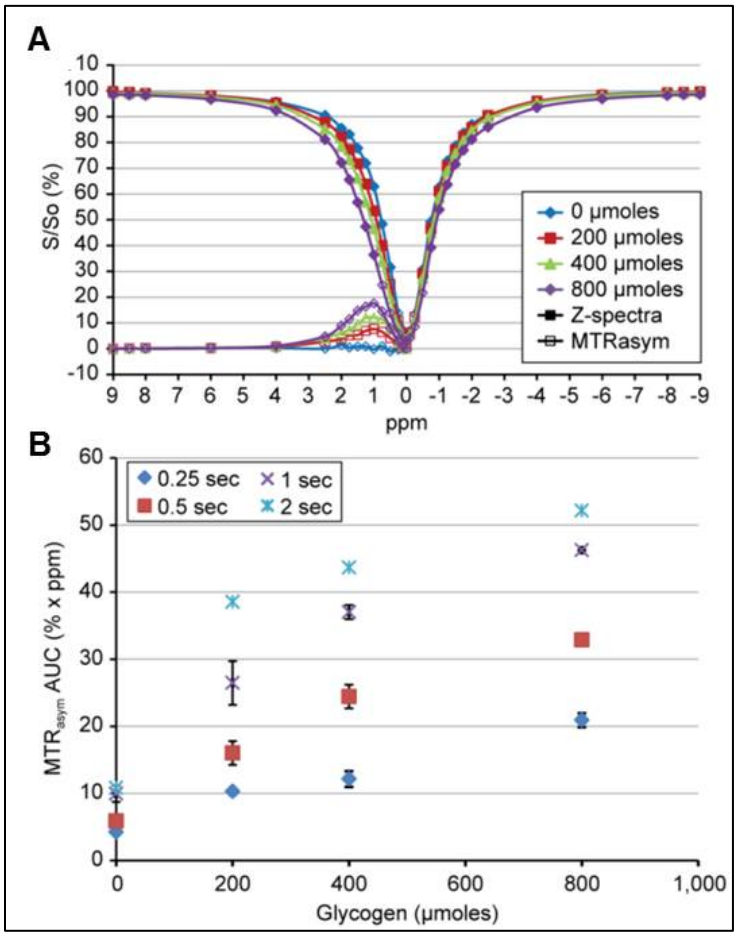

Figure 8. Z-spectra and MTR_{asym} curves for phantom glycogen solutions (A), and the relationship between total phantom glycogen and MTR_{asym} AUC for different saturation pulse lengths with B_1 = 4 µT (n=2).

The data for ^{13}C MRS measurements of phantom glycogen is shown below in Figure 9. This data confirms that ^{13}C MRS can accurately measure glycogen over the expected physiological range and will be used to calibrate ^{13}C MRS measurements of glycogen in perfused livers in Chapter V.

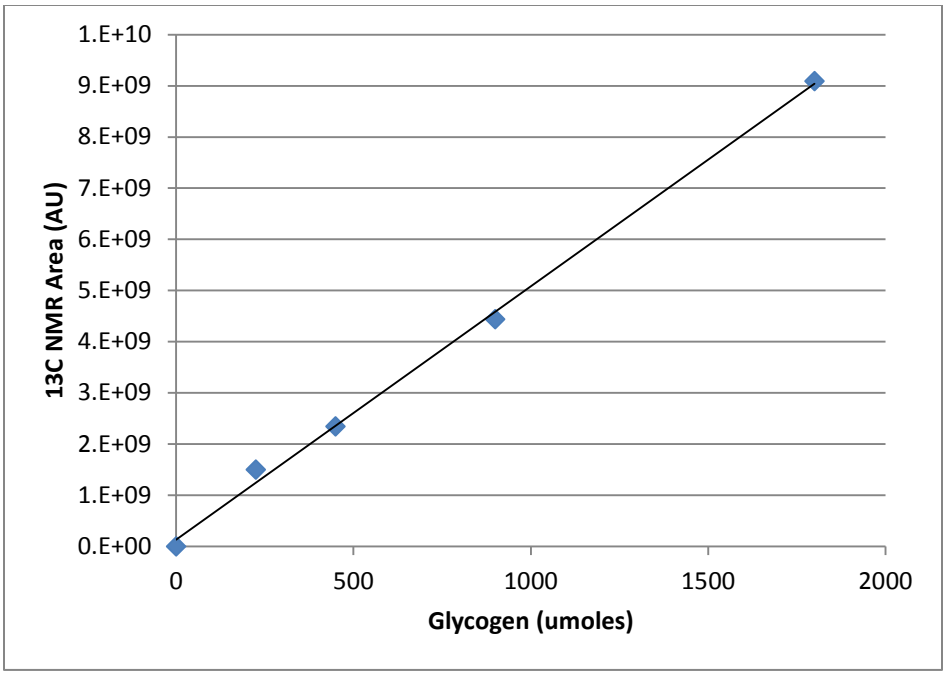

Figure 9. Calibration curve for total phantom glycogen and ^{13}C MRS signal.

Conclusion

These phantom studies demonstrate that it is possible to obtain acquisition parameters which result in a linear relationship between total phantom glycogen over the expected physiological range and the MTR_{asym} AUC derived from CEST Z-spectra. This suggests that these parameters will be suitable for the measurement of total glycogen content in perfused livers as described in the next chapter.

CHAPTER 5

MEASUREMENT OF TOTAL GLYCOGEN IN PERFUSED LIVERS

Introduction

In this chapter I take the parameters found to be optimal for CEST detection of glycogen in phantoms from Chapter IV, and apply them to isolated perfused livers, in an attempt to measure total hepatic glycogen content non-invasively.

Methods

The animals were studied under the purview of an Institutional Animal Care and Use Committee, and all applicable regulations and laws pertaining to the use of laboratory animals were followed. The perfused liver procedure has been published in detail elsewhere (Cohen, 1987) and is summarized briefly here. C57/BL6 mice (3-6 months old) were fed either normal chow or a high fructose diet (Research Diets Inc. #124908i) for 4-7 days to elevate liver glycogen (Koo, 2008). Mice were anesthetized (Nembutal IP, 50 mg/kg) during the dark cycle. Following a laparotomy, the portal vein was exposed and cannulated, and the liver was excised and perfused with a pre-oxygenated Krebs-Henseleit bicarbonate buffered solution. The liver was then placed into a custom 20 mm NMR tube and the entire assembly was placed inside the NMR spectrometer. ^{31}P MRS was initially performed to assess liver viability via ATP and Pi levels. Following manual shimming adjustments (typical water ^{1}H linewidth = 30-50 Hz) and

centering of the water frequency, baseline ^{13}C MRS and CEST Z-spectra were acquired and followed by the addition of glucagon (100 pM) to the perfusate to stimulate glycogen breakdown and thereby provide a range of liver glycogen values to be measured in a single study. Interleaved ^{13}C MRS and CEST acquisitions were then performed until liver glycogen reached a level near the ^{13}C MRS detection limit, estimated to be ~50 µmoles. This protocol is shown in Figure 10. A total of 13 perfused liver studies were performed, with each study yielding 1-4 separate glycogen measurements (determined by the starting glycogen content, glycogen breakdown rate, and limit of detection).

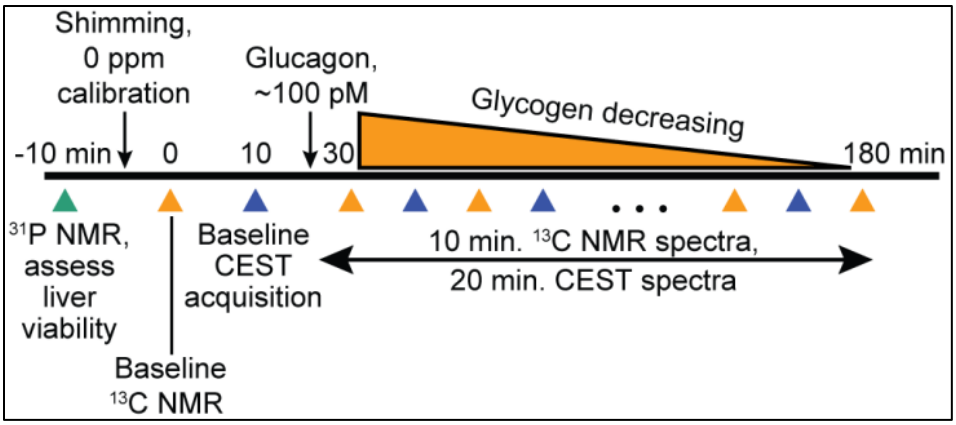

Figure 10. Interleaved CEST and ^{13}C MRS protocol used in perfused liver measurements of total liver glycogen.

Data analysis methods were identical to those already described in Chapter IV for the phantom studies, with the addition of computational simulations to estimate the inherent errors in each measurement method. As each liver started with a different glycogen level, the calculation of uncertainties with repeated measures was not feasible. As an alternative, I used Monte Carlo simulations based on the SNR of the ^{13}C

and ^{1}H spectra to generate standard deviations for each ^{13}C MRS and CEST measurement, respectively. For the ^{13}C MRS errors, a normal distribution with a mean of zero and standard deviation equal to the root mean square (RMS) noise of the ^{13}C MRS spectrum was created and random values from this distribution were added to each resonance. The total sum of the areas of the glycogen MRS peaks was then recalculated and this procedure was repeated 50,000 times to generate a distribution of ^{13}C MRS signal areas. The standard deviation of this distribution was used as the horizontal error bar in the plot of ^{13}C MRS determined glycogen versus CEST MTR_{asym} AUC. For the CEST errors, a normal distribution with a mean of zero and a standard deviation equal to the RMS noise of the individual ^{1}H MR spectra in the Z-spectrum was created and random values from this distribution were added to each resonance in the Z-spectrum. The integral of each resonance in the new Z-spectrum was then re-calculated and this new Z-spectrum was fit with an inverted Lorentzian model, from which the MTR_{asym} AUC could be re-calculated as described in the Chapter IV. This process was repeated 50,000 times to generate a distribution of MTR_{asym} AUC values and the standard deviation of this distribution was used as the vertical error bar in the plot of ^{13}C MRS determined glycogen versus CEST MTR_{asym} AUC.

The correlation between ^{13}C MRS determined glycogen and CEST MTR_{asym} AUC was then investigated by randomly choosing pairs of ^{13}C MRS determined glycogen values and CEST MTR_{asym} AUC values from each distribution for all perfused liver studies, performing a linear regression, and repeating for all 50,000 values in the respective distributions. In this way, distributions for the R^2, slope, and Y-intercept values characterizing this correlation could be formed and the standard deviations of

each was used as an estimate of the error in each of these parameters. This error simulation protocol is shown schematically in Figure 11.

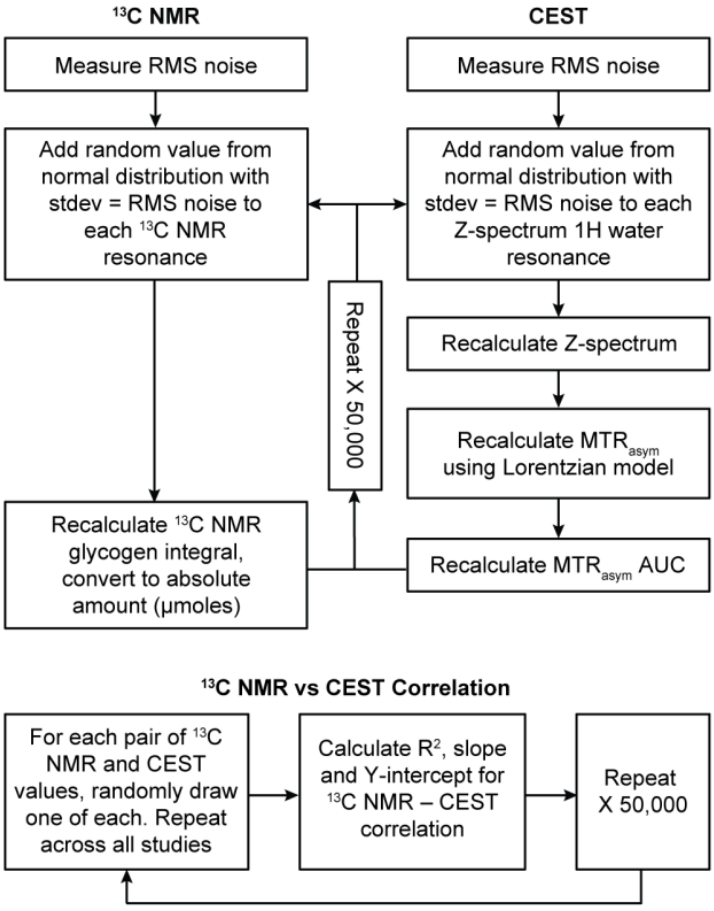

Figure 11. Monte Carlo simulation scheme to investigate the errors in the ^{13}C MRS and CEST measures of glycogen, and in the correlation of the two.

Results and Discussion

Figures 12A and 12B show raw ^{13}C NMR and CEST data, respectively, acquired in a selected perfused liver experiment. Here WE can see that the 100 pM dose of glucagon stimulated glycogen breakdown and served to efficiently generate a range of liver glycogen values in a single study. However since glucagon will also cause glucose

release from the liver, and since glucose hydroxyl protons have also been shown to have a CEST signal (van Zijl, 2012; Chan, 2012), there was likely to be additional CEST signal following glucagon administration. To account for this, data from all the perfused liver studies were separated into two groups, those acquired before glucagon addition and those acquired after glucagon addition.

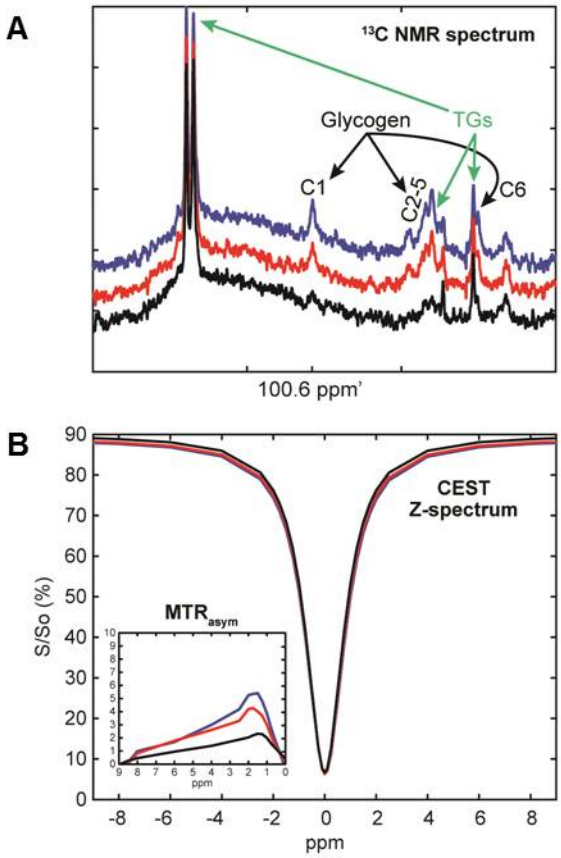

Figure 12. ^{13}C MRS (A) and CEST (B) data from a selected perfused liver study.

I also investigated which region of the MTR_{asym} curve would be optimal to use for correlation with the ^{13}C MRS data by comparing the R^2 value for the correlation between ^{13}C MRS determined glycogen and CEST MTR_{asym} AUC as different regions of the

MTR_{asym} curve were incorporated into the AUC calculation. Figure 13 shows the dependence of this R^2 value on which region of the MTR_{asym} curve was integrated (for fixed integration range of +2 ppm). Here we see that the region that produced the maximum R^2 value is [0.5 – 2.5 ppm] which is consistent with the glycogen hydroxyl protons being reported to resonate at approximately 1.2 ppm downfield from water (van Zijl, 2012).

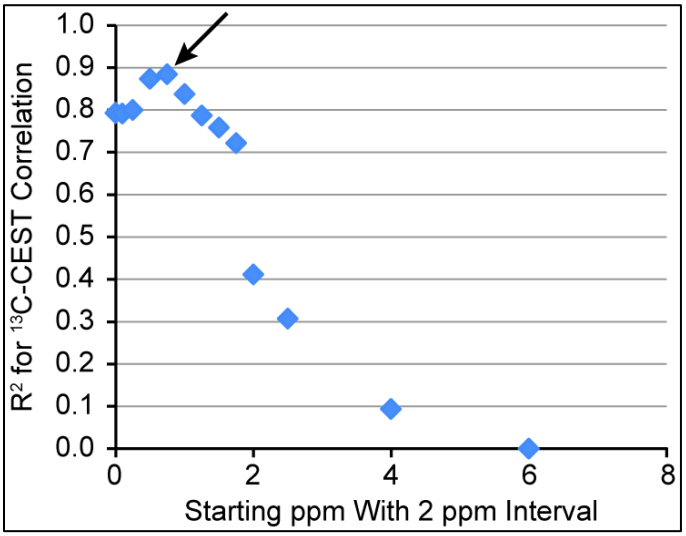

Figure 13. The dependence of R^2 for the ^{13}C MRS-CEST correlation on which region of the MTR_{asym} curve was used for the AUC calculation.

Figure 14 shows a plot of ^{13}C MRS determined glycogen versus CEST MTR_{asym} $AUC_{0.5\text{-}2.5}$ for data acquired before (blue) and after (red) glucagon. The R^2 values were 0.88 ± 0.054 and 0.87 ± 0.040, the slope values were 0.0091 ± 0.00078 and 0.0082 ± 0.00064, and the Y-intercept values were -0.50 ± 0.38 and 2.4 ± 0.21, respectively (mean ± SD). Error bars for the data points in Figure 14 as well for the standard deviations for the reported correlation parameters were determined by Monte Carlo

simulations described in Methods. I observed a strong linear relationship between ^{13}C MRS determined glycogen and CEST MTR_{asym} $AUC_{0.5\text{-}2.5}$ both before and after glucagon treatment. The slope of the relationship was similar in both groups as evidenced by the overlapping standard deviations. This slope value can be used in future studies as a calibration factor between CEST MTR_{asym} $AUC_{0.5\text{-}2.5}$ and total perfused liver glycogen. The fact that the Y-intercept is within two standard deviations of zero (i.e. not statistically different from zero) in the data obtained before glucagon addition demonstrates that there are few competing endogenous CEST metabolites in this spectral region of the liver. The increased Y-intercept value observed after glucagon addition is attributed to glucose release from the liver adding an additional CEST signal during this period of the experiment.

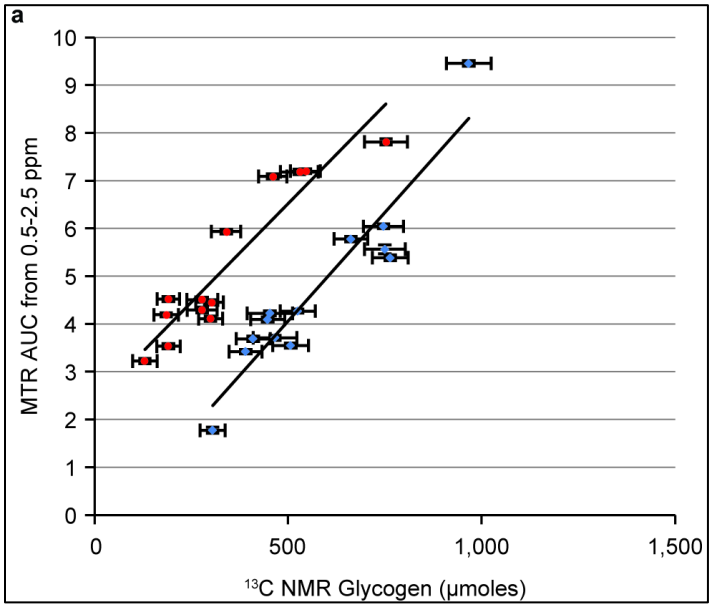

Figure 14. Correlation of CEST MTR_{asym} $AUC_{0.5\text{-}2.5}$ and ^{13}C MRS determined glycogen before (blue), and after (red) glucagon addition.

Interestingly, this glucose CEST signal is much higher than would have been predicted based on the expected perfusate glucose concentration of approximately 1 mM in the NMR tube (determined by the perfusion flow rate and observed glycogen breakdown rate), and differences in numbers of exchangeable hydroxyl protons between glucose and glycogen. I noted that while the linear relationship between total glycogen and CEST MTR_{asym} that was observed in phantoms was preserved in the perfused liver studies, the overall magnitude of the MTR_{asym} signal was reduced approximately by a factor of 4 in the perfused liver studies. Factors which could account for this are the lower water relaxation (T_{1w}) values in liver compared to in phantom solutions, differences in the molecular architecture of glycogen (e.g. branching patterns, number of tiers) in liver compared to in phantom solutions (oyster glycogen), and also the protein-bound nature of glycogen in tissue (Roach, 2012). The latter could reduce the CEST effect either directly by removing exchangeable glycogen hydroxyl protons or by altering the relaxation properties of the glycogen hydroxyl protons. This observation of reduced glycogen CEST signal in liver has two significant implications in the design of in vivo studies using CEST based measurements of tissue glycogen. Firstly, glycogen phantom solutions cannot be used to calibrate in vivo tissue glycogen measurements as is often done with the NMR detection of other metabolites/biomolecules. Secondly, the competing CEST signal from glucose represents a much larger potential hurdle than originally anticipated in the translation of this measurement to an in vivo setting (where glucose is always present in the liver). For example, a typical range of values for liver glycogen is 100 – 400 mM, while circulating glucose is generally near 5 mM. However, the 4-fold reduction of glycogen

signal in liver I observed combined with the approximate 2-fold reduction in exchangeable protons in glycogen suggests that *in vivo*, the glucose CEST signal can range from 10-40% of the glycogen CEST signal. As such, care must be taken to maintain glucose as constant as possible throughout an *in vivo* study to allow for specific detection of changes in the glycogen CEST signal. This implies that the use of CEST to measure absolute changes in liver glycogen *in vivo* would likely perform optimally with a glucose clamp protocol. It should be noted, however, that these studies were performed at 11.7 T which is much higher than most clinical MRI scanners. As such, it is possible that at lower fields where relaxation times are generally shorter, the amount of completing glucose CEST signal may be different.

The error bars for the plot shown in Figure 14, along with the errors reported for the R^2, slope, and Y-intercept values were determined by Monte Carlo simulations based on the respective SNR of the ^{13}C MRS glycogen spectra and ^{1}H Z-spectra. These error values allow us to estimate and compare the relative precision inherent to each approach. Defining the relative precision as the ratio of the dynamic range to the average error for each technique, I estimate values of 10:1 and 80:1 for ^{13}C MRS and CEST, respectively, implying that CEST is inherently ~8-fold more precise than natural abundance ^{13}C MRS. It is important to realize, however, that this calculation is based solely on the SNR of the original ^{1}H and ^{13}C spectra and it is likely that other experimental factors such as variations in shimming quality and variations in B_1 pulse power from experiment to experiment could reduce the precision of the CEST measurement. As a preliminary assessment of this, I studied a 40 mM glycogen phantom (prepared as described in Chapter IV) and measured the CEST MTR_{asym}

under the following three conditions: (1) optimal shimming (^{1}H line width = 40 Hz) with B_1 = 4 μT, (2) suboptimal shimming (^{1}H line width = 50 Hz) with B_1 = 4 μT, (3) optimal shimming with B_1 = 3.6 μT (i.e. a 10% error in the B_1 pulse). I found that case (2) produced an error in the CEST MTR_{asym} of ~5 % while case (3) produced an error of ~10%. Both of these errors are larger than the SNR-based errors estimated by the Monte Carlo simulations (~1-2%), demonstrating that variations in experimental parameters are likely to be the dominant source of error in CEST measurements of liver glycogen. In contrast, I routinely observe that errors in ^{13}C NMR measurements of glycogen are relatively insensitive to small variations in shimming and other experimental parameters, and are dominated mostly by the inherently low SNR of the ^{13}C nucleus.

Conclusion

These studies demonstrate that CEST can be used to measure total glycogen content in perfused livers and that CEST measurements of liver glycogen are inherently more precise than ^{13}C MRS. These studies also suggest that glucose may be a larger than anticipated confounding factor in the CEST detection of glycogen and that control over, or at least sampling of, glucose concentrations may be necessary for the translation of this approach *in vivo*.

CHAPTER VI

CEST MEASUREMENTS OF HEPATIC GLYCOGEN SYNTHESIS IN PERFUSED LIVERS

Introduction

In the previous chapter, I demonstrated that CEST methods could be used to measure total liver glycogen content. Here, I seek to apply this approach to the measurement of hepatic glycogen synthesis rates in perfused livers.

Methods

The same general perfused liver procedure as described in Chapter V was used with the addition of 15 mM [1-^{13}C] glucose to the perfusate to be used as a substrate for glycogen synthesis. The use of the ^{13}C label also affords the ability to use interleaved ^{13}C MRS measurements as before, but now with increased sensitivity and decreased acquisition time. The overall protocol for this is shown below in Figure 15.

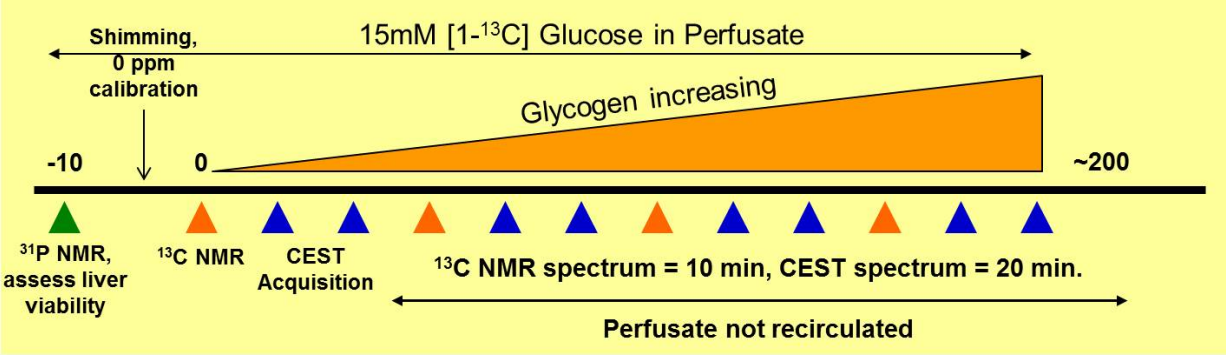

Figure 15. Protocol for measurement of glycogen synthesis rates in perfused livers using ^{13}C MRS and CEST.

As before, livers from lean non-fasted C57 mice were used and the experimental conditions were varied by adding known effectors of glycogen synthesis to generate a range of hepatic glycogen synthesis rates, and also to generate data for statistical power calculations. In the first set of studies, livers were harvested from mice either in the middle of the light cycle (expected to have lower glycogen synthesis) or dark cycle (expected to have increased glycogen synthesis) and perfused with [1-^{13}C] glucose alone, and also with 1mM fructose for mice taken during the dark cycle (expected to have further increased glycogen synthesis). In the second set of studies, livers harvested from mice taken in the middle of the dark cycle were perfused with varying concentrations of glucagon which is expected to inhibit glycogen synthesis.

The data analysis methods were similar to those described in Chapter 5 except for the omission of Monte Carlo error simulations which were unnecessary due to the ability to use repeated trials under identical conditions. ^{13}C spectral integrals were calculated for each time point and converted to absolute glycogen amounts using the calibration curve shown in Figure 9. CEST Z-spectra and MTR_{asym} curves were

calculated as before and numerically integrated from [0 – 6 ppm] and this MTR_{asym} AUC was converted to an absolute glycogen amount using an analogous curve to that in Figure 14, determined now by integrating the MTR_{asym} curve from [0 – 6 ppm] instead of [0.5 – 2.5 ppm] as in Chapter 5. Subtraction of baseline signals resulted in plots of the increment in absolute amount of glycogen versus time for each measurement method, and the average slope of each was calculated to yield independent measures of glycogen synthesis in units of μmoles/min. This protocol is shown for a selected study in Figure 16 below.

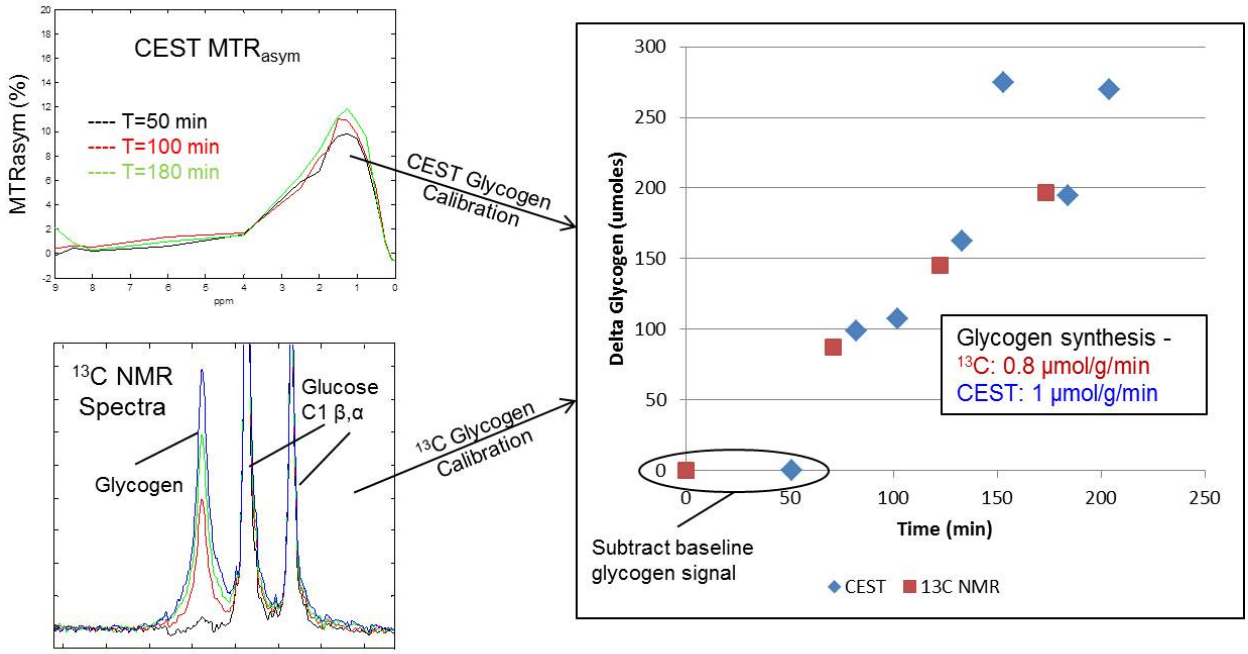

Figure 16. Data analysis protocol for the calculation of rates of glycogen synthesis from ^{13}C MRS and CEST measurements.

Results and Discussion

Data from the first set of studies is shown in Figure 17 which demonstrates that 1mM fructose increases glycogen synthesis, while harvesting the livers in the middle of

the light cycle decreases glycogen synthesis (two-factor ANOVA $P < 0.0001$, no difference between ^{13}C MRS and CEST). These data were then used to develop a power calculation to determine approximate samples sizes needed to detect changes in glycogen synthesis. For this calculation, the following values were used: mean value of glycogen synthesis = 0.55; average standard deviation = 0.2; expected change in glycogen synthesis with treatment = 0.3. The results of this are shown in Table 1 for a two-sided analysis assuming a confidence level of $\alpha = 0.05$.

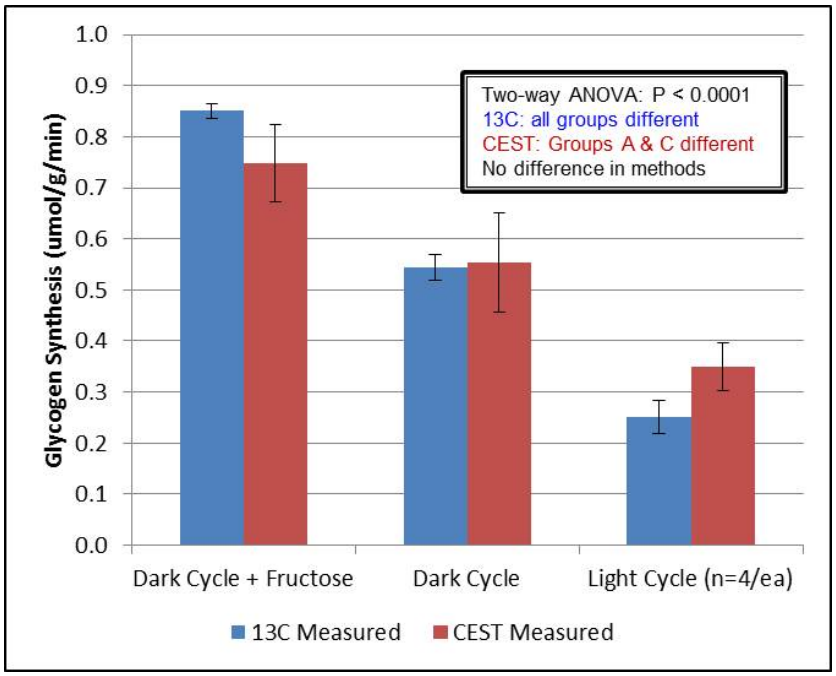

Figure 17. CEST and ^{13}C MRS measurements of glycogen synthesis rates for perfused livers with different starting conditions.

Power Level	# of Studies (n)
0.7	3
0.75	4
0.8 (typically chosen)	4
0.85	4
0.9	5

Table 1. Power calculation for sample size requirements to detect changes in glycogen synthesis rates with CEST based on data from Figure 17.

The data from the glucagon titration is shown in Figure 18. As expected, glucagon dose-dependently reduced glycogen synthesis and both the 3 pM and 10 pM were significantly different from no glucagon (0 pM), and also different from each other (two-factor ANOVA $P < 0.0001$, no difference between ^{13}C MRS and CEST).

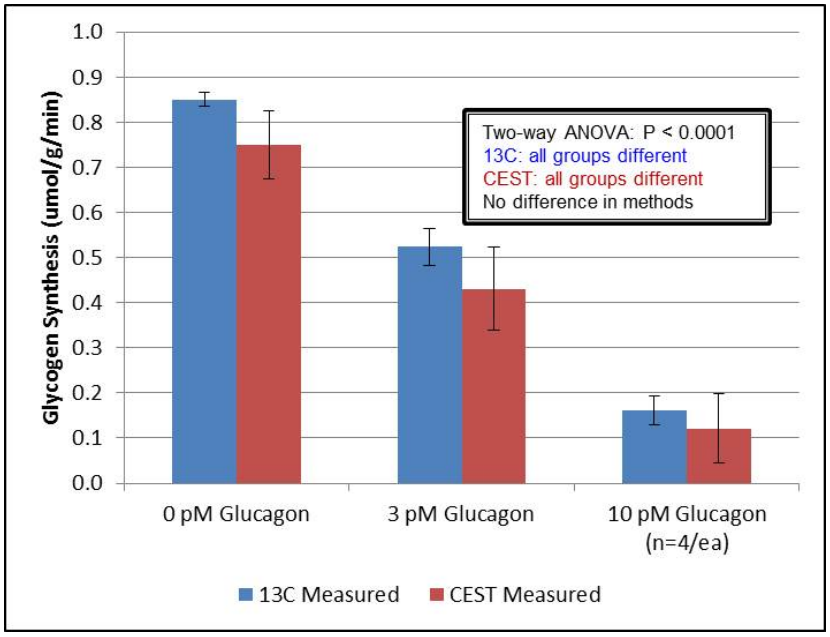

Figure 18. The effects of glucagon on hepatic glycogen synthesis ex-vivo.

These two data sets confirm that CEST has sufficient sensitivity to detect physiologically relevant changes in glycogen synthesis. Interestingly, the error bars (SEMs) for the CEST measurements tended to be larger than those for the ^{13}C MRS measurements in these studies. This is in contrast to what was observed in the previous set of studies described in Chapter V where total glycogen levels were measured. This is likely due to two factors. First, ^{13}C labeled glucose was used here which enhanced the SNR of the glycogen NMR signal approximately 10-fold. Second, the changes in the CEST signal due to glycogen synthesis were superimposed on top of an already large CEST signal from the 15mM glucose in the perfusate. As demonstrated in Chapter 5, small variations in experimental parameters are likely to be the dominant source of error in CEST measurements, and since the overall CEST signal is larger in this set of studies, these experimental errors are larger than what would be expected due the CEST signal from glycogen alone.

The correlation between the CEST and ^{13}C MRS measurements of glycogen synthesis is shown in Figure 18. The slope and Y-intercept of this relationship was 0.88 +/- .31 and 0.042 +/- 0.16 (95% confidence intervals), respectively. That the slope is close to unity and the Y-intercept is close to zero confirm that CEST can accurately measure glycogen synthesis rates. The overall R^2 value for this relationship is 0.65 which is not as strong as that obtained in the measurements of total glycogen levels alone. This is most likely due to the increased error in the CEST measurements as described above.

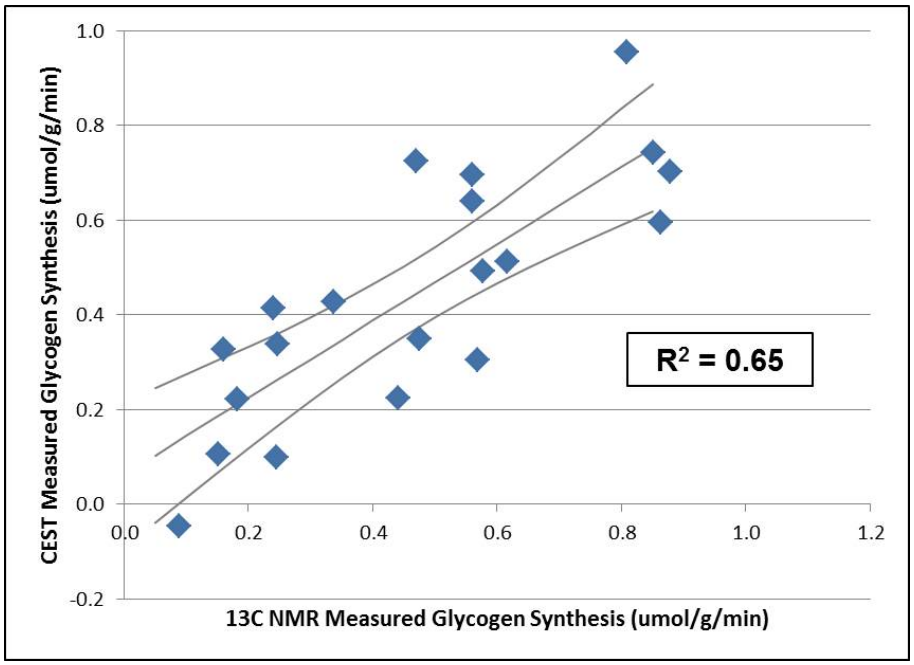

Figure 19. Correlation of ^{13}C MRS and CEST measurements of glycogen synthesis.

Conclusion

These studies demonstrate that CEST can be used to measure glycogen synthesis rates in perfused livers and also can likely be used to detect changes in glycogen synthesis rates with a reasonable number of subjects (4-5) per group. Errors in CEST measurements of glycogen synthesis are larger than those observed with ^{13}C MRS, likely due to the large perfusate concentrations of glucose needed to stimulate glycogen synthesis.

CHAPTER VII

EFFECTS OF AMPK ACTIVATION ON HEPATIC GLYCOGEN SYNTHESIS

Introduction

In the previous chapter, I demonstrated that CEST can be used to measure rates of glycogen synthesis in perfused livers, and that this technique has sufficient precision to detect physiologically relevant changes in these rates. I now apply this methodology to investigate a novel pharmacological question, the effects of acute activation of AMPK on hepatic glycogen synthesis.

AMPK Biology

AMPK is currently one of the most actively investigated areas of both molecular biology and pharmacology. Activation of AMPK (by various means) has been shown to have various effects in metabolic tissues, generally stimulating catabolic, ATP-generating pathways while inhibiting anabolic, ATP-consuming pathways . This is achieved by direct phosphorylation of regulatory proteins and also by indirect effects on gene expression. For this reason, the enzyme had been colloquially called a 'metabolic master switch' (Winder, 1999). A summary of the known effects of AMPK along with upstream effectors of its activity effects are shown in Figure 20 below.

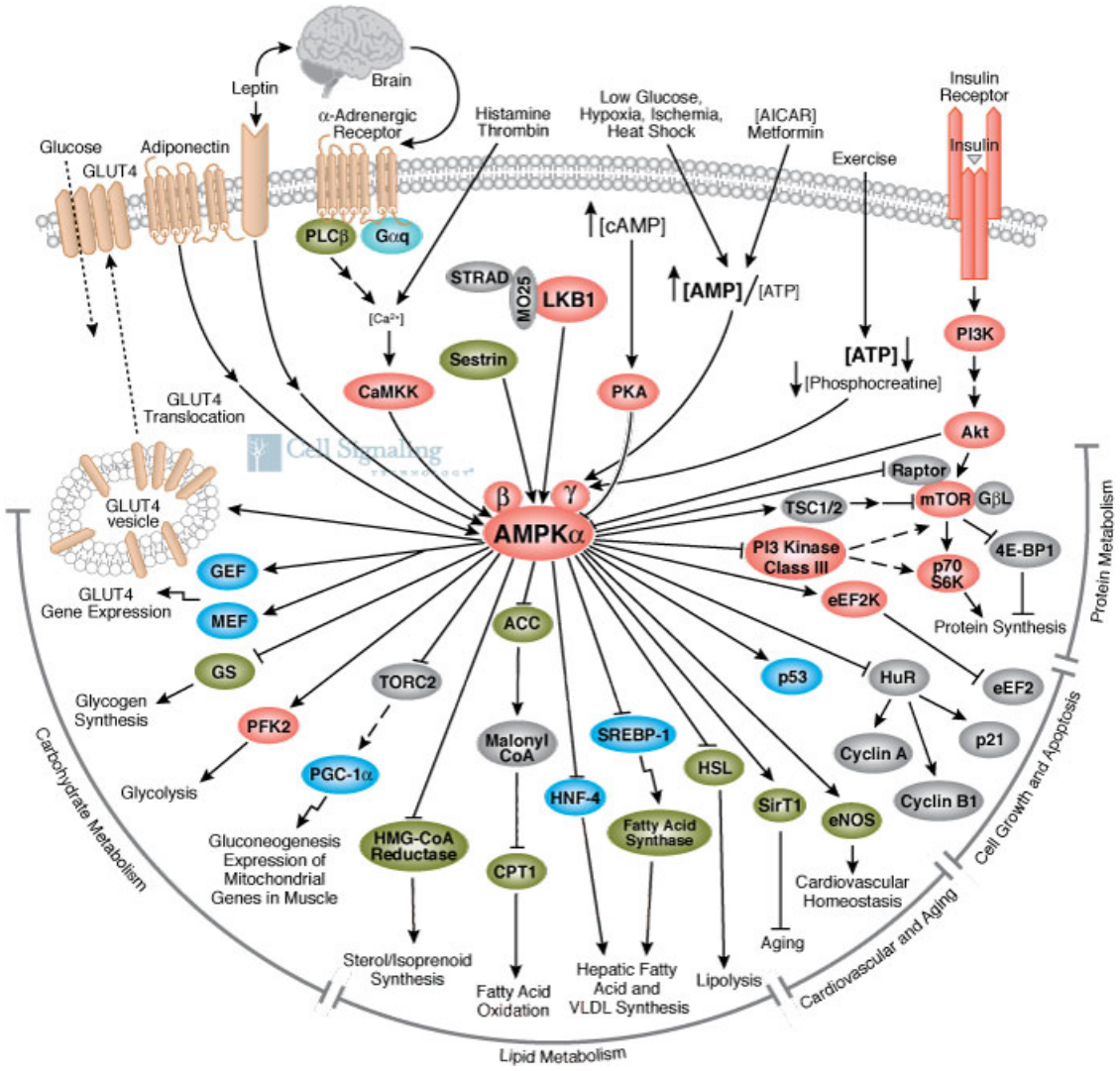

Figure 20. The influence of AMPK on various metabolic pathways.

Despite a wealth of literature, there are still many challenges and caveats in our current knowledge of AMPK. Firstly, the main pharmacological tool which has been employed to activate AMPK, 5-aminoimidazole-4-carboxyamide-riboside (AICAR), works by intracellular conversion to an AMP analog (zMP), and thus raises the effective AMP/ATP ratio rather than activating the AMPK enzyme directly. AICAR has relatively

poor potency (in vitro studies typically use concentrations ~ 1mM) for AMPK activation, and has also been shown to stimulate GPase and inhibit *fructose-1,6-bisphosphatase* (Vincent, 1991; Longus, 2003). The therapeutic effects of Metformin were initially thought to be mediated via AMPK (Zhou, 2001), however recent work has demonstrated that Metformin is still able to suppress glucose output in hepatocytes derived from AMPK and LKB1 (an upstream regulator of AMPK) KO mice (Foretz, 2010). Secondly, many studies have manipulated AMPK activity via alterations in the initial state of the subjects, (e.g. fed vs. fasted rodents, exercised/contracted vs. rested muscle). While the results of these efforts can be used to glean correlative changes between AMPK activity and enzyme/pathway effects, direct causality cannot be assumed as these initial alterations can certainly have many effects beyond AMPK alone. Lastly, much of our knowledge of AMPK is derived from measured effects at the level of mRNA or protein expression. While changes at this level may translate to changes in enzyme activity and pathway flux in vivo, a linear relationship is not necessarily guaranteed.

With respect to glycogen metabolism, AMPK has been demonstrated to phosphorylate, and therefore inhibit, both liver and muscle glycogen synthase in vitro (Bultot, 2012, Carling, 1989). Paradoxically, however, it was recently demonstrated that activation of AMPK with AICAR resulted in increased skeletal muscle glycogen levels in mice (Hunter, 2011). Further work using site-directed mutagenesis showed that the allosteric activation of glycogen synthase by G6P was required for this effect. AMPK increases glucose transport in skeletal muscle but not in liver, and because skeletal muscle *hexokinase* has a very low K_m compared to liver GK (~0.1mM vs. ~10mM, respectively), it is entirely possible that liver and muscle G6P levels may differ

significantly following AMPK activation. This, in turn, may result in potentially very different GSase and GPase activities, and hence different rates of glycogen synthesis. This illustrates that changes in glycogen metabolism can be difficult to predict as they represent the integrated sum of many different effectors, and that methods for direct measurement of glycogen like ^{13}C MRS or CEST are necessary to understand the dynamics of glycogen metabolism. The goal of this portion was to investigate the acute effects of AMPK activation on hepatic glycogen synthesis.

Description of Small Molecule AMPK Activator

For these studies the compound MK8722 was chosen as an activator of AMPK. The structure of MK8722 is shown in below in Figure 21.

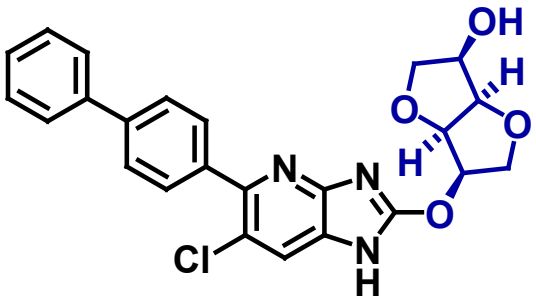

Figure 21. Chemical structure of small molecule AMPK activator MK8722.

The in vitro profile for MK8722 against all 12 isoforms of AMPK is shown in in Table 2 as EC_{50} values along with the maximal activation of the enzyme in parentheses. Of particular interest for these studies are isoforms 1 and 7 which are the primary liver

isoforms, and the low EC_{50} values of 1 and 2 nM, respectively, confirm excellent potency of this compound against these isoforms.

Isoform	Subunits	Human	Mouse	Rhesus
		EC50 nM (%act)		
AMPK1	α1β1γ1	1 (328%)	1 (447%)	1 (1209%)
AMPK2	α1β1γ2		2 (293%)	1 (963%)
AMPK3	α1β1γ3	4 (1519%)	3 (678%)	1 (472%)
AMPK4	α1β2γ1	51 (874%)	25 (529%)	27 (1058%)
AMPK5	α1β2γ2	63 (440%)	22 (216%)	21 (668%)
AMPK6	α1β2γ3	29 (849%)	20 (354%)	16 (588%)
AMPK7	α2β1γ1	2 (518%)	1 (541%)	1 (587%)
AMPK8	α2β1γ2	6 (625%)	2 (538%)	1 (407%)
AMPK9	α2β1γ3	4 (2026%)	5 (2353%)	2 (540%)
AMPK10	α2β2γ1	50 (293%)	34 (558%)	36 (357%)
AMPK11	α2β2γ2	56 (240%)	28 (315%)	23 (254%)
AMPK12	α2β2γ3	15 (2111%)	26 (2400%)	15 (625%)

Table 2. In vitro potencies of AMPK activator MK8722 against all the isoforms of AMPK for different species.

One of the proximal targets of AMPK is the enzyme *acetyl CoA carboxylase* (ACC) which is a key step in de novo lipogenesis (DNL), and the phosphorylation of ACC (pACC) has been widely used as an indicator of AMPK activation (i.e. target engagement). Figure 22A shows that following a 10 mg/kg oral dose of MK8722, levels of liver pACC were elevated (Merck – unpublished data). Analysis of plasma samples

from this study showed that levels of MK8722 were approximately 10 μM. Data from a separate study examining the effects of MK8722 on DNL in primary hepatocytes is shown in Figure 22B and confirms that maximal effect of MK8722 is achieved at concentrations of approximately 10 μM (Merck – unpublished data). Hence for the current perfused liver studies, a perfusate dose of 10 μM for MK8722 was chosen.

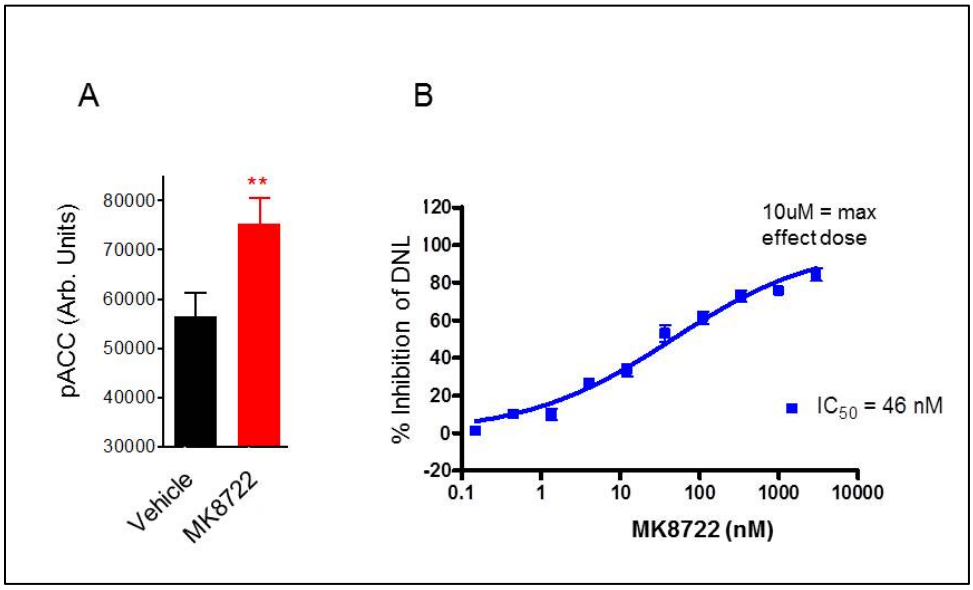

Figure 22. Effects of MK8722 on pACC *in vivo* (A), and on DNL *in vitro* (B).

Methods

The overall perfused liver protocol used was similar to that described in Chapter VI. Livers from lean C57 mice were harvested in the middle of the dark cycle and perfused with 15 mM [1-^{13}C] glucose and either 10 μM MK8722 or 0.1% DMSO (the solvent used for making stock solution of MK8722). Glycogen synthesis was then measured using interleaved ^{13}C MRS and CEST methods as described in Chapter VI. It

is important to note that the data shown in Figure 17 confirms that this approach and these conditions have the potential to show either an increase or decrease in glycogen synthesis and thus I have not biased the study towards any one particular effect.

Results and Discussion

The results of this study are shown in Figure 23. Here we see again excellent agreement between the CEST and ^{13}C MRS measurements, and that MK8722 acutely inhibits glycogen synthesis (two-factor ANOVA, P = 0.0003, no difference in ^{13}C MRS and CEST). Hepatic ATP levels were measured using ^{31}P MRS at the beginning and end of the each study and MK8722 had no effect on these, indicating that effects on glycogen synthesis were unlikely to be due to toxicity. In separate perfused liver studies performed at Merck, MK8722 at 10 μM was shown to acutely reduce hepatic DNL from ^{13}C-pyruvate, consistent with the primary hepatocyte data shown in Figure 22, and further confirming target engagement of AMPK at this perfusate concentration. Taken together, these findings demonstrate that acute AMPK activation in liver reduces glycogen synthesis.

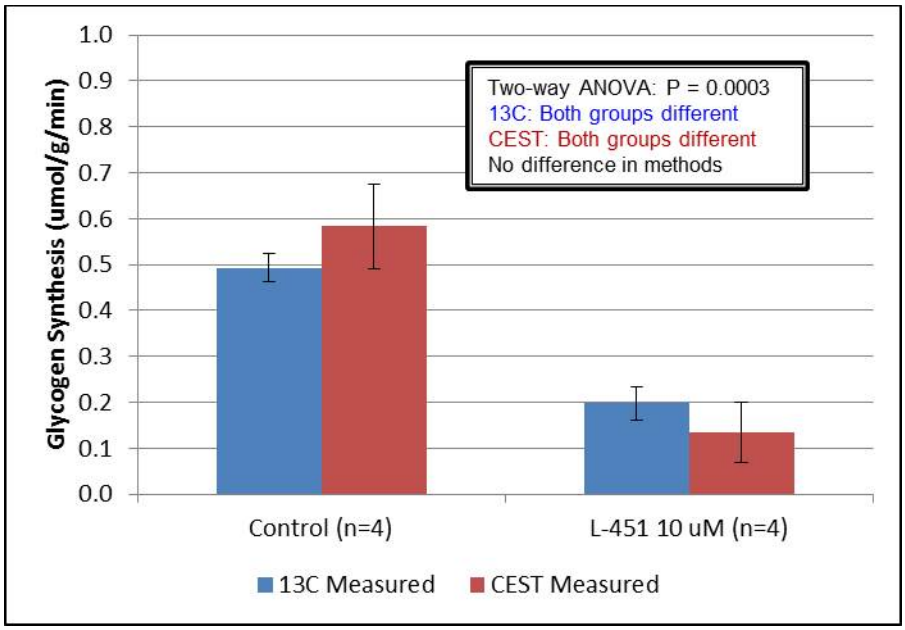

Figure 23. The acute effects of AMPK activation on hepatic glycogen synthesis as measured with CEST and ^{13}C MRS.

This is an interesting finding as it is the opposite effect as was reported in muscle (Hunter, 2011). This is likely because while AMPK activation directly increases glucose uptake via GLUT4 translocation in muscle, no such effect is likely to be seen in liver as GLUT2 is embedded in the cell membrane and is not known to be directly affected by AMPK. Thus, while in muscle the increased intracellular levels of glucose and G6P may override the inhibitory effects of AMPK on GSase, no such mechanism occurs in liver and the result is an inhibition of glycogen synthesis due to direct phosphorylation and inhibition of GSase by AMPK. This finding is also consistent with other reports of associations between AMPK activation and reductions in hepatic glycogen synthesis observed in response to hepatic glycogen loading (Winnick, 2011) and elevated hepatic nitric oxide levels (An, 2010).

A reduction in glycogen synthesis is the opposite effect as seen with two other drug targets (GK activators and GP inhibitors) which are known to ameliorate hyperglycemia, at least in preclinical models. While at first this suggests that hepatic AMPK activation may not have a favorable therapeutic effect for diabetes, it must be remembered that AMPK has been reported to have many other hepatic and extra-hepatic effects which are likely to be beneficial such as reduction of fatty liver (Viollet, 2006), increased muscle glucose uptake (Sakoda, 2002), and reduced hepatic gluconeogenesis (Viollet, 2006), although the latter still remains a topic of debate.

Conclusion

These studies demonstrate that acute activation of AMPK with MK8722 reduces hepatic glycogen synthesis. This result also demonstrates that CEST measurements of glycogen synthesis rates are of sufficient precision to detect physiologically relevant changes in response to pharmacological effectors.

CHAPTER VIII

PILOT CEST MRI IMAGING MEASUREMENTS OF GLYCOGEN SYNTHESIS *IN VIVO* AT 7T

Introduction

The good overall performance of CEST in terms of measuring both total glycogen content and glycogen synthesis rates described in the two previous chapters suggested that it may be possible to develop a protocol to measure glycogen synthesis rates in vivo. I report here the preliminary results of this effort.

Methods

Phantom Studies – As a preliminary check that the CEST acquisition parameters used in the previous studies were appropriate for use at 7T, I prepared glycogen phantoms as described in Chapter IV at concentrations of 100 mM, 200 mM, and 400 mM in 5 mm NMR tubes. These were then arranged horizontally in a 7T Bruker MRI system and Z-images were acquired by using a RARE imaging sequence (parameters described in the next section) with CEST saturation pulses at offsets identical to those used in the previous perfused liver studies.

MRI Acquisitions – For both the phantom and in vivo studies at 7T, a 30 mm quadrature volume coil was used in a Bruker 7T MRI equipped with Paravision 6. After typical adjustments (tuning, shimming, pulse power calibrations), T_1-weighted RARE

images were acquired initially to ensure appropriate placement in the coil. CEST Z-images were then acquired using a block saturation pulse (4 uT, 500 ms) in combination with a RARE imaging sequence (64 x 64 pixels, RARE factor = 32, centric encoding, TR/TE = 20 sec / 5 msec, total acquisition time ~ 20 min).

Animal Protocol – Lean C57 mice were anesthetized in the middle of the light cycle with 3% isoflurane and a tail vein cannula was inserted and used to take a baseline blood glucose measurement. Mice were then transferred to a heated holder and inserted into a Bruker 7T horizontal MRI equipped with a 30 mm volume coil and respiratory monitoring and localizer images combined with T_1-weighted RARE images with coronal slices were used to position the liver at magnet center. Respiratory-gated CEST acquisitions were then performed on a 2 mm slice encompassing as much liver as possible while remaining at a sufficient distance from the lungs and stomach. Saturation offsets were as follows: [12, 6, 3, 2, 1.75, 1.5, 1.25, 1, 0.75, 0.5, 0.4, 0.3, 0.25, 0.2, 0.15, 0.1, 0.5, 0, 100 ppm] which resulted in a total acquisition time of 25 min. The additional saturation offsets were added around 0 ppm to allow for more accurate centering of the Z-spectrum over the slice. The larger offset of the reference frequency (100 ppm) was due to the observation of overall reduction of signal intensity in the Z-spectrum and as a result, the 40 ppm offset previously used no longer yielded the plateau value of the Z-spectrum. I attribute this overall decrease in Z-spectrum intensity at higher frequency offsets to the increased amount of general magnetization transfer (MT) in vivo. After an initial baseline CEST image was acquired, an I.V. infusion of [1-^{13}C] glucose consisting of a 1 g/kg bolus over 10 minutes followed by a 10 mg/kg/min slow infusion was administered via the tail vein. This was accompanied by four

additional serial respiratory-gated CEST image acquisitions of ~25 min each. The in vivo protocol is shown below in Figure 24.

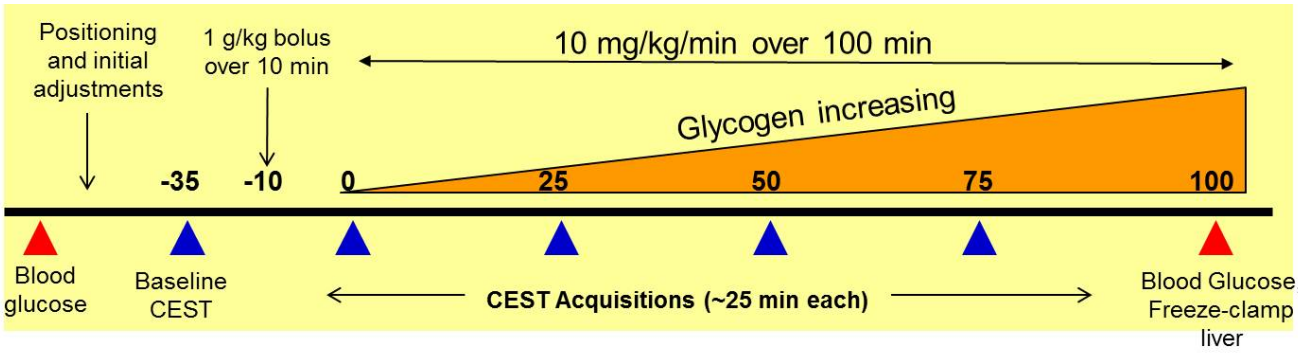

Figure 24. Protocol for in vivo glycogen synthesis CEST studies.

Data Analysis – Image processing was performed offline using Matlab functions. To accurately correct for variations in B_0, additional saturation offsets were included around 0 ppm and the Z-spectrum for the following subset of saturation offsets was fit to an inverted Lorentzian model as described in Chapter IV to estimate the 0 ppm shift: [±0.4, ±0.3, ±0.25, ±0.2, ±0.15, ±0.1, ±0.05, 0, -0.5, -0.75, -0.1, -1.25, -1.5, -1.75, -2, -3 ppm]. This procedure was chosen over performing a single field map or WASSR-type scan (Kim, 2009) at the beginning of the study because the B_0 inhomogeneity may change over the course of a study and this current approach allows each Z-image to be corrected for 0 ppm variation independently. The saturation offsets were then shifted and the Z-spectrum was corrected by linear interpolation. This correction procedure is illustrated for a single Z-spectrum in Figure 25 below.

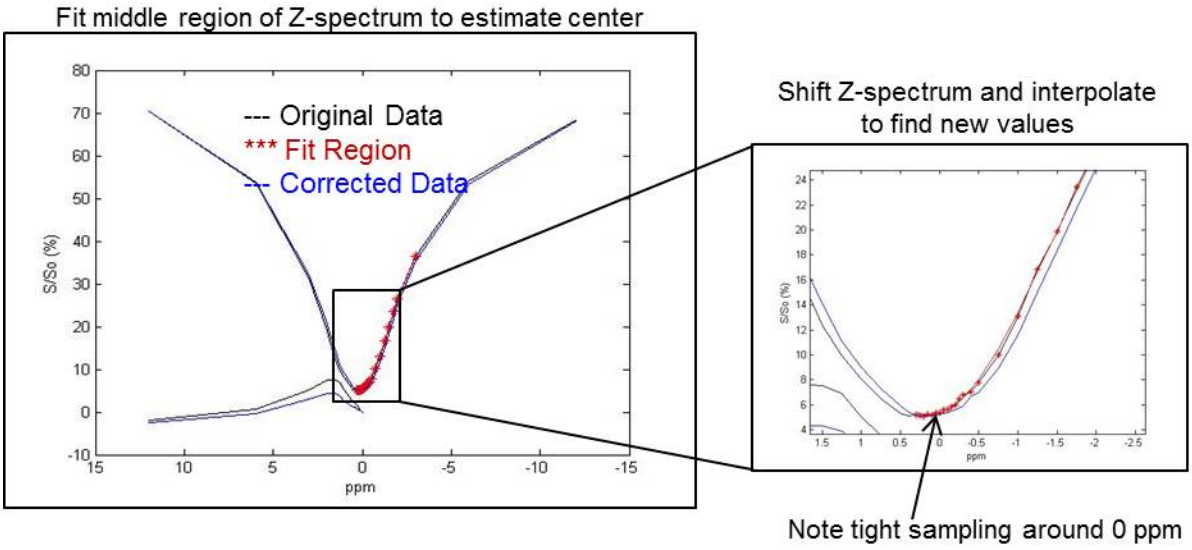

Figure 25. Illustration of procedure used to correct for B_0 inhomogeneity and variation in 0 ppm.

Two different approaches were used to analyze the CEST image data. In the first approach, analysis was performed on a region of interest (ROI) in the liver selected from the reference CEST image. To calculate average glycogen synthesis rates, ROIs were drawn over the homogeneous portions of the CEST image and Z-spectra were constructed from the average intensities in the ROI. Once corrected for any 0 ppm variation using the fitting procedure described above, the MTR_{asym} function was calculated using the traditional method (eq.1) and was integrated over the region [0.5 – 2.5 ppm] to yield an AUC value. The baseline AUC value was then subtracted and a plot of ΔMTR_{asym} versus time was constructed. This process is shown for a sample study using two ROIs in Figure 26 below.

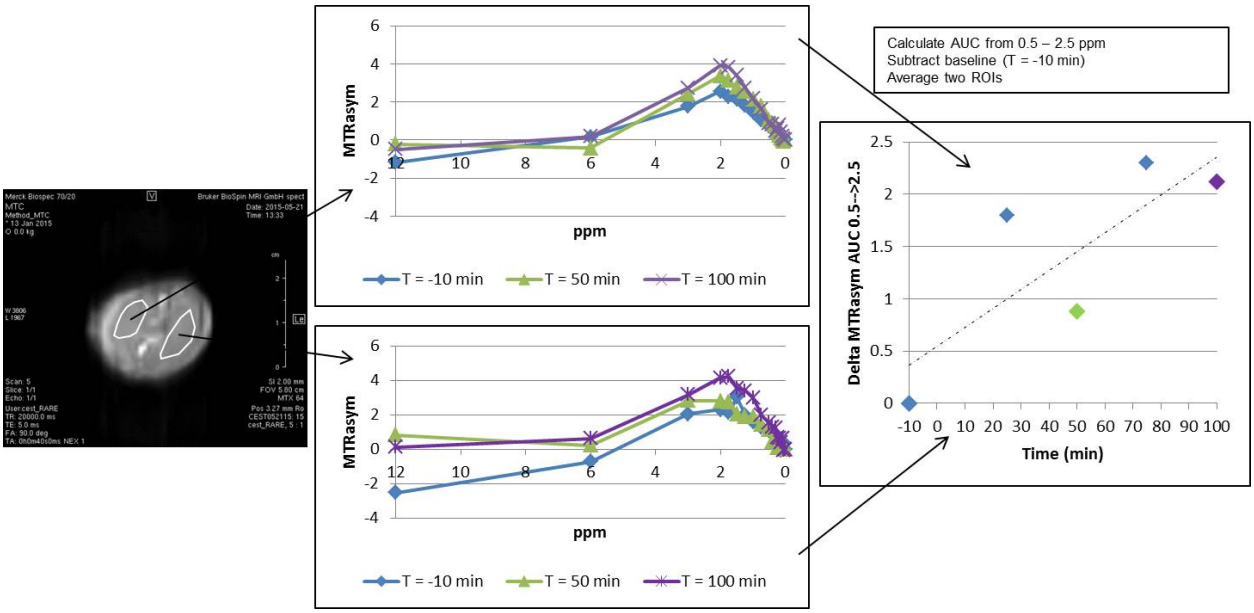

Figure 26. Illustration of the analysis method to calculate the change in the MTR_{asym} AUC over time starting with two ROIs drawn on the CEST image.

In the second analysis approach, calculations were performed on a pixel by pixel basis starting with the CEST Z-images. Here, a 3D matrix (size = 64 x 64 x # of offsets) was constructed corresponding to the individual CEST images acquired at various frequency offsets and the 0 ppm correction described above was applied to the Z-spectrum from each pixel. The MTR_{asym} function and its AUC from [0.5 – 2.5] were then calculated for each pixel and finally, the slope of the MTR_{asym} AUC versus time was calculated for each pixel. This procedure is shown for a selected study in Figure 27 below.

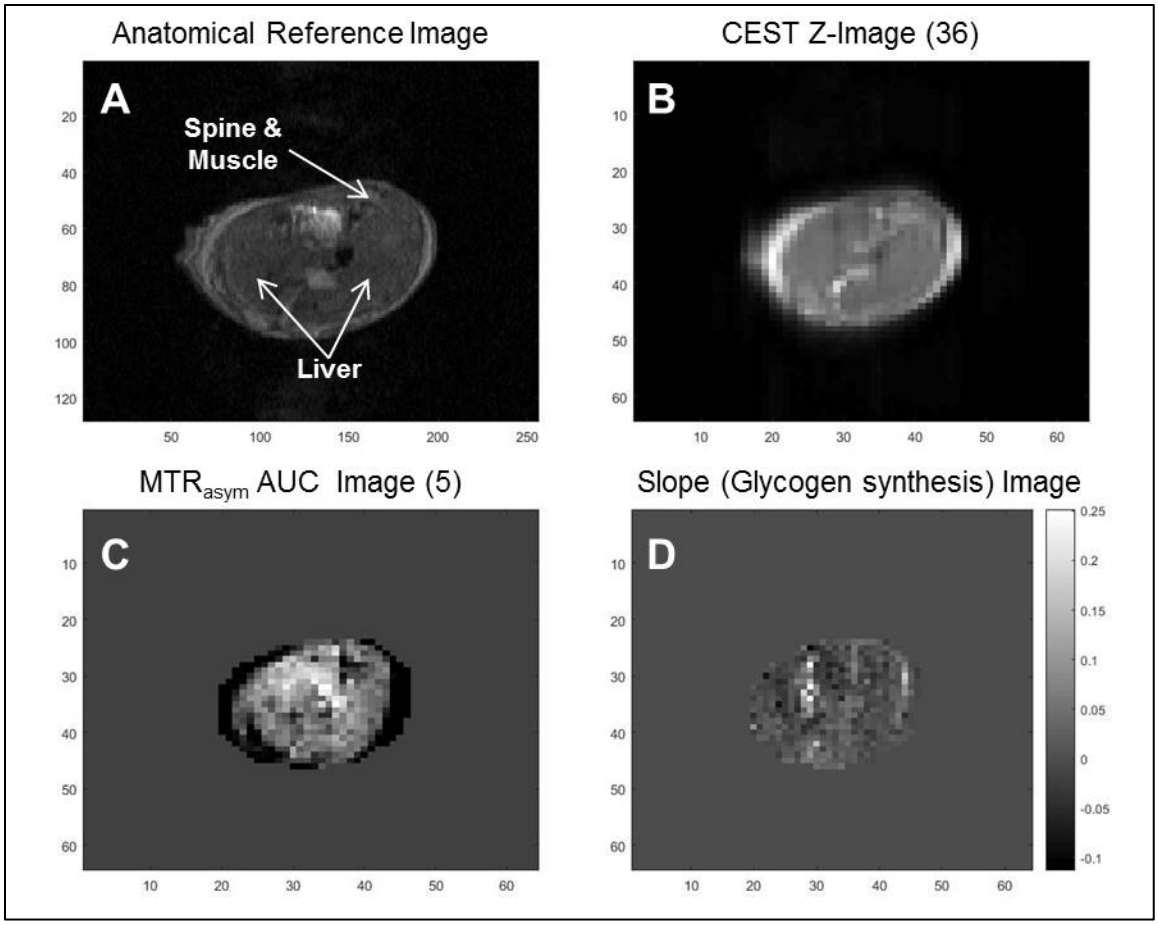

Figure 27. Illustration of pixel by pixel analysis protocol. The anatomical image (A) is used to locate different organs. The 36 CEST Z-images (B) acquired at different frequency offsets are used to calculate each MTR_{asym} AUC image (C). The five MTR_{asym} AUC images acquired over time were then used to calculate the slope image (D) which reflects glycogen synthesis. Axes denote pixel number with a field of view of 50 mm for each image.

Results and Discussion

Phantom Studies – Data from the phantom studies is shown below in Figure 28. Panel (A) shows CEST images at +1 ppm and -1 ppm offsets. Note that the difference in intensity is greatest for the 400 mM glycogen phantom and least for the 100 mM phantom. Panel (B) shows the Z-spectrum for a circular ROI positioned on each phantom. Panel (C) shows the MTR_{asym} plot for the ROIs and panel (D) shows a plot of

MTR_{asym} AUC versus glycogen concentration. The high degree of linearity of this relationship confirms that the CEST acquisition parameters used are suitable for detection of glycogen in the physiological range.

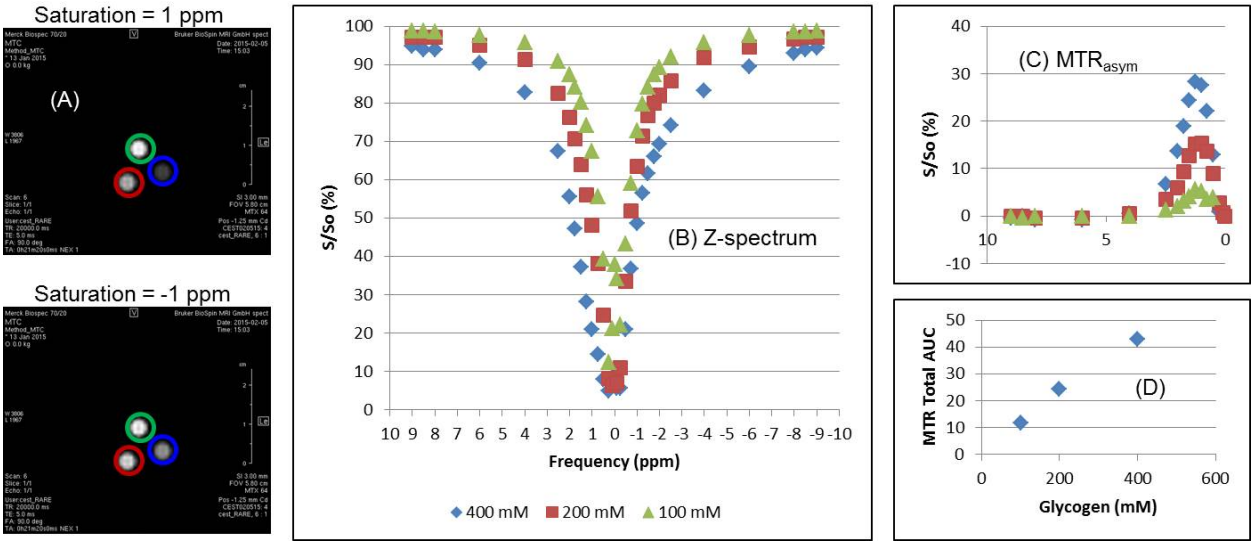

Figure 28. Data from glycogen phantom studies at 7T. (A) CEST images for saturation offsets of +1 ppm and -1 ppm. (B) Z-spectra corresponding to the ROIs in (A). (C) MTR_{asym} curves calculated from each Z-spectrum. (D) Relationship of MTR_{asym} AUC versus phantom glycogen concentration.

<u>In Vivo Studies</u> – Figure 29 below shows a sample coronal respiratory gated T1-weighted RARE image along with the CEST slice used for this subject and the corresponding axial image for this slice.

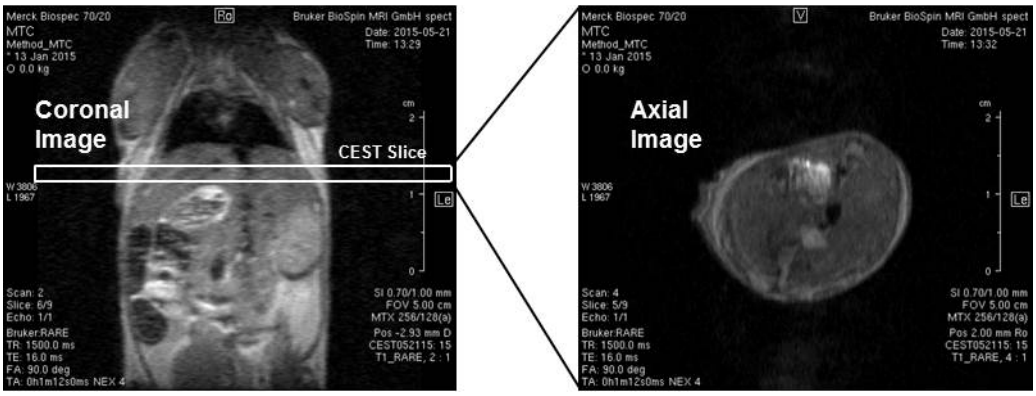

Figure 29. Sample anatomical images and CEST slice used for this subject.

Figure 30 below shows the blood glucose before and after the infusion protocol, confirming that the infusion raised the blood glucose level approximately 3-fold to a final value of ~450 mg/dl. Previous perfused liver studies have shown that glycogen synthesis rates plateau at approximately 300-350 mg/dl, which suggests that glycogen synthesis was maximally activated throughout these studies.

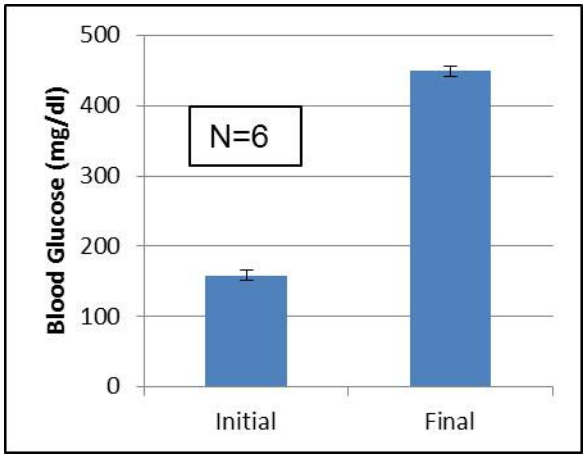

Figure 30. Blood glucose concentrations at the beginning and end of the glucose infusion protocol.

Figure 31 below shows a plot of average (n = 4) changes in MTR_{asym} versus time using the first analysis protocol based on the average CEST signal intensities from RIOs in the liver. Here WE see that, despite some variation in individual data points, the MTR_{asym} still increases over time as would be expected with increasing glycogen levels. The slope of this line is 0.011 MTR_{asym} AUC/min.

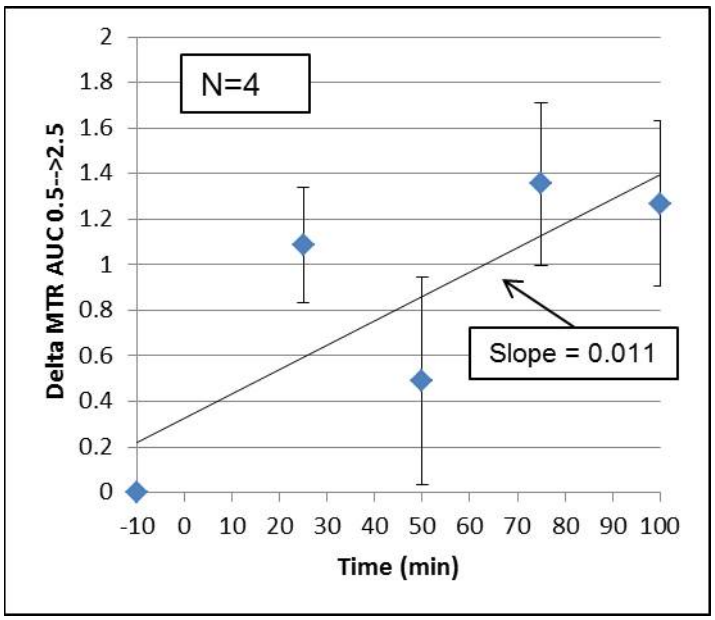

Figure 31. Average increase of MTR_{asym} $AUC_{0.5\text{-}2.5}$ over time *in vivo*.

Sample results of the second analysis protocol using pixel by pixel calculations were shown in Figure 27, starting from the anatomical image through the CEST Z-image, MTR_{asym} AUC images, and the final slope image which reflects glycogen synthesis. As a consistency check for this analysis method, three ROIs were selected for the slope image in each study, two for regions within the liver and one for the area of the spinal cord and paraspinal muscles. The average slope was calculated for each

ROI and the results are shown below in Figure 32. The average slope value of 0.0093 MTR_{asym} AUC/min for the liver regions is consistent with the slope value from Figure 31 and is significantly different from values obtained from ROIs drawn around the region containing the spine and paraspinal muscles ($P < 0.01$, t-test).

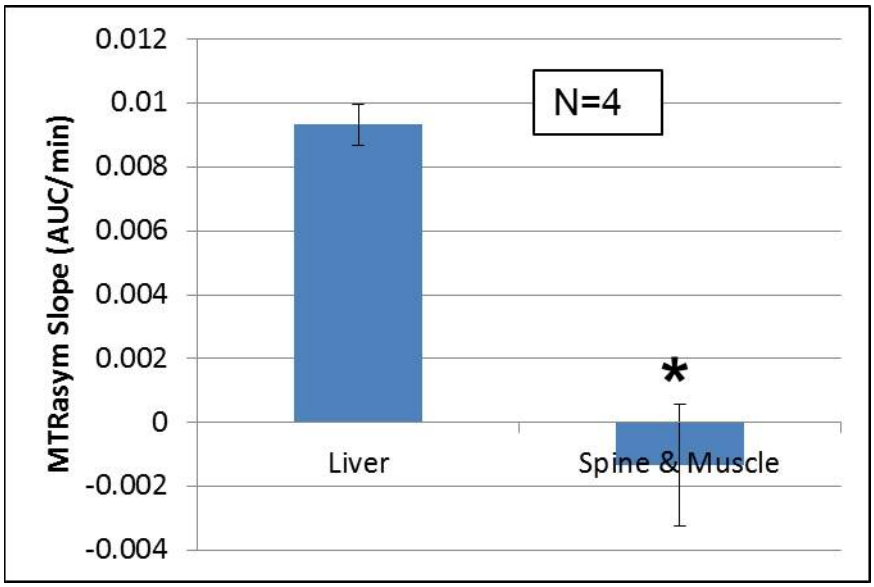

Figure 32. Comparison of slope of the MTR_{asym} $AUC_{0.5\text{-}2.5}$ versus time for ROIs containing the liver or the spine and paraspinal muscles.

While it is natural to attribute the observed increase in MTR_{asym} solely to glycogen synthesis, it must be remembered that glucose is also elevated over the course of the study and thus could theoretically contribute to the increased MTR_{asym}, especially since I have no knowledge of the circulating glucose time course profile over the study. This appears to be unlikely, however, for three reasons. First, since glucose in infused intravenously, circulating glucose should also be increased and the spine and paraspinal muscle regions, yet there is no increase CEST MTR_{asym} over time in these regions (Figure 33). Second, if glucose was responsible for the majority of the MTR_{asym}

signal, then after the initial glucose bolus infusion (which is expected to increase glucose 2-3 fold, the total MTR_{asym} should increase accordingly. Looking at Figure 26, however, we see from T = -10 min to T = 50 min there is only a modest increase in the MTR_{asym}. Third, glucose has significant MTR_{asym} signal at +3 ppm (van Zijl, 2007) while glycogen does not, and thus if responsible for the increase in MTR_{asym}, we would expect to see a pronounced increase in the MTR_{asym} at +3 ppm after the glucose bolus. Figure 26 again shows that this is not the case.

Conclusion

The results of this chapter demonstrate that detection and MRI imaging of hepatic glycogen synthesis in vivo using CEST is feasible. While there is much work that could to be done in terms of optimizing the image acquisition protocol (e.g. tighter sampling around 0 ppm to improve the correction, optimization of TR to reduce acquisition time and improve temporal resolution), these results lay the groundwork for future translation of this methodology into larger animals and humans.

CHAPTER IX

SUMMARY AND FUTURE DIRECTIONS

In this work, I have addressed the question of whether CEST methods can be used to reliably measure hepatic glycogen levels and synthesis rates over the physiological range. Using model glycogen solutions, I found that with appropriate choice of acquisition parameters, CEST measurements of total glycogen were linearly related to total phantom glycogen content. Applying these same acquisition parameters to perfused livers treated ex-vivo with glucagon to generate a range of glycogen values in a single study, I then showed that CEST measures of total liver glycogen content were strongly correlated with interleaved ^{13}C MRS measurements. This demonstrated that CEST can reliably report glycogen content in a whole, functional liver. Monte Carlo simulations of intrinsic errors in each method revealed that CEST was more precise than ^{13}C MRS from an SNR standpoint, however it may be more susceptible to errors induced by variations in experimental parameters (e.g. shimming, B_0 variation).

I then adapted the perfused liver protocol to stimulate hepatic glycogen synthesis by adding high concentrations of [1-^{13}C] glucose to the perfusate. Under these conditions, and with the addition of effectors of hepatic glycogen synthesis (fructose, glucagon) to the perfusate, I found that the MTR_{asym} AUC from serially acquired CEST spectra increased over time and this rate of increase was correlated with glycogen synthesis rates derived from interleaved ^{13}C MRS measurements. I also found that errors in CEST-derived measures of glycogen synthesis rates were larger than those

derived from ^{13}C MRS measurements, though some of this was likely to be from the contaminating CEST signal from the high concentration of glucose in the perfusate. This finding was in contrast to what was observed in the measurements of total hepatic glycogen content, where CEST was shown to be inherently more precise.

I then applied this platform for the measurement of glycogen synthesis rates to a novel pharmacological question, the effect of AMPK activation on hepatic glycogen synthesis. Using a small molecule AMPK activator shown to be highly potent in vitro and to have good target engagement in vivo, I found that acute activation of AMPK inhibits hepatic glycogen synthesis, a result in contrast to a recently published finding in skeletal muscle. This finding demonstrated that CEST measures of glycogen synthesis were of sufficient precision to detect changes in glycogen synthesis rates induced by a novel effector, and that glycogen metabolism is quite different in liver and muscle, and that changes in net glycogen synthesis cannot always be predicted from in vitro results alone. An interesting follow up study would be to investigate hepatic glycogen synthesis rates after *chronic* treatment with the same AMPK activator in perfused livers from a mouse model of diabetes. This would probe the question of whether the additional beneficial effects of long term AMPK activation (e.g. reduction of liver triglycerides, lowering of circulating glucose via increased skeletal muscle glucose uptake) have additional effects on hepatic glycogen metabolism beyond the acute effects resulting from the direct inhibition of GSase by AMPK.

After demonstrating that CEST could accurately measure glycogen synthesis rates in perfused livers, I then developed an in vivo protocol at 7T to stimulate hepatic glycogen synthesis using I.V. glucose infusions in anesthetized mice. With appropriate

modifications to acquisition parameters to reflect the need for spatial correction of B_0 variation, I were able to show that the CEST MTR_{asym} signal in liver regions increased over time during the glucose infusion, while the CEST MTR_{asym} signal from regions containing the spine and surrounding paraspinal muscles did not. This was demonstrated by two types of analysis, one on single Z-spectra derived from ROIs in the initial liver CEST image, and the other on ROIs in the liver after pixel by pixel calculation of MTR_{asym} AUC and slope versus time.

While measurement of total glycogen levels and glycogen synthesis rates in perfused livers has been well worked out in these studies, much more work is needed in the development of CEST based measures of glycogen metabolism in vivo. One of the obvious shortcomings of our infusion protocol is the lack of knowledge of blood glucose concentrations between the start and end of the study. This can be remedied by the use of surgically implanted sampling lines. Currently, this is beyond our technical expertise due to the physical constraints of our 7T magnet room, however I acknowledge that future studies will eventually require this capability and a solution will need to be developed.

In this work I increased hepatic glycogen synthesis in vivo with an IV glucose infusion, and observed a subsequent increase in the MTR_{asym} signal over time. An obvious next step would be to replace the glucose infusion with a glucagon infusion (or injection) to stimulate glycogen breakdown and then to attempt to measure that decrease in glycogen over time with CEST. This would demonstrate that CEST can measure bidirectional changes in liver glycogen. Additional studies could then modify the glucose infusion protocol by either adding fructose (to increase glycogen synthesis

further) or by systematically lowering the glucose infusion rate to yield different levels of hyperglycemia, and accordingly, different rates of glycogen synthesis. This would address the precision of in vivo CEST measurements of glycogen synthesis and would allow for the use of power calculations to determine sample sizes required to detect certain changes in glycogen synthesis rates. Interesting initial applications of this approach to pathology would be in cases of a known focal lesion in the liver, such as a tumor or cirrhosis. As glycogen synthesis would likely be reduced in those regions, they would serve a positive control for known alterations in glycogen synthesis and could be used to assess the spatial sensitivity of this approach.

Improvements in the CEST MRI acquisition parameters and analysis methods will also likely be required to maximize the utility of this approach and afford the highest probability of success for translation to larger species. In these studies, I used very long TR values to ensure complete longitudinal relaxation. This, however, results in long acquisition times (20-25 min/image) which can be problematic in large, free-breathing subjects, especially when multiple images need to be acquired over time to calculate a glycogen synthesis rate. B_0 inhomogeneity may also present issues when translating this approach to larger species. I found that B_0 generally varied by less than ±0.5 ppm over a mouse liver using a small (30 mm) volume coil. The larger imaging coils required for use with larger subjects, however, may have more B_0 variation. While in theory this can always be accounted for by using the correction procedure described here, along with the addition of more saturation offsets over the expected range of B_0 variation, this too could add significant time to each image acquisition.

In summary, this work expands upon the initial detection of the glycogen CEST signal, and lays the foundation for the use of CEST to probe glycogen metabolism in isolated tissues and in vivo. While there are still hurdles, both known and possibly unknown, to overcome in the application of this methodology to larger species, I remain optimistic that these issues will be tractable, and that this approach will eventually yield a greater understanding of glycogen metabolism in both normal and pathological states.

REFERENCES

Agius, L. (2008) Glucokinase and molecular aspects of liver glycogen metabolism. *Biochem J*, **414**, 1-18.

An, Z., Winnick, J. J., Farmer., Neal, D., Lautz, M., Irimia, J., Roach, P. J., Cherrington, A. D. (2010) A Soluble Guanylate Cyclase–Dependent Mechanism Is Involved in the Regulation of Net Hepatic Glucose Uptake by Nitric Oxide in Vivo. *Diabetes*, **59**, 2999-3007.

Avison, M. J., Rothman, D. L., Nadel, E., Shulman, R. G. (1988) Detection of human muscle glycogen by natural abundance 13C NMR. *Proc Natl Acad Sci*, **85**, 1634-1636.

Baker, D. J., Greenhaff, P. L., Timmons, J. A., (2006) Glycogen phosphorylase inhibition as a therapeutic target: a review of the recent patent literature. *Expert Opin. Ther. Patents*, **16**, 459-466.

Bultot, L., Guigas, B., Von Wilamowitz-Moellendorff, A., Maisin, L., Vertommen, D., Hussain, N., Beullens, M., Guinovart, J. J., Foretz, M., Viollet, B., Sakamoto, K., Hue, L., Rider, M. H. (2012) AMP-activated protein kinase phosphorylates and inactivates liver glycogen synthase. *Biochem J*, **443**, 193-203.

Cai, K., Haris, M., Singh, A., Kogan, F, Greenberg, J. H., Hariharan, H., Detrem, J. A., Reddy, R. (2012) Magnetic resonance imaging of glutamate. *Nature Med* **18**, 302-307.

Carling D., Hardie D. G. (1989) The substrate and sequence specificity of the AMP-activated protein kinase. Phosphorylation of *glycogen synthase* and *phosphorylase kinase*. *Biochim Biophys Acta*, **1012**, 81–86.

Caro, J. F., Triester, S., Patel, V. K., Tapscott, E, B., Frazier, N. L., Dohm, G. L. (1995) Liver glucokinase: decreased activity in patients with type II diabetes. *Horm Metab Res*, **27**, 19–22.

Chan, K. W. Y., McMahon, M. T., Kato, Y., Liu, G., Bulte, J. W. M., Bhujwalla, Z. M., Artemov, D., van Zijl, P. C. M. (2012) Natural D-Glucose as a biodegradable MRI contrast agent for detecting cancer. *Mag Res Med*, **68**, 1764-1773.

Cherrington, A. D. (1999) Control of glucose uptake and release by the liver in vivo. *Diabetes,* **48**, 1198-1214.

Choi, I. Y., Gruetter, R., (2003) In vivo 13C NMR assessment of brain glycogen concentration and turnover in the awake rat. *Neurochem Int*, **43**, 317-22.

Choi, J. M., Seo, M, H.,Kyeong, H. H., Kim, E., Kim, H.S. (2013) Molecular basis for the role of glucokinase regulatory protein as the allosteric switch for glucokinase. *Proc Natl Acad Sci*,**110**, 10171-10176.

Chu, C. A., Sindelar, D. K., Neal, D. W., Allen, E. J., Donahue, E. P., Cherrington, A. D. (1997) Comparison of the direct and indirect effects of epinephrine on hepatic glucose production. *J Clin Invest*, **99**, 1044–1056.

Chu, C. A., Sindelar, D. K., Neal, D. W., Allen, E. J., Donahue, E. P., Cherrington, A.D. (1998) Effect of a selective rise in sinusoidal norepinephrine on HGP is due to an increase in glycogenolysis. *Am J Physiol*, **274**, E162-171.

Cline, G. W., Magnusson, I., Rothman, D. L., Petersen, K. F., Laurent, D., Shulman, G. I. (1997) Mechanism of impaired insulin-stimulated muscle glucose metabolism in subjects with insulin-dependent diabetes mellitus. *J Clin Invest*. **99**, 2219–2224.

Cohen, S.M. (1987) 13C and 31P NMR study of gluconeogenesis: utilization of 13C-labeled substrates by perfused liver from streptozotocin-diabetic and untreated rats. *Biochemistry*, **26**, 563-572.

Daw, C. J., Lefer, A. M., Berne, R. M. (1968) Influences of Corticosteroids on Cardiac Glycogen Concentration in the Rat. *Circ Res*, **22**, 639-647.

Eldar-Finkelman, H., Ilouz, R. (2003) Challenges and opportunities with glycogen synthase kinase -3 inhibitors for insulin resistance and Type 2 diabetes treatment. *Expert Opinion Invest Drugs,* **12**, 1511-1519.

Fontana, J. D. (1980) The presence of phosphate in glycogen. *FEBS Lett*, **109**, 85-92.

Foretz, M., Hébrard, S., Leclerc, J., Zarrinpashneh, E., Soty, M., Mithieux, G., Sakamoto, K., Andreelli, F., Viollet B. (2010) Metformin inhibits hepatic gluconeogenesis in mice independently of the LKB1/AMPK pathway via a decrease in hepatic energy state. *J Clin Invest*, **120**, 2355-2369.

Forsén, S., Hoffman, R. A. (1963) Study of Moderately Rapid Chemical Exchange Reactions by Means of Nuclear Magnetic Double Resonance. *J Chem Phys*, **39**, 2892-2901.

Goldsmith, E., Sprang, S. and Fletterick, R. (1982) Structure of maltoheptaose by difference Fourier methods and a model for glycogen. *J Mol Biol*, **156**, 411-427.

Gunja-Smith, Z., Marshall, J. J., Mercier, C., Smith, E. E. and Whelan, W. J. (1970) A revision of the Meyer–Bernfeld model of glycogen and amylopectin. *FEBS Lett,* **12**, 101-104.

Gruetter, R., Prolla, T. A., Shulman, R. G. (1991) 13C NMR visibility of rabbit muscle glycogen in vivo. *Mag Res Med*, **20**, 327-332.

Gruetter, R., Magnusson, I., Rothman, D. L., Avison, M. J., Shulman, R. G., Shulman, G. I. (1994) Validation of 13C NMR measurements of liver glycogen in vivo. *Mag Res Med*, **31**, 583–588.

Hardie, D. G. (2008) AMPK: a sensor of glycogen as well as AMP and ATP? *Proc Physiol Soc*, **12**, SA10.

Haschke, R. H., Heilmeyer, L. M., Meyer, F. and Fischer, E. H. (1970) Control of phosphorylase activity in a muscle glycogen particle. III. Regulation of phosphorylase phosphatase. *J Biol Chem*, **245**, 6657-6663.

Hansen, B. F, Asp, S., Kiens, B., Richter, E. A. (1999) Glycogen concentration in human skeletal muscle: effect of prolonged insulin and glucose infusion. *Scand J Med Sci Sports*, **9**, 209-13.

Heilmeyer, L. M., Meyer, F., Haschke, R. H. and Fischer, E. H. (1970) Control of phosphorylase activity in a muscle glycogen particle. II. Activation by calcium. *J Biol Chem*, **245**, 6649-6656.

Hellerstein, M. K., Xie Y. (1993) The indirect pathway of hepatic glycogen synthesis and reduction of food intake by metabolic inhibitors. *Life Sci*, **53**, 1833-45.

Henquin, J. C. (2000) Triggering and amplifying pathways of regulation of insulin secretion by glucose. *Diabetes*, **49**, 1751–1760.

Huang, M. T., Veech, R. L. (1988) Role of the direct and indirect pathways for glycogen synthesis in rat liver in the postprandial state. *J Clin Invest*, **81**, 872–878.

Hudson, E. R., Pan, D. A., James, J., Lucocq, J. M., Hawley, S. A., Green, K. A., Baba, O., Terashima, T. and Hardie, D. G. (2003) A novel domain in AMP-activated protein kinase causes glycogen storage bodies similar to those seen in hereditary cardiac arrhythmias. *Curr Biol*, **13**, 861-866.

Hunter, R. W., Treebak, J. T., Wojtaszewski, J.F., Sakamoto, K. (2011) Molecular mechanism by which AMP-activated protein kinase activation promotes glycogen accumulation in muscle. Diabetes, 60, 766-774.

Hwang, J. H., Perseghin, G., Rothman, D. L., Cline, G. W., Magnusson, I., Petersen, K. F., Shulman, G. I. (1995) Impaired Net Hepatic Glycogen Synthesis in Insulin-dependent Diabetic Subjects during Mixed Meal Ingestion: A 13C Nuclear Magnetic Resonance Spectroscopy Study. *J Clin Invest*, **95**, 783-787.

Iynedijan, P. B. (1993) Mammalian glucokinase and its gene. *Biochem J*, **293**, 1-13.

Jensen, J., Jebens, E., Brennesvik, E. O., Ruzzin, J., Soos, M.A., Engebretsen, E. M., O'Rahilly, S., Whitehead, J. P. (2006) Muscle glycogen inharmoniously regulates glycogen synthase activity, glucose uptake, and proximal insulin signaling. *Am J Physiol Endocrinol Metab*, **290**, E154-E162.

Jiang G., Zhang B. B. (2003) Glucagon and regulation of glucose metabolism. *Am J Physiol Endocrinol Metab*, **284**, E671-678.

Jue, T., Lohman, J. A. B., Ordidge, R. J., Shulman, R. G. (1987) Natural abundance 13C NMR spectrum of glycogen in humans. *Mag Res Med*, **5**, 377-379.

Jue, T., Rothman, D. L., Tavatian, B. A., Shulman, R. G. (1989) Natural abundance 13C NMR study of glycogen repletion in human liver and muscle. *Proc Natl Acad Sci*, **86**, 1439-1442.

Jue, T., Rothman, D. L., Shulman, G. I., Tavatian, B. A., DeFronzo, R. A., Shulman, R. G. (1989) Direct observation of glycogen synthesis in human muscle with 13C NMR. *Proc Natl Acad Sci*, **86**, 4489-4491.

Jurczak, M. J., Danos, A. M., Rehrmann, V. R., Allison, M. B., Greenberg, C. C., Brady, M. J., (2007) Transgenic overexpression of protein targeting to glycogen markedly increases adipocytic glycogen storage in mice. *Am J Physiol Endocrinol Metab*, **292**, E952–E963.

Kim, M., Gillen, J., Landman, B. A., Zhou, J., van Zijl, P. C. M. (2009) Water saturation shift referencing (WASSR) for chemical exchange saturation transfer (CEST) experiments. *Mag Res Me*d, **61**, 1441-1450.

Kirkman, B. R., Whelan, W. J. and Bailey, J. M. (1989) The distribution of glucosamine in mammalian glycogen from different species, organs and tissues. *Biofactors,* **2**, 123-126.

Kirkman, B. R. and Whelan, W. J. (1986) Glucosamine is a normal component of liver glycogen. *FEBS Lett*, **194**, 6-11.

Kogan, F., Haris, M., Sing, A., Cai, K., Debrosse, C., Nanga, R. P. R., Hariharan, H., Reddy, R. (2014) Method for high-resolution imaging of creatine in vivo using chemical exchange saturation transfer. *Mag Res Med*, **71**, 164-172.

Koo, H., Wallig, M. A., Chung, B. H., Nara, T. Y., Cho, B. H. S., Nakamura, M.T. (2008) Dietary fructose induces a wide range of genes with distinct shift in carbohydrate and lipid metabolism in fed and fasted rat liver. *Biochim Biophys Acta*, **1782**, 341–348.

Ling, W., Regatte, R., Navon, G., Jerschow, A. (2008) Assessment of glycosaminoglycan concentration in vivo by chemical exchange-dependent saturation transfer (gagCEST). *Proc Natl Acad Sci*, **105**, 2266-2270.

Lomako, J., Lomako, W. M., Kirkman, B. R. and Whelan, W. J. (1994) The role of phosphate in muscle glycogen. *Biofactors,* **4**, 167-171.

Longo, D. L., Sun, P. Z., Consolino, L., Michelotti, F. C., Uggeri, F., Aime, S. (2014) A General MRI-CEST Ratiometric Approach for pH Imaging: Demonstration of in Vivo pH Mapping with Iobitridol. *J Am Chem Soc*, **136**, 14333–14336.

Longus, S. L., Wambolt, R. B., Parsons, H. L., Brownsey, R. W., Allard, M. F. (2003) 5-Aminoimidazole-4-Carboxaimde 1-beta-D-ribofuranoside (AICAR) stimulates myocardial glycogenolysis by allosteric mechanisms. *Am J Physiol Regul Comp Physiol*, **284**, R936-R944.

Magnusson, I., Rothman, D. L., Katz, L. D., Shulman, R. G., Shulman, G. I. (1992) Increased rate of gluconeogenesis in type II diabetes mellitus – A 13C nuclear magnetic resonance study. *J Clin Invest*, **90**, 1323-1327.

Massa, L., Baltrusch, S., Okar, D. A, Lange, A. J., Lenzen, S., Tiedge, M. (2004) Interaction of 6-phoshpofructo-2-kinase/fructose-2,6-bisphosphatase (PFK-2/FBPase-2) with glucokinase activates glucose phosphorylation and glucose metabolism in insulin producing cells. *Diabetes*, **53**, 1020-1029.

Matschinsky, F. M., Zelent, B.,Doliba, N., Li, C., Vanderkooi, J. M., Naji, A., Sarabu, R., Grimsby, J. (2011) Glucokinase activators for diabetes therapy - May 2010 status report. *Diabetes Care*, **34**, S236-S243.

McConnell, H. M. (1958) Reaction Rates by Nuclear Magnetic Resonance. *J Chem Phys*, **28**, 430-431

Melendez-Hevia, E., Waddell, T. G. and Shelton, E. D. (1993) Optimization of molecular design in the evolution of metabolism: the glycogen molecule. *Biochem J*, **295**, 477-483.

Meléndez, R., Meléndez-Hevia, E. and Cascante, M. (1997) How did glycogen structure evolve to satisfy the requirement for rapid mobilization of glucose? A problem of physical constraints in structure building. *J Mol Evol*, **45**, 446-455.

McBride A., Hardie D. G. (2009) AMP-activated protein kinase--a sensor of glycogen as well as AMP and ATP? *Acta Physiol*, **196**, 99-113.

Meyer, F., Heilmeyer, L. M., Haschke, R. H. and Fischer, E. H. (1970) Control of phosphorylase activity in a muscle glycogen particle. I. Isolation and characterization of the protein–glycogen complex. *J Biol Chem*, **245**, 6642-6648.

Moore, M. C., Cherrington, A. D., Cline, G. W., Pagliassotti, M. J., Jones, E. M., Neal, D. W., Badet, C., Shulman, G.I. (1991) Sources of carbon for hepatic glycogen synthesis in the conscious dog. J Clin Invest, 88, 578-587.

Moore, M. C., Coate, K. C., Winnick, J. J., An, Z., Cherrington, A.D. (2012) Regulation of hepatic glucose uptake and storage in vivo. *Adv Nutr*, **3**, 286-294.

Myers, S. R., McGuinness, O. P., Neal, D. W., Cherrington, A. D. (1991) Intraporal glucose delivery alters the relationship between net hepatic glucose uptake and the insulin concentration. *J Clin Invest*, **87**, 930-99.

Nakao, M., Matsubara, T., Sakamoto, N. (1993) Effects of diabetes on cardiac glycogen metabolism in rats. *Heart and Vessels*, **8**, 171-175.

Nasrallah, F. A., Pages, G., Kuchel, P. W., Golay, X., Chuang, K. H. (2013) Imaging brain deoxyglucose uptake and metabolism by glucoCEST MRI. *J Cerebr Blood Flow Met*, **33**, 1270-1278.

Newgard, C. B., Matschinsky, F.M. (2001) Substrate control of insulin release: the endocrine system. Vol II. *The endocrine pancreas and regulation of metabolism*. In Handbook of Physiology, Jefferson J., Cherrington, A., Eds. Oxford, Oxford University Press, 125–151.

Öz, G., Seaquist E. R., Kumar, A., Criego, A. B., Benedict, L. E., Rao, J. P., Henry, P. G., Van De Moortele, P. F., Gruetter, R. (2007) Human brain glycogen content and metabolism: implications on its role in brain energy metabolism. *Am J Physiol Endocrinol Metab*, **292**, E946-E951.

Pagliassotti, M. J., Holste, L. C., Moore, M. C., Neal, D. W., Cherrington, A. D. (1996) Comparison of the time courses of insulin and the portal signal on hepatic glucose and glycogen metabolism in the conscious dog. *J Clin Invest*, **97**, 81-91.

Polekhina, G., Gupta, A., Michell, B. J., van Denderen, B., Murthy, S., Feil, S. C., Jennings, I. G., Campbell, D. J., Witters, L. A. and Parker, M. W. (2003) AMPKβ subunit targets metabolic stress sensing to glycogen. *Curr Biol*, **13**, 867-871.

Ramnanan, C. J., Edgerton, D. S., Kraft, G., Cherrington, A. D. (2011) Physiologic action of glucagon on liver glucose metabolism. *Diabetes Obes Metab*, **13 S1**, 118-25.

Rivlin, M., Horev, J., Tsarfaty, I., Navon, G. (2013) Molecular imaging of tumors and metastases using chemical exchange saturation transfer (CEST) MRI. *Sci Reports*, **3**, 1-7.

Roach, P. J., Skurat, A. V., Harris, R. A. (2011) Regulation of Glycogen Metabolism. *Handbook of Physiology, The Endocrine System, The Endocrine Pancreas and Regulation of Metabolism*. Chapter 19, 609-647.

Roach, P. J., Depaoli-Roach, A.A., Hurley, T. D., Tagliabracci, V. D. (2012) Glycogen and its metabolism: some new developments and old themes. *Biochem J*, **441**, 763-787.

Roden, M., Shulman, G. I. (1999) Applications of NMR spectroscopy to study muscle glycogen metabolism in man. *Annu Rev Med*, **50**, 277-290.

Rothman, D. L., Magnusson, I., Katz, L. D., Shulman, R. G., Shulman, G. I. (1991) Quantitation of hepatic glycogenolysis and gluconeogenesis in fasting humans with 13C NMR. *Science*, **254**, 573-576.

Rothman, D. L., Magnusson, I., Cline, G., Gerard, D., Kahn, C. R., Shulman, R. G., Shulman, G. I. (1995) Decreased muscle glucose transport/phosphorylation is an early defect in the pathogenesis of non-insulin-dependent diabetes mellitus. *Proc Natl Acad Sci*, **92**, 983–987.

Sakoda, H., Ogihara, T., Anai, M., Fujishiro, M., Ono, H., Onishi, Y., Katagiri, H., Abe, M., Fukushima, Y., Shojima, N., Inukai, K., Kikuchi, M., Oka, Y., Asano, T. (2002) Activation of AMPK is essential for AICAR-induced glucose uptake by skeletal muscle but not adipocytes. *Am J Physiol Endocrinol Metab*, **282**, E1239-44.

Saltiel, A. R., Kahn, R. C. (2001) Insulin signaling and the regulation of glucose and lipid metabolism. *Nature*, **414**, 799-806.

Savage, D. B., Petersen, K. F., Shulman, G. I. (2007) Disordered lipid metabolism and the pathogenesis of insulin resistance. *Physiol Rev*, **87**, 507-520.

Samuel, V. T., Petersen, K. F., Shulman, G. I. (2010) Lipid induced insulin resistance: unraveling the mechanism. *Lancet*, **375**, 2267-2277.

Shulman G. I., Rothman, D. L., Jue, T., Stein, P., DeFronzo, R. A., Shulman, R. G. (1990) Quantitation of Muscle Glycogen Synthesis in Normal Subjects and Subjects with Non-Insulin-Dependent Diabetes by 13C Nuclear Magnetic Resonance Spectroscopy. *N Engl J Med*, **322**, 223-228.

Shulman, R. G., Rothman, D. L. (1991) 13C NMR of intermediary metabolism: implications for systemic physiology. *Annu Rev Physiol*, **63**, 15-48.

Torres, T. P., Catlin, R. L., Chan, R. (2009) Restoration of hepatic glucokinase expression corrects hepatic glucose flux and normalizes plasma glucose in zucker diabetic fatty rats. *Diabetes*, **58**, 78–86.

van Schaftingen, E., Vandercammen, A., Detheux, M., Davies, D. R. (1992) The regulatory protein of liver glucokinase. *Adv Enzyme Regul*, **32**, 133-48.

Van Zijl, P. C. M., Jones, C. K., Ren, J., Malloy, C. R., Sherry, A. D. (2007) MRI detection of glycogen in vivo using chemical exchange saturation transfer imaging (glycoCEST). *Proc Natl Acad Sci*, **104**, 4359-4364.

Villar-Palasí, C., Guinovart, J. J. (1997) The role of glucose 6-phosphate in the control of glycogen synthase. *FASEB J*, **11**, 544-58.

Vincent, M. F., Marangos, P. J., Gruber, H. E., Van den Berghe, G. (1991) Inhibition by AICA-riboside of gluconeogenesis in isolated rat hepatocytes. *Diabetes*, **40**, 1259-1266.

Viollet, B., Foretz, M., Guigas, B., Horman, S., Dentin, R., Bertrand, L., Hue, L., Andreelli F. (2006) Activation of AMP-activated protein kinase in the liver: a new strategy for the management of metabolic hepatic disorders. *J Physiol*, **574**, 41–53.

Winder, W.W., Hardie, G. D. (1999) AMPK-activated protein kinase, a metabolic master switch: possible roles in Type 2 diabetes. *Am J Physiol Endocrinol Metab* **40**, E1-10.

Winnick, J. J., An, Z., Ramnanan, C. J., Smith, M., Irimia J. M., Neal, D. W., Moore, M. C., Roach, P. J., Cherrington, A. D. (2011) Hepatic glycogen supercompensation activates AMP-activated protein kinase, impairs insulin signaling, and reduces glycogen deposition in the liver. *Diabetes*, **60**, 398-407.

Winnick, J. J., Kraft, G., Farmer, B., Lautz, M., Allen, E., Cherrington, A. D. (2012) Liver Glycogen Loading Amplifies Counterregulatory Hormone Release and the Hepatic Response to Hypoglycemia. ADA Scientific Sessions, 1765-P.

Winnick, J. J., An, Z., Kraft, G., Ramnanan, C. J., Irimia J. M., Smith, M., Lautz, M., Roach, P. J., Cherrington A. D. (2013) Liver Glycogen Loading Dampens Glycogen Synthesis Seen in Response to Either Hyperinsulinemia or Intraportal Glucose Infusion. *Diabetes*, **62**, 96–101.

Zaiss, M., Schmitt, B., Bachert, P. (2011) Quantitative separation of CEST effect from magnetization transfer spillover effects by Lorentzian-line-fit analysis of z-spectra. *J Mag Res*, **211**, 149-155.

Zhou, G., Myers, R., Li, Y., Chen, Y., Shen, X., Fenyk-Melody, J., Wu, M., Ventre, J., Doebber, T., Fujii, N., Musi, N., Hirshman, M. F., Goodyear, L. J., Moller, D. E. (2001) Role of AMPK in the mechanism of Metformin action. *J Clin Invest*, **108**, 1167-74.

Zhou, J., Wilson, D. A., Sun, P. Z., Klaus, J. A., Van Zijl, P. C. M. (2004) Quantitative description of proton exchange processes between water and endogenous and exogenous agents for WEX, CEST, and APT experiments. *Mag Res Med*, **51**, 945-52.

Zhou, J., van Zijl, P. C. M., (2006) Chemical exchange saturation transfer imaging and spectroscopy. *Prog Nuc Mag Res Spect*, **48**, 109-136.

Zhou J. (2011) Amide proton transfer imaging of the human brain. *Methods Mol Biol*, **711**, 227-37.

APPENDIX

A. Matlab Processing Code

```
function l = CESTShiftLorentzian
% l = CESTShiftLorentzian
% CESTshiftLorentzian.m generates a string describing an upside down
% Lorentzian lineshape for use in fitting CEST Z-Spectra, including a
% shift term to correct for the centering of the spectra

    h='x(1)';
    w='x(2)';
    dc='x(3)';
    xo='x(4)';

    l=strcat(dc,'-(',h,'./(4.*((xdata-',xo,')./',w,').^2 + 1))');
```

```
function ppmList = WriteFreqList(BF,Zero,Flag,ppm1,ppm2,ppminc)
%
% ppmList = WriteFreqList(BF,Zero,ppm1,ppm2,ppminc)
%
% WriteFreqList.m writes a series of files containing frequency offsets
% to be used by the Bruker AU program 'noemult' entitled CEST.1,
% CEST.2, ..., CEST.n.  Freqency offsets are in +/- pairs (e.g. 5,-5,4,-
4,...)
% These files are written to the C:\FreqLists\ directory which can then
% be exported to XWin-NMR.  Input parameters are as follows:
%
%   BF = Basic Frequency (500.1300000 MHz)
%   Zero = Frequency (MHz) corresponding to the water peak
%   Flag = 1 if using the non-uniform offset list, Flag = 0 if using the
%       uniformly spaced list
%   ppm1 = starting ppm offset
%   ppm2 = ending ppm offset
%   ppminc = increment between ppm1 and ppm2

if Flag==1;
    % Make the non-uniformly spaced offset vector.
    temp=[5 4 3.6 3.2 2.8 2.4 2 1.8 1.6 1.4 1.2 1 0.8 0.6 0.3];
    temp=[interleave(temp',-temp')' 0];
elseif Flag==2;
    % Make the non-uniformly spaced 64 offset vector for future fitting.
    temp=[9 8.75 8.5 8.25 8 7 6 5 4.5 4 3.5 3.25 3 2.8 2.6 2.4 2.2 2 1.8 ...
          1.6 1.4 1.2 1 0.8 .7 .6 .5 .4 .3 .2 .1];
    temp=[interleave(temp',-temp')' 0];
elseif Flag==3;
    % Make the non-uniformly spaced 32 offset vector for future fitting.
    temp=[9 8.5 8 6 4 2.5 2 1.75 1.5 1.25 1 0.75 0.5 0.25 0.1];
    temp=[interleave(temp',-temp')' 0];
elseif Flag==4;
    % Make the non-uniformly spaced 36 offset vector for 7T data.
    temp=[20 10 5 2.5 2 1.75 1.5 1.25 1 0.75 0.5 0.4 0.3 0.2 0.15 0.1 0.05];
    temp=[interleave(temp',-temp')' 0];
elseif Flag==5;
    % Make the non-uniformly spaced 36 offset vector for 7T data.
    temp=[12 6 3 2 1.75 1.5 1.25 1 0.75 0.5 0.4 0.3 0.25 0.2 0.15 0.1 0.05];
    temp=[interleave(temp',-temp')' 0];
else
    % Make the uniformly spaced offset vector.
    a=[ppm1:-1*ppminc:ppm2];
    temp=zeros(size(a));

    % Arrange into +/- pairs.
    for i=1:length(a)/2;
        temp(2*i-1)=a(i);
        temp(2*i)=a(length(a)-i+1);
    end
end
```

```
% Add on the reference offset.
ppmList=[temp 40]';
b=1e6*(Zero-BF);

% Convert ppm offsets into absolute frequencies.
FreqList=b+ppmList*BF;

% Write each offset into a sepate file.
for i=1:length(FreqList);
    filename=strcat('c:\Freqlists\CEST.',num2str(i));
    fid=fopen(filename,'w');
    fprintf(fid,'O ');
    fprintf(fid,'%2.6f\n',BF);
    fprintf(fid,'%2.2f',FreqList(i));
    fclose(fid);
end
```

```
function
[FitZSpec,FitMTRasym,MTRasym,FitAUC,AUC,FitCESTdiff,CESTdiff]=MakeZSpec(expid
,expno,ppmList,si,sw,intLim,ppmTarget,FitFlag)

% [ZSpec,FitMTRasym,MTRasym,FitAUC,AUC,FitCESTdiff,CESTdiff]=
%            MakeZSpec(expid,expno,ppmList,si,sw,intLim,ppmTarget,FitFlag)
%
% MakeZSpec.m makes a Z-Spectrum from a '2rr' Bruker data file, i.e. a
% file generated by packing the separate spectra in the Z-Spectrum into a
% 2D data set.  This function also calculates the MTRasym two ways, (1)
% directly from the Z-Spectrum (i.e. MTR = (S(-w)-S(w))/So, and (2) by
% fitting the Z-Spectrum to an upside down Lorentzian and subtracting the
% Z-Spectrum from the modeled Z-Spectrum.  Input parameters are as follows:
%
% expid - directory path and root file name
% expno - experiment # from that series
% ppmList - vector of ppm offset values used to make the Z-Spectrum
% si - # of data points per individual spectrum (8192)
% sw - Sweep width (Hz) of each spectrum (20)
% intLim - region (+/-) to integrate the water peak over in each spectrum
% ppmTarget - region of the MTRasym curve to integrate over for the final
%   CEST measurement ([2.5 0.5])
% FitFlag = 1 to also perform the Lorentzian fit, FitFlag = 0 to not.
%
% Filenames are expected to be of the form <expid>.<expno> (e.g.
% CESTStudy1.001, CESTStudy1.002, etc. for all the Z-Spectra

% Manipulate the file path if necessary to parse out the filename.
% Assumed to be of the form $PATH\expid.expno (e.g. C:\Data\Liver.001)
filepath='';
a=find(expid=='\');
if isempty(a)==0;
   filepath=expid(1:max(a));
   expid=expid(max(a)+1:length(expid));
end

if expno<10;
    expnostr=strcat('00',num2str(expno));
elseif expno>=10 & expno<100;
    expnostr=strcat('0',num2str(expno));
else
    expnostr=num2str(expno);
end

% Open the file and read the data. Note that the data comes out as one long
% series of numbers (not a 2D array as Bruker would imply) which needs to be
% chopped into the individual spectra in the next section.
a=fopen(strcat(filepath,expid,'.',expnostr),'r','ieee-le');
spectra=fread(a,Inf,'int32');
fclose(a);

% Parse out the individual spectra into a matrix called 'specmat'. It is
```

```
% expected here that the ppm offsets are symmetric about 0 and that the
% spectra have been acquired in an alternating fashion
% (e.g. +9,-9,+8.5,-8.5,0.1,-0.1,...,0,RefFreq).  Examples noted in the
% comments below will be for 32 ppm offsets.

Nspecs=length(spectra)/si;  % Total # of spectra = 32
for i=1:Nspecs/2;           % i=1:16
                                                    % i=1, 1:si
    specmat(i,:)=spectra(2*(i-1)*si+1:(2*i-1)*si);  % i=2, 2*si+1:3*si
                                                    % i=16, 30*si+1:31*si

                            % So temp(1:16) equals the positive offset
    temp(i)=ppmList(2*i-1); % entries 1,3,5,...,31 in ppmList (#31 being 0)
end

for i=1:Nspecs/2-1;         % i=1:15
                                                      % i=1, si+1:2*si
    specmat(Nspecs-i,:)=spectra((2*i-1)*si+1:2*i*si); % i=2, 3*si+1:4*si
                                                      % i=15, 29*si+1:30*si

                                % So temp(31:-1:17) equals the negative
    temp(Nspecs-i)=ppmList(2*i); % entries 2,4,6,...,30 in ppmList.
end
specmat(Nspecs,:)=spectra((Nspecs-1)*si+1:Nspecs*si); % i=32, 31*si+1:32*si
temp(Nspecs)=ppmList(Nspecs); % So temp(32)=ppmList(32), the reference spec

ppmList=temp'; % ppmList is now ordered correctly, e.g. 9,8.5,...0,...,-
8.5,9,Ref

% Make the Z-Spectrum based on AUC from each spectrum.

                        % In case you only want to use part of the spectrum
if exist('intLim')==1;  % to calculate the AUC, like when there's a large
                        % lipid signal.  intLim has units of ppm.

    limit1=round(si/2-intLim*si/sw); % Round the ppm limits to the nearest
    limit2=round(si/2+intLim*si/sw); % data point

    ZSpec=trapz(specmat(:,limit1:limit2),2); % Calculate the AUC
else
    ZSpec=trapz(specmat,2); % Calculate the AUC (no integration limits)
end

ZSpec=100*ZSpec/ZSpec(length(ZSpec)); % Normalize the Z-Spectrum to the
                                      % reference spectrum


% Make the MTRasym based on the Z-Spectrum.
ppms=ppmList(1:length(ppmList)/2); % Picks out the first half (16) of the
values
MTRasym=zeros(length(ZSpec)/2,1); % (32)
ZSpec=ZSpec(1:length(ZSpec)-1); % Removes the value from reference spectrum
(31)
for i=1:(length(ZSpec)-1)/2; % i=1:15
```

```
                                                        % The MTRasym
calculation
                                                        % i=1:ZSpec(31)-
ZSpec(1)
    MTRasym(i)=ZSpec(length(ZSpec)-i+1)-ZSpec(i);       % i=2:ZSpec(30)-
ZSpec(2)
                                                        %          |
                                                        % i=15:ZSpec(17)-
ZSpec(15)
end                                                     % Note still 0 at end.

AUC=trapz(MTRasym)
AUC=-trapz(ppms,MTRasym); % Total MTRasym AUC.  Note the negative since the
                          % ppm values decrease

% Plot the spectral series
for i=1:Nspecs;
   figure(10);
   plot([(i-1)*si+1:i*si],specmat(i,:))
   hold on
end

% Plot the Z-Spectrum and MTRasym
ppmList=ppmList(1:length(ppmList)-1); % (31)
figure(1)
plot(ppmList,ZSpec,'k')
hold on
plot(ppmList(1:length(MTRasym)),MTRasym,'k')
set(gca,'XDir','Reverse')

% Now calculate a more 'local' MTRasym value, either the value at the
% expected offest, or in the region around the expected offest.

                            % ppmTarget is either the value of the expected
if prod(size(ppmTarget))>1; % max CEST effect or a range [min max] around
                            % that expected value.

    adiff=find(ppmList-ppmTarget(1)==min(abs(ppmList-ppmTarget(1))));
    bdiff=find(ppmList-ppmTarget(2)==min(abs(ppmList-ppmTarget(2))));
    CESTdiff=-trapz(ppms(adiff:bdiff),MTRasym(adiff:bdiff))
else
    adiff=find(ppmList-ppmTarget==min(abs(ppmList-ppmTarget)));
    CESTdiff=MTRasym(adiff);
end

% If required, calculate the MTRasym by fitting to a Lorentzian, which is
% described by its height, width, offset from 0, and asymptotic value

if FitFlag==1; % Determines if a fit is to be done

    % Defines the region over which to use the data to fit. This is
    % generally far from 0 and close to 0.
    FitRegion=[find(ppmList>=8)' find(ppmList<0.4 & ppmList>-2)'
find(ppmList<=-8)'];
```

```
    % Calculate the initial parameters to use for the fit
    dc0=ZSpec(1);
    Zero=find(ppmList==0);
    Height0=dc0-ZSpec(Zero);
    a=find(ZSpec<Height0/2);
    a=a(1);
    Width0=2*abs(ppmList(a));

    % Define the data needed for the lsqcurvefit function
    xdata=ppmList(FitRegion);
    ydata=ZSpec(FitRegion);

                            % Calls the script to generate the string
    l=CESTShiftLorentzian;  % describing the upside-down Lorentzian which
                            % is used for the fit.

    fiteqn=inline(l,'x','xdata');
    p0=[Height0 Width0 dc0 0]; % The initial parameters.
    opts=optimset('MaxIter',100,'MaxFunEvals',2000); % Parameters used by
                                                     % the fitting routine

    % Performs the curve fit

[param,ressum,residual,exitflag,output]=lsqcurvefit(fiteqn,p0,xdata,ydata,[],
[],opts);

    % Extract the values of the parameters from the curve fit
    param
    Height=param(1);
    Width=param(2);
    dc=param(3);
    xo=param(4);

    % Plot the fit Z-Spectrum along with the data points used to fit
    FitZSpec=dc-(Height./(4*((ppmList-xo)/Width).^2+1));
    plot(ppmList,FitZSpec,'r')
    plot(xdata,ydata,'r*')

    % Calculate the MTRasym from the modeled Z-Spectrum
    FitMTRasym=FitZSpec-ZSpec;
    FitMTRasym=FitMTRasym(1:length(MTRasym));
    plot(ppmList(1:length(MTRasym)),FitMTRasym,'r')
    FitAUC=-trapz(ppms,FitMTRasym)
    FitCESTdiff=-trapz(ppms(adiff:bdiff),FitMTRasym(adiff:bdiff))
    set(gca,'XDir','Reverse')

end
```

```
function
C13Stdev=Make13CError(expid,expno,Areas,Heights,P2PNoise,n,GlycogenCalibratio
n)
%
%   C13AreaDist=Make13CError(Areas,Heights,P2PNoise,n)
%   Make13CError uses a Monte Carlo approach to generate an estimate of the
%   error from fitting a series of peaks in a 13C NMR spectrum.  This
%   assumes that the spectrum has already been fit and the model peak areas
%   and heights are known.  These are either read into the function directly
%   or loaded from existing files. Input parameters are as follows:
%
%   Areas = list of peak areas for a given spectrum (use [] if already
%       saved in a local file
%   Heights = list of peak heights for a given spectrum (use [] if already
%       saved in a local file
%   LW = list of linewidths corresnpoding to each area
%   P2PNoise = The peak to peak noise from the spectrum of intrest
%   n = number of simulations to use (>10000 suggested)

% Check if Areas and Heights are defined and load the files if not.
if isempty(Areas)==1;
    load(strcat(expid,'Areas0',num2str(expno),'.mat'))
    load(strcat(expid,'Heights0',num2str(expno),'.mat'))
end

RMSNoise=P2PNoise/(2*sqrt(2)); % Calculate RMS noise from peak to peak noise
C13AreaDist=zeros(n,length(Areas));
for i=1:length(Areas);                                      % The normalized
    NormError=(Heights(i)+RMSNoise*randn(n,1))/Heights(i);  % error for each
peak
    C13AreaDist(:,i)=Areas(i)*NormError; % The distribution of areas for each
peak
end
C13AreaDist=sum(C13AreaDist,2)*GlycogenCalibration; % The distribution of
total glycogen values
C13Stdev=std(C13AreaDist)
mean(C13AreaDist) % Display the mean just to check that it is the same as the
                  % original area value

% Save the Areas and Heights so that they don't need to be looked up again
save(strcat(expid,'Areas0',num2str(expno),'.mat'),'Areas')
save(strcat(expid,'Heights0',num2str(expno),'.mat'),'Heights')

% Save the distribution for future use
save(strcat(expid,'13CDist0',num2str(expno),'.mat'),'C13AreaDist')

% Plot the distribution
figure(1)
edges=(min(C13AreaDist):(max(C13AreaDist)-
min(C13AreaDist))/50:max(C13AreaDist));
bar(edges,histc(C13AreaDist,edges));
```

```
function
[Average,Stdev]=ZSpecError(expid,expno,ppmList,si,sw,intLim,ppmTarget,P2PNois
e,n)
%
[Average,Stdev]=ZSpecError(expid,expno,ppmList,si,sw,intLim,ppmTarget,P2PNois
e,n)
%
% ZSpecError.m uses a Monte Carlo approach to generate an error estimate
% of the MTRasym derived from a given Z-Spectrum.  The beginning part
% of the program reads in the file and parses out the individual spectra
% much like MakeZSpec.m.  Then once the Z-Spectrum is calculated, some
% random error defined by the peak to peak noise is added to each point in
% the spectrum and the resulting Z-Spectrum is analyzed to calculate the
% new MTRasym curve.  This is repeated n times to form a distribution of
% MTRasym curves.  Input parameters are as follows:
%
% expid - directory path and root file name
% expno - experiment # from that series
% ppmList - vector of ppm offset values used to make the Z-Spectrum
% si - # of data points per individual spectrum (8192)
% sw - Sweep width (Hz) of each spectrum (20)
% intLim - region (+/-) to integrate the water peak over in each spectrum (2)
% ppmTarget - region of the MTRasym curve to integrate over for the final
%   CEST measurement ([2.5 0.5])
% P2PNoise = Peak to peak noise from the spectra making up the Z-Spectrum
(2e3)
% n - number of times to run the simulation (5000 - 50000)

% Manipulate the file path if necessary to parse out the filename.
% Assumed to be of the form $PATH\<expid>.<expno> (e.g. C:\Data\Liver.001)
filepath='';
a=find(expid=='\');
if isempty(a)==0;
   filepath=expid(1:max(a));
   expid=expid(max(a)+1:length(expid));
end

if expno<10;
    expnostr=strcat('00',num2str(expno));
elseif expno>=10 & expno<100;
    expnostr=strcat('0',num2str(expno));
else
    expnostr=num2str(expno);
end

% Open the file and read the data. Note that the data comes out as one long
% series of numbers which needs to be chopped into the individual spectra
% in the next section.
a=fopen(strcat(filepath,expid,'.',expnostr),'r','ieee-le');
spectra=fread(a,Inf,'int32');
fclose(a);

% Parse out the individual spectra. It is expected here that the ppm
```

```
% offsets are symmetric about 0 and that the spectra have been acquired in
% an alternating fashion (e.g. +9,-9,+8.5,-8.5,...,0,RefFreq).  Examples
% noted in the comments below will be for 32 ppm offsets.

Nspecs=length(spectra)/si;  % Total # of spectra = 32
for i=1:Nspecs/2;           % i=1:16
                                                    % i=1, 1:si
    specmat(i,:)=spectra(2*(i-1)*si+1:(2*i-1)*si);  % i=2, 2*si+1:3*si
                                                    % i=16, 30*si+1:31*si

                            % So temp(1:16) equals the positive offset
    temp(i)=ppmList(2*i-1); % entries 1,3,5,...,31 in ppmList (#31 being 0)
end

for i=1:Nspecs/2-1;         % i=1:15
                                                      % i=1, si+1:2*si
    specmat(Nspecs-i,:)=spectra((2*i-1)*si+1:2*i*si); % i=2, 3*si+1:4*si
                                                      % i=15, 29*si+1:30*si

                                % So temp(31:-1:17) equals the negative
    temp(Nspecs-i)=ppmList(2*i); % entries 2,4,6,...,30 in ppmList.
end
specmat(Nspecs,:)=spectra((Nspecs-1)*si+1:Nspecs*si); % i=32, 31*si+1:32*si
temp(Nspecs)=ppmList(Nspecs); % So temp(32)=ppmList(32), the reference spec

ppmList=temp'; % ppmList is now ordered correctly, e.g. 9,8.5,...0,...,-8.5,-
9,Ref

% Make the Z-Spectrum based on AUC from each spectrum.

                        % In case you only want to use part of the spectrum
if exist('intLim')==1;  % to calculate the AUC, like when there's a large
                        % lipid signal.  intLim has units of ppm.

    limit1=round(si/2-intLim*si/sw); % Round the ppm limits to the nearest
    limit2=round(si/2+intLim*si/sw); % data point

    ZSpecOriginal=trapz(specmat(:,limit1:limit2),2); % Calculate the AUC for
each spectrum
    PeakHeights=max(specmat,[],2); % Finds the peak heights for error
analysis later
else
    ZSpecOriginal=trapz(specmat,2); % Calculate the AUC (no integration
limits)
    PeakHeights=max(specmat,[],2);
end

ZSpec0=100*ZSpecOriginal/ZSpecOriginal(length(ZSpecOriginal)); % Normalize
the Z-Spectrum to the
                                                               % reference
spectrum

% Make the original MTRasym based on the Z-Spectrum.
ppms=ppmList(1:length(ppmList)/2); % Picks out the first half (16) of the
values
```

```
MTRasym0=zeros(length(ZSpec0)/2,1); % Allocates 16 values
ZSpec0=ZSpec0(1:length(ZSpec0)-1); % Removes the value from reference
spectrum
for i=1:(length(ZSpec0)-1)/2; % i=1:15
                                                        % The MTRasym
calculation
                                                        % i=1:ZSpec(31)-
ZSpec(1)
    MTRasym0(i)=ZSpec0(length(ZSpec0)-i+1)-ZSpec0(i); % i=2:ZSpec(30)-
ZSpec(2)
                                                        %          |
                                                        % i=15:ZSpec(17)-
ZSpec(15)
end                                                     % Note still 0 at end.

% Plot the Z-Spectrum and MTRasym
ppmList=ppmList(1:length(ppmList)-1); % Removes the reference offset value
figure(1)
plot(ppmList,ZSpec0,'k')
hold on
plot(ppmList(1:length(MTRasym0)),MTRasym0,'k')
set(gca,'XDir','Reverse')

% Up until now this has all been the same as in MakeZSpec.m.  Now we will
% incorporate some error into each value in the Z-Spectrum.  This is done
% by adding a random # based on the spectral noise to each value in the
% Z-Spectrum.  This will be done n times.

% First define the region of the MTRasym curve over which to calculate the
% AUC before the loop for efficiency.

                            % ppmTarget is either the value of the expected
if prod(size(ppmTarget))>1; % max CEST effect or a range [max min] around
                            % that expected value.

    adiff=find(ppmList-ppmTarget(1)==min(abs(ppmList-ppmTarget(1))));
    bdiff=find(ppmList-ppmTarget(2)==min(abs(ppmList-ppmTarget(2))));
else
    adiff=find(ppmList-ppmTarget==min(abs(ppmList-ppmTarget)));
end

% Here's the main loop for the Monte Carlo error simulations
tstart=tic;
RMSNoise=P2PNoise/(2*sqrt(2));
for i=1:n;
                                                                % Add random
error
    PeakError=PeakHeights+RMSNoise*randn(length(PeakHeights),1); % to the
peak
                                                                % heights
based on
                                                                % the P2P
noise
    NormError=PeakError./PeakHeights; % Normalized error of each peak
    ZSpecNew=ZSpecOriginal.*NormError; % This is the Z-Spectrum + error at
each point
```

```
    ZSpecNew=100*ZSpecNew/ZSpecNew(length(ZSpecNew)); % Normalize the Z-
Spectrum to the
                                            % reference spectrum

    ZSpecNew=ZSpecNew(1:length(ZSpecNew)-1); % Removes the value from
reference spectrum

    % Defines the region over which to use the data to fit. This is
    % generally far from 0 and close to 0.
    FitRegion=[find(ppmList==8)' find(ppmList<0.4 & ppmList>-2)'
find(ppmList==-8)'];

    % Calculate the MTRasym by fitting to a Lorentzian, which is described
    % by its height, width, offset from 0, and asymptotic value.

    dc0=ZSpecNew(1);                %
    Zero=find(ppmList==0);          % Calculates the
    Height0=dc0-ZSpecNew(Zero);     % initial parameters
    a=find(ZSpecNew<Height0/2);     % to be used
    a=a(1);                         % in the fit
    Width0=2*abs(ppmList(a));       %

    % Define the data needed for the lsqcurvefit function
    xdata=ppmList(FitRegion);
    ydata=ZSpecNew(FitRegion);
    l=CESTShiftLorentzian; % the upside-down Lorentzian which is used for the
fit

    fiteqn=inline(l,'x','xdata');
    p0=[Height0 Width0 dc0 0]; % The initial parameters.
    opts=optimset('MaxIter',100,'MaxFunEvals',2000,'Display','off'); %
Parameters used by
                                                                    % the
fitting routine
    % Performs the curve fit

[param,ressum,residual,exitflag,output]=lsqcurvefit(fiteqn,p0,xdata,ydata,[],
[],opts);

    % Extract the values of the parameters from the curve fit
    Height=param(1);
    Width=param(2);
    dc=param(3);
    xo=param(4);

    % Plot the fit Z-Spectrum along with the data points used to fit
    FitZSpec=dc-(Height./(4*((ppmList-xo)/Width).^2+1)); % The Lorentzian
equation
    plot(ppmList,FitZSpec,'r')
    plot(xdata,ydata,'r*')

    % Calculate the MTRasym from the modeled Z-Spectrum
    FitMTRasym=FitZSpec-ZSpecNew;
    FitMTRasym=FitMTRasym(1:length(ZSpecOriginal)/2);
```

```
    % Plot the many MTRasym curves
    plot(ppmList(1:length(FitMTRasym)),FitMTRasym,'r')
    set(gca,'XDir','Reverse')

    % Calculate the AUC under the defined region
    FitMTRAUC(i)=-trapz(ppms(adiff:bdiff),FitMTRasym(adiff:bdiff));
end
toc(tstart)

% Calculate the statistics for the distribution of MTRasym AUC values
Average=mean(FitMTRAUC)
Stdev=std(FitMTRAUC)
strcat(filepath,expid,'Dist00',num2str(expno),'.mat')
save(strcat(filepath,expid,'Dist00',num2str(expno),'.mat'),'FitMTRAUC')

% Plot the distribution
figure(2)
edges=(min(FitMTRAUC):(max(FitMTRAUC)-min(FitMTRAUC))/50:max(FitMTRAUC));
bar(edges,histc(FitMTRAUC,edges));
```

```
function Stdev=CESTvsC13Correlation(n)

% This function generates the distribution of the parameters descrining the
% correlation between CEST and 13C data.

a1=load('c:\FreqLists\KWCESTLiver7Dist001.mat');
a2=load('c:\FreqLists\KWCESTLiver7Dist002.mat');
a3=load('c:\FreqLists\KWCESTLiver8Dist001.mat');
a4=load('c:\FreqLists\KWCESTLiver10Dist001.mat');
a5=load('c:\FreqLists\KWCESTLiver13Dist001.mat');
a6=load('c:\FreqLists\KWCESTLiver14Dist001.mat');
a7=load('c:\FreqLists\KWCESTLiver15Dist001.mat');
a8=load('c:\FreqLists\KWCESTLiver16Dist001.mat');
a9=load('c:\FreqLists\KWCESTLiver18Dist001.mat');
a10=load('c:\FreqLists\KWCESTLiver18Dist002.mat');
a11=load('c:\FreqLists\KWCESTLiver20Dist001.mat');
a12=load('c:\FreqLists\KWCESTLiver23Dist001.mat');
a13=load('c:\FreqLists\KWCESTLiver23Dist002.mat');

b1=load('c:\FreqLists\KWCESTLiver713CDist023.mat');
b2=load('c:\FreqLists\KWCESTLiver713CDist034.mat');
b3=load('c:\FreqLists\KWCESTLiver813CDist023.mat');
b4=load('c:\FreqLists\KWCESTLiver1013CDist023.mat');
b5=load('c:\FreqLists\KWCESTLiver1313CDist023.mat');
b6=load('c:\FreqLists\KWCESTLiver1413CDist023.mat');
b7=load('c:\FreqLists\KWCESTLiver1513CDist023.mat');
b8=load('c:\FreqLists\KWCESTLiver1613CDist023.mat');
b9=load('c:\FreqLists\KWCESTLiver1813CDist023.mat');
b10=load('c:\FreqLists\KWCESTLiver1813CDist034.mat');
b11=load('c:\FreqLists\KWCESTLiver2013CDist023.mat');
b12=load('c:\FreqLists\KWCESTLiver2313CDist023.mat');
b13=load('c:\FreqLists\KWCESTLiver2313CDist034.mat');

for i=1:n;
    for j=1:13;

%['y(',num2str(j),')=',strcat('a',num2str(j),'.FitMTRAUC(',num2str(i),');')]

%['x(',num2str(j),')=',strcat('b',num2str(j),'.C13AreaDist(',num2str(i),');')
]

eval(['y(',num2str(j),')=',strcat('a',num2str(j),'.FitMTRAUC(',num2str(i),');
')]);

eval(['x(',num2str(j),')=',strcat('b',num2str(j),'.C13AreaDist(',num2str(i),'
);')]);
    end
    figure(1)
    plot(x,y,'*')
    hold on
    p=polyfit(x,y,1);
    slope(i)=p(1);
    intercept(i)=p(2);
```

```
    yfit=polyval(p,x);
    yresid=y-yfit;
    SSresid=sum(yresid.^2);
    SStotal=(length(y)-1)*var(y);
    rsq(i)=1-SSresid/SStotal;
end
xlabel('13C NMR Glycogen (umoles)')
ylabel('MTRasym AUC 0.5 --> 2.5 ppm')

mean(rsq)
Stdev=std(rsq)
figure(2)
edges=(min(rsq):(max(rsq)-min(rsq))/50:max(rsq));
bar(edges,histc(rsq,edges));
xlabel('R-Squared')

mean(slope)
Stdev=std(slope)
figure(3)
edges=(min(slope):(max(slope)-min(slope))/50:max(slope));
bar(edges,histc(slope,edges));
xlabel('Slope')

mean(intercept)
Stdev=std(intercept)
figure(4)
edges=(min(intercept):(max(intercept)-min(intercept))/50:max(intercept));
bar(edges,histc(intercept,edges));
xlabel('Y-Intercept')
```

```
function Z = LoadZImage(m,n,nfiles)
%
% Z = LoadZImage(m,n,nfiles)
%
% LoadZImage loads DICOM images (m by n pixels in each, nfiles = # of images)
% in the current directory and forms a 3D matrix where each 'slice'
% is a different saturation frequency offset.

Z=zeros(m,n,nfiles);
for i=1:nfiles;
    if i<10;
        file=strcat('MRIm0',num2str(i),'.dcm');
        Z(:,:,i)=dicomread(file);
    else
        file=strcat('MRIm',num2str(i),'.dcm');
        Z(:,:,i)=dicomread(file);
    end
end

Z=double(Z);
```

```
function
[MTRasym,MTRasymCorr,AUC,AUCCorr,CESTdiff,CESTdiffCorr]=MakeCorrectedMTRasym(
ppmList,ZSpec,ppmTarget,Center)

% [MTRasym,MTRasymCorr,AUC,AUCCorr,CESTdiff,CESTdiffCorr]=
%
MakeCorrectedMTRasym(ppmList,ZSpec,ppmTarget,Center)
%
% MakeCorrectedMTRasym.m calculates the MTRasym function from a Z-spectrum in
two
% ways, (1) directly from the Z-Spectrum (i.e. MTR = (S(-w)-S(w))/So,
% and (2) by correcting for any offset from 0 ppm.  This is done by
% fitting the middle region of the Z-Spectrum to an upside down Lorentzian
and
% using that fit to find the 'true' zero.  The ppm axis is then shifted and
% the Z-Spectrum values are corrected by linear interpolation
% Input parameters are as follows:

% ppmList - vector of ppm offset values used to make the Z-Spectrum
% ZSpec - the Z-spectrum values corresponding to each value in ppmList
% ppmTarget - region of the MTRasym curve to integrate over for the final
%   CEST measurement (e.g. [6 0] [2.5 0.5])
% Center - the loaction of the middle of the Z-Spectrum (generally this is
%   found by the Lorentzian fit but may in some cases be known


% Re-order the ppmList and ZSpec values as it is expected here that the
% ppm offsets are symmetric about 0 and that the spectra have been
% acquired in an alternating fashion (e.g. +12,-12,+6,-6,...,0.1,-
0.1,0,RefFreq).
% Examples noted in the comments below will be for 32 ppm offsets.

Nspecs=length(ZSpec);  % Total # of spectra = 32
for i=1:Nspecs/2;      % i=1:16

    Ztemp(i)=ZSpec(2*i-1); % So temp(1:16) equals the positive offset
    temp(i)=ppmList(2*i-1); % entries 1,3,5,...,31 in ppmList (#31 being 0)
end

for i=1:Nspecs/2-1;     % i=1:15

    Ztemp(Nspecs-i)=ZSpec(2*i); % So temp(31:-1:17) equals the negative
    temp(Nspecs-i)=ppmList(2*i); % entries 2,4,6,...,30 in ppmList.
end

Ztemp(Nspecs)=ZSpec(Nspecs);
temp(Nspecs)=ppmList(Nspecs); % So temp(32)=ppmList(32), the reference spec

ZSpec=Ztemp';  % The Z-Spectrum and
ppmList=temp'; % ppmList are now ordered correctly, e.g. 12,6,...0,...,-6,-
12,Ref
```

```
ZSpec=100*ZSpec/ZSpec(length(ZSpec)); % Normalize the Z-Spectrum to the
                                      % reference spectrum

% Make the MTRasym based on the Z-Spectrum.
ppms=ppmList(1:length(ppmList)/2); % Picks out the first half (16) of the
values
MTRasym=zeros(length(ZSpec)/2,1);  % (16)
ZSpec=ZSpec(1:length(ZSpec)-1);    % Removes the value from reference
spectrum (31)
for i=1:(length(ZSpec)-1)/2;       % i=1:15
                                                        % The MTRasym
calculation
                                                        % i=1:ZSpec(31)-
ZSpec(1)
    MTRasym(i)=ZSpec(length(ZSpec)-i+1)-ZSpec(i);       % i=2:ZSpec(30)-
ZSpec(2)
                                                        %          |
                                                        % i=15:ZSpec(17)-
ZSpec(15)
end                                                     % Note still 0 at end.

AUC=-trapz(ppms,MTRasym); % Total MTRasym AUC.  Note the negative since the
                          % ppm values decrease


% Double check that there is a MTRasym value for the offset of 2.5 ppm since
% this is likely to be important and was not always acquired in some initial
% studies.  If not, then calculate a new value using linear interpolation.
if isempty(find(ppmList==2.5))==1
    a=find(ppms>2.5);
    a=a(length(a));
    ppms(a);
    NewValue=MTRasym(a)+(ppms(a)-2.5)*((MTRasym(a+1)-MTRasym(a))/(ppms(a)-
ppms(a+1)));
    ppmsNew=[ppms(1:a)' 2.5 ppms(a+1:length(ppms))'];
    MTRasymNew=[MTRasym(1:a)' NewValue MTRasym(a+1:length(MTRasym))'];
else
    ppmsNew=ppms;
    MTRasymNew=MTRasym;
end

% Plot the Z-Spectrum and MTRasym.
ppmList=ppmList(1:length(ppmList)-1); % (31)
figure(1)
plot(ppmList,ZSpec,'k')
hold on
plot(ppmsNew,MTRasymNew,'k')
set(gca,'XDir','Reverse')

% Now calculate a more 'local' MTRasym value, either the value at the
% expected offest, or in the region around the expected offest.

                            % ppmTarget is either the value of the expected
if prod(size(ppmTarget))>1; % max CEST effect or a range [min max] around
```

```
                            % that expected value.

    adiff=find(ppmsNew-ppmTarget(1)==min(abs(ppmsNew-ppmTarget(1))));
    bdiff=find(ppmsNew-ppmTarget(2)==min(abs(ppmsNew-ppmTarget(2))));
    CESTdiff=-trapz(ppmsNew(adiff:bdiff),MTRasymNew(adiff:bdiff));
else
    adiff=find(ppmsNew-ppmTarget==min(abs(ppmsNew-ppmTarget)));
    CESTdiff=MTRasymNew(adiff);
end

% Calculate the 0 ppm shift by fitting to a Lorentzian, which is
% described by its height, width, offset from 0, and asymptotic value

% Defines the region over which to fit.
FitRegion=[find(ppmList<=0.3 & ppmList>=-3)'];

% Calculate the initial parameters to use for the fit
dc0=100;
Zero=find(ppmList==0);
Height0=dc0-ZSpec(Zero);
a=find(ZSpec<Height0/2);
a=a(1);
Width0=2*abs(ppmList(a));

% Define the data needed for the lsqcurvefit function
xdata=ppmList(FitRegion);
ydata=ZSpec(FitRegion);

                        % Calls the script to generate the string
l=CESTShiftLorentzian;  % describing the upside-down Lorentzian which
                        % is used for the fit.

fiteqn=inline(l,'x','xdata');
p0=[Height0 Width0 dc0 0]; % The initial parameters.
opts=optimset('MaxIter',100,'MaxFunEvals',2000); % Parameters used by
                                                 % the fitting routine

% Performs the curve fit
[param,ressum,residual,exitflag,output]=lsqcurvefit(fiteqn,p0,xdata,ydata,[],
[],opts);

% Extract the values of the parameters from the curve fit
Height=param(1);
Width=param(2);
dc=param(3);
xo=param(4); % This is the 0 ppm shift.

% Plot the fit Z-Spectrum along with the data points used to fit
FitZSpec=dc-(Height./(4*((ppmList-xo)/Width).^2+1));
plot(ppmList(FitRegion),FitZSpec(FitRegion),'r')
plot(xdata,ydata,'r*')

if nargin==4;   % In case the center
    xo=Center;  % of the Z-Spectrum is
end             % known or should be specefied.
```

```
% Now correct the Z-spectrum.  This is done by first shifting the original
% ppm voffset values and then using these values to interpolate the
% Z-Spectrum to find the new corrected values.

ppmListCorr=ppmList-xo;
%plot(ppmListCorr,ZSpec,'g*')
%hold on

ZSpecCorr=zeros(length(ZSpec),1);
for i=1:length(ppmList);
    a=find(ppmListCorr>ppmList(i));
    b=find(ppmListCorr<ppmList(i));

    if (isempty(b)==0 & isempty(a)==0);
        a=a(length(a));
        b=b(1);
        deltax=ppmList(i)-ppmListCorr(b);
        ZSpecCorr(i)=ZSpec(b)+((ZSpec(a)-ZSpec(b))*deltax/(ppmListCorr(a)-
ppmListCorr(b)));
    else
        ZSpecCorr(i)=ZSpec(i);
    end
end

% Recalculate the MTRasym.
MTRasymCorr=zeros(length(MTRasym),1);
for i=1:(length(ZSpecCorr)-1)/2; % i=1:15
                                                                    % The
MTRasym calculation
                                                                    %
i=1:ZSpec(31)-ZSpec(1)
    MTRasymCorr(i)=ZSpecCorr(length(ZSpecCorr)-i+1)-ZSpecCorr(i);   %
i=2:ZSpec(30)-ZSpec(2)
                                                                    %
|
                                                                    %
i=15:ZSpec(17)-ZSpec(15)
end                                                                 % Note
still 0 at end.

AUCCorr=-trapz(ppms,MTRasymCorr); % Total MTRasym AUC.  Note the negative
                                  % since the ppm values decrease

% As before, insert a value at 2.5 ppm of necessary.
if isempty(find(ppmList==2.5))==1
    a=find(ppms>2.5);
    a=a(length(a));
    ppms(a);
    NewValue=MTRasymCorr(a)+(ppms(a)-2.5)*((MTRasymCorr(a+1)-
MTRasymCorr(a))/(ppms(a)-ppms(a+1)));
    ppmsNew=[ppms(1:a)' 2.5 ppms(a+1:length(ppms))'];
    MTRasymCorrNew=[MTRasymCorr(1:a)' NewValue
MTRasymCorr(a+1:length(MTRasymCorr))'];
else
```

```
    MTRasymCorrNew=MTRasymCorr;
end

% Now recalculate the more 'local' MTRasym value, as done previously.

                              % ppmTarget is either the value of the expected
if prod(size(ppmTarget))>1; % max CEST effect or a range [min max] around
                              % that expected value.

    CESTdiffCorr=-trapz(ppmsNew(adiff:bdiff),MTRasymCorrNew(adiff:bdiff));
else
    CESTdiffCorr=MTRasymCorrNew(adiff);
end

plot(ppmList,ZSpecCorr,'b')
plot(ppmsNew,MTRasymCorrNew,'b')
```

```
function
[AUC,Bo,MTRasymAvg,x,y]=MakeMTRImage(ppmList,ZImage,ppmTarget,PlotFlag,x,y)

% [AUC,Bo,MTRasymAvg,x,y]=MakeMTRImage(ppmList,ZImage,ppmTarget,PlotFlag,x,y)
%
% MakeMTRImage.m calculates the MTRasym function on a pixel by pixel
% basis from a Z-image.  It applies a lorentzian fit to the region near 0
% and uses the fit to correct the ppm values for any offset from 0 ppm.
% The Z-Spectrum is then corrected by linear interpolation and the
% MTRasym is calculated as MTR = (S(-w)-S(w))/So.  The AUC under the MTRasym
% curve is calculated over the spectral region defined by 'ppmTarget' and the
% final output is a matrix of the AUC values for each pixel.
%
% Input parameters are as follows:
%
% ppmList - vector of ppm offset values used to make the Z-Spectrum
% ZImage - A 3D matrix of all the images corresponding to each value in
ppmList
% ppmTarget - region of the MTRasym curve to integrate over for the final
%   CEST measurement ([2.5 .5])
% PlotFlag = 1 if you want to plot the average Z-Spectrum and MTRasym for
%   the ROI specified by x and y
% x and y - vectors containing the x and y coordinates of the ROI specified
%   using the roipoly command (if already defined for the first image in a
%   time series, then can be reused for subsequent images)
%
% Output parameters as follows:
%
% AUC - matrix of MTRasym AUC values at each pixel
% Bo - matrix of Bo offsets
% MTRasymAvg - average MTRasym for the whole ROI (onle meaningful for a
%   small, uniform ROI.
% x and y - same as above, they are also outputs if they are to be reused
%



% Re-order the ppmList and ZSpec values as it is expected here that the
% ppm offsets are symmetric about 0 and that the spectra have been
% acquired in an alternating fashion (e.g. +9,-9,+8.5,-8.5,0.1,-
0.1,...,0,RefFreq).
% Examples noted in the comments below will be for 32 ppm offsets.

a=size(ZImage);
m=a(1);
n=a(2);
Nspecs=a(3);  % Total # of spectra = 32
Ztemp=zeros(size(ZImage));
for i=1:Nspecs/2;                    % i=1:16
    Ztemp(:,:,i)=ZImage(:,:,2*i-1);  % So Ztemp(:,:,1:16) equals the positive
offsets
    temp(i)=ppmList(2*i-1);          % entries 1,3,5,...,31 in ppmList (#31
being 0)
end
```

```
for i=1:Nspecs/2-1;                          % i=1:15
    Ztemp(:,:,Nspecs-i)=ZImage(:,:,2*i); % So Ztemp(:,:,31:-1:17) equals the
negative
    temp(Nspecs-i)=ppmList(2*i);          % entries 2,4,6,...,30 in ppmList.
end

Ztemp(:,:,Nspecs)=ZImage(:,:,Nspecs);
temp(Nspecs)=ppmList(Nspecs); % So temp(32)=ppmList(32), the reference spec

ZImage=Ztemp;   % ZImage and
ppmList=temp';  % ppmList are now ordered correctly, e.g. 12,6,...0,...,-6,-
12,Ref

figure(1);
imagesc(ZImage(:,:,Nspecs));    % Display CEST image at the reference offset
colormap(gray);                 % for use in defining the ROI
colorbar;

if nargin==4;
    BW=roipoly;          % If an ROI has not yet been defined, then use
    [x,y]=find(BW);      % the roipoly function to define one
end

ppms=ppmList(1:Nspecs/2);   % Allocate space for some space
MTRasym=zeros(Nspecs/2,1);  % for important vectors before
ppmList=ppmList(1:Nspecs-1);% the main loop

Bo=zeros(m,n);       % Allocate space for some important
AUC=zeros(m,n);      % Matrices befor ethe main loop

ZSpecAvg=zeros(Nspecs-1,1);     % Allocate space for the average
MTRasymAvg=zeros(Nspecs/2,1);   % quantities

% Here's the main loop to step through all the pixels in the image
% defined by the ROI specified in x and y
for j=1:length(x);
    ZSpec=zeros(Nspecs,1);
    for k=1:Nspecs;
        ZSpec(k)=ZImage(x(j),y(j),k);
    end
    ZSpec=100*ZSpec/ZSpec(Nspecs);      % Normalize the Z-Spectrum to the
                                        % reference spectrum

    ZSpec=ZSpec(1:Nspecs-1); % Removes the value from reference spectrum

    % Calculate the 0 ppm shift by fitting to a Lorentzian, which is
    % described by its height, width, offset from 0, and asymptotic value

    % Defines the region over which to use the data to fit
    FitRegion=[find(ppmList<=0.3 & ppmList>=-3)'];

    % Calculate the initial parameters to use for the fit
    dc0=100;
```

```
    Zero=find(ppmList==0);
    Height0=dc0-ZSpec(Zero);
    lw=find(ZSpec<Height0/2);
    if isempty(lw)==0;
        lw=lw(1);
        Width0=2*abs(ppmList(lw));
        if Width0==0;                                   % These safeguard
            Width0=(max(ppmList)-min(ppmList))/4;       % against unrealistic
        end                                             % values for the
    else                                                % line width
        Width0=(max(ppmList)-min(ppmList))/4;
    end

    % Define the data needed for the lsqcurvefit function
    xdata=ppmList(FitRegion);
    ydata=ZSpec(FitRegion);

                            % Calls the script to generate the string
    l=CESTShiftLorentzian;  % describing the upside-down Lorentzian which
                            % is used for the fit.

    fiteqn=inline(l,'x','xdata');
    p0=[Height0 Width0 dc0 0]; % The initial parameters.
    opts=optimset('MaxIter',100,'MaxFunEvals',2000,'Display','none'); %
Parameters used by
                                                                    % the
fitting routine

    % Performs the curve fit

[param,ressum,residual,exitflag,output]=lsqcurvefit(fiteqn,p0,xdata,ydata,[],
[],opts);

    % Extract the values of the parameters from the curve fit
    Height=param(1);
    Width=param(2);
    dc=param(3);
    xo=param(4); % This is the 0 ppm shift.

    if abs(xo)>1;
        xo=0;
    end

    Bo(x(j),y(j))=xo;

    % Now correct the Z-spectrum.  This is done by first shifting the
original
    % ppm voffset values and then using these values to interpolate the
    % Z-Spectrum to find the new corrected values.

    ppmListCorr=ppmList-xo;

    ZSpecCorr=zeros(length(ZSpec),1);
    for k=1:length(ppmList);
        a=find(ppmListCorr>ppmList(k));
```

```
        b=find(ppmListCorr<ppmList(k));

        if (isempty(b)==0 & isempty(a)==0);
            a=a(length(a));
            b=b(1);
            deltax=ppmList(k)-ppmListCorr(b);
            ZSpecCorr(k)=ZSpec(b)+((ZSpec(a)-
ZSpec(b))*deltax/(ppmListCorr(a)-ppmListCorr(b)));
        else
            ZSpecCorr(k)=ZSpec(k);
        end
    end

    % Calculate the MTrasym
    for k=1:Nspecs/2-1 % k=1:15
                                                                % The
MTRasym calculation
                                                                %
k=1:ZSpec(31)-ZSpec(1)
            MTRasym(k)=ZSpecCorr(length(ZSpecCorr)-k+1)-ZSpecCorr(k); %
k=2:ZSpec(30)-ZSpec(2)
                                                                %
|
                                                                %
k=15:ZSpec(17)-ZSpec(15)
    end                                                         % Note
still 0 at end.

    % Insert a value at 2.5 ppm if necessary.  This is based on the
    % observation that [2.5 0.5] is likele to be the best region to
    % integrate the MTRasym over, but initial studies did not incluse
    % 2.5 ppm as an offset.  Future studies will all include 2.5 ppm so
    % this will become unnecessary.
    if isempty(find(ppmList==2.5))==1
        a=find(ppms>2.5);
        a=a(length(a));
        ppms(a);
        NewValue=MTRasym(a)+(ppms(a)-2.5)*((MTRasym(a+1)-
MTRasym(a))/(ppms(a)-ppms(a+1)));
        ppmsNew=[ppms(1:a)' 2.5 ppms(a+1:length(ppms))'];
        MTRasymNew=[MTRasym(1:a)' NewValue MTRasym(a+1:length(MTRasym))'];
    else
        ppmsNew=ppms;
        MTRasymNew=MTRasym;
    end

    % Now calculate the more 'local' MTRasym value

                                % ppmTarget is either the value of the
expected
    if prod(size(ppmTarget))>1; % max CEST effect or a range [min max] around
                                % that expected value.

        adiff=find(ppmsNew-ppmTarget(1)==min(abs(ppmsNew-ppmTarget(1))));
        bdiff=find(ppmsNew-ppmTarget(2)==min(abs(ppmsNew-ppmTarget(2))));
        CESTdiffCorr=-trapz(ppmsNew(adiff:bdiff),MTRasymNew(adiff:bdiff));
```

```
    else
        adiff=find(ppmsNew-ppmTarget==min(abs(ppmsNew-ppmTarget)));
        CESTdiffCorr=MTRasymNew(adiff);
    end

    AUC(x(j),y(j))=CESTdiffCorr;

    ZSpecAvg=ZSpecAvg+ZSpecCorr;    % Keeps a running total of the ZSpec
    MTRasymAvg=MTRasymAvg+MTRasym;  % and MTRasym to calculate the average

end

ZSpecAvg=ZSpecAvg/length(x);        % Calculates the average ZSpec and
MTRasymAvg=MTRasymAvg/length(x);    % MTRasym for the ROI

% Plot the MTRasym AUC map
figure(2);
imagesc(AUC,[-5 15]);
colormap(gray);
colorbar;

% Plot the Bo map
figure(3);
imagesc(Bo,[-0.5 0.5]);
colormap(gray);
colorbar;

% If a plot of the average Z-Spectrum and MTRasym is desired, this could
% useful if a small ROI is used
if PlotFlag==1;
    figure(4);
    plot(ppmList,ZSpecAvg,'k');
    hold on;
    plot(ppmList(1:length(MTRasymAvg)),MTRasymAvg,'k');
    set(gca,'XDir','Reverse')
end
```